UNIVERSITÁ DEGLI STUDI DI MILANO - BICOCCA
Dipartimento di fisica G. Occhialini

CORSO DI DOTTORATO IN FISICA E ASTRONOMIA
CICLO XXIX

High-rate thermal neutron gaseous detector for use at neutron spallation sources

Tesi di Dottorato di:
GIORGIA ALBANI

Supervisor: Prof. Giuseppe Gorini
Coordinatore: Prof.ssa Marta Calvi

Anno Accademico 2016-2017

To Andrea,
Mum, Dad, Samuel,
Antonietta and Umberto
with love.

Abstract

Neutron science is faced with the challenge of finding alternative technologies to ^{3}He as a thermal neutron detector with a rate capability matching the high flux as expected at the European Spallation Source (ESS).

Aim of this PhD thesis is the development of a ^{3}He-free high-rate thermal neutron gaseous detector based on the Gas Electron Multiplier (GEM) technology for applications at spallation sources. A key role in thermal neutron detectors is played by the "converter" material, which allows for the conversion of neutrons into secondary charged particles via nuclear reactions such as $^{10}\mathrm{B}(n,\alpha)^7\mathrm{Li}$.

During the project four detector prototypes were developed, assembled and tested at spallation sources (such as the ISIS facility, Didcot, UK) and nuclear reactors (such as the ORPHEE reactor, Saclay, France and the JEEP II reactor, Kjeller, Norway) and this thesis is focused on optimisation calculations prior the detector assembly, experimental tests and data analysis. The detectors had different converter geometries ranging from a GEM detector coupled to a planar B_4C converter to the BAND (Boron Array Neutron Detector)-GEM technology provided with a 3D converter structure. Along with the evolution of the converter technology goes the improvement of detector performance: the latest BAND-GEM prototype has an efficiency of $\approx 40\%$ at $\lambda = 4\,\text{Å}$ and spatial resolution of ≈ 6 mm.

These and other features obtained with this new technology, make it an attractive candidate for installation - after further optimisation - on LoKI, a Small Angle Neu-

tron Scattering (SANS) instrument and one of the first ones under construction at the ESS. The optimisation will make use of the Geant4-based simulation framework already developed in this thesis to study the detector spatial and time resolution, detection efficiency and other detector features such as multiple hits on readout pads. More generally the results presented in this thesis demonstrate that the BAND-GEM technology can contribute to the replacement of ^{3}He-based detectors in applications where high count rates are expected over areas of the order $\approx 1\,\mathrm{m}^2$ and the spatial resolution along the neutron flight path (that reflects into the *Time-of-Fligth* resolution) is not too demanding.

Contents

Abstract **v**

List of attached papers **xiii**

1 Introduction **1**

1.1 Outline of the thesis 2

1.2 Neutron scattering science 3

1.3 European Spallation Source 6

1.4 The ^{3}He crisis 7

1.4.1 The ^{3}He shortage 7

1.4.2 Alternatives to ^{3}He in neutron detection 8

2 Gaseous Neutron detectors **11**

2.1 Thermal neutron interaction with matter 11

2.1.1 Nuclear reactions for thermal neutron detection 12

2.2 Thermal neutron gaseous detectors 14

2.2.1 Modes of gas detector operation 15

2.2.2 Pulse Height Spectrum (PHS) and counting plateaus 19

3 bGEM neutron detector **23**

3.1 GEM detectors 23

3.2 bGEM description 28

3.2.1 Boron-based planar converter 29

3.2.2 Electronics read-out 32
3.3 Diffraction measurements 33
3.3.1 The INES instrument at ISIS 33
3.3.2 Experimental set-up 34
3.3.3 Results and Performances 36
3.4 High-rate measurements 41
3.4.1 ORPHEE reactor and G3-2 irradiation station 41
3.4.2 Experimental set-up 41
3.4.3 Results 42
3.5 Conclusions 43
4 BAND-GEM neutron detector: first prototype 45
4.1 From planar to 3D converters 45
4.2 The BAND-GEM detector design 46
4.3 Neutron radiography analysis 48
4.3.1 Destructive measurements 49
4.3.2 Theoretical calculations 50
4.3.3 Experimental set-up and image analysis 52
4.4 Counting rate measurements versus tilt angle 54
4.4.1 Experimental set-up 55
4.4.2 Performance results 57
4.5 Diffraction measurements 58
4.5.1 Experimental set-up 59
4.5.2 Results and Performances 60
4.5.3 Conclusions 63

5 BAND-GEM: second prototype **65**

5.1 Limits of the first prototype 65

5.2 Second prototype design 66

5.3 Detector test 68

5.3.1 EMMA instrument 69

5.3.2 Experimental set-up 69

5.3.3 Performance results 70

5.4 Conclusions 79

6 BAND-GEM for SANS applications **81**

6.1 LoKI instrument 82

6.1.1 Small Angle Neutron Scattering technique 82

6.1.2 Instrument overview and detectors 85

6.2 Simulation of detector performance 86

6.2.1 The dgcode simulation framework 87

6.2.2 Advantages and limits of the MC simulations 87

6.2.3 Detector design in Geant4 89

6.2.4 Timing resolution 91

6.2.5 Energy deposition volume 93

6.2.6 Multiple hits 96

6.2.7 Efficiency 100

6.3 Conclusions 101

7 Conclusions **103**

List of Tables **109**

List of Figures **110**

Bibliography **113**

Synopsis of attached papers **119**

List of attached papers

This thesis is based on the following papers, which are referred to in the text:

I G. Albani, G. Croci, C. Cazzaniga, M. Cavenago, G. Claps, A. Muraro, F. Murtas, R. Pasqualotto, E. Perelli Cippo, M. Rebai, M. Tardocchi and G. Gorini, Neutron beam imaging with GEM detectors. *Journal of Instrumentation*, 10(04):C04040, 2015.

II G. Croci, G. Albani, C. Cazzaniga, E. Perelli Cippo, E. Schooneveld, G. Claps, A. Cremona, G. Grosso, A. Muraro, F. Murtas, M. Rebai, A. Scherillo, M. Tardocchi and G. Gorini, Diffraction measurements with a boron-based GEM neutron detector. *Europhysics Letters*, 107(1):12001, 2014.

III E. Perelli Cippo, G. Croci, A. Muraro, A. Menelle, G. Albani, M. Cavenago, C. Cazzaniga, G. Claps, G. Grosso, F. Murtas, M. Rebai, M. Tardocchi and G. Gorini, A GEM-based thermal neutron detector for high counting rate applications. *Journal of Instrumentation*, 10(10):P10003, 2015.

IV A. Muraro, G. Albani, E. Perelli Cippo, G. Croci, G. Angella, J. Birch, C. Cazzaniga, R. Caniello, F. Dell'Era, F. Ghezzi, G. Grosso, R. Hall-Wilton, C. Höglund, L. Hultman, S. Schimdt, L. Robinson, M. Rebai, G. Salvato, D. Tresoldi, C. Vasi and M. Tardocchi, Neutron radiography as a non-destructive method for diagnosing neutron converters for advanced thermal neutron detectors. *Journal of Instrumentation*, 11(03):C03033, 2016.

V G. Albani, E. Perelli Cippo, G. Croci, A. Muraro, E. Schooneveld, A. Scherillo, R. Hall-Wilton, K. Kanaki, C. Höglund, L. Hultman, J. Birch, G. Claps, F. Murtas, M. Rebai, M. Tardocchi and G. Gorini, Evolution in boron-based GEM detectors for diffraction measurements: from planar to 3D converters. *Measurements science and technology*, 27(11):115902, 2016.

1

Introduction

Neutron scattering science allows to investigate atomic-scale structure and dynamics of materials providing information highly complementary to that from photon or electron scattering techniques. The core activity of present spallation neutron sources is represented by neutron spectroscopy and diffraction experiments using neutron beams of thermal energies, *i.e.* $E_{th} = 25\,\mathrm{meV}$, corresponding to a wavelength of $\lambda = 1.8\,\text{Å}$. Nowadays most neutron beam lines use ^{3}He detectors that have an excellent intrinsic efficiency ($> 80\%$ for thermal neutrons) and can cover large areas (several m^2). However in recent years the production of ^{3}He from tritium decay has declined with the reduction of the nuclear weapons stockpile [1] [2]. This has led to a substantial increase of the ^{3}He price preventing its extensive use for research applications including future neutron sources such as the *European Spallation Source* (ESS) [3][4]. Besides the need for replacing ^{3}He [5], it is essential to develop high-rate neutron detectors that can fully exploit the increase of neutron flux of ESS compared to present-day sources [6] [7] [8] [9]. Thus, it is necessary to develop a large area and high-rate neutron detector that does not use ^{3}He but has a comparable detection efficiency, an affordable price and a space resolution of $100\,\mu\mathrm{m} - 100\,\mathrm{mm}$ depending

on the applications.

Gas Electron Multiplier (GEM) [10] detectors are good candidates for this aim. These detectors are generally used in high-energy physics for tracking and triggering signals [11] [12] [13] thanks to their good spatial resolution (from $80\,\mu m$ up to a few mm) and timing properties. Moreover they have an excellent rate capability (MHz/mm^2) and can cover large areas ($\approx 1\,m^2$) at low cost [14]. Although GEM-based detectors are mainly used with charged particles, they can be adapted to detect neutrons [15] [16] [17]. This is achieved by adding a geometrically optimised "converter", as for instance boron carbide (B_4C) layers, in order to detect thermal neutrons through the $^{10}B(n,\alpha)^7Li$ reaction. An early example of these detectors is CASCADE [18] made of borated GEM foils. This detector has limited global rate capability due to the signal read-out based on strips, therefore it is of limited interest for use at ESS.

This thesis presents the development of a new detector with high rate capability and good spatial resolution based on the GEM technology. In this project four detector prototypes with different converter geometries were developed, assembled and tested. With the evolution of the converter technology comes the improvement of detector performance such as efficiency and spatial resolution. This technology represents an interesting alternative to ^{3}He-based detectors with promising applications at ESS.

1.1 Outline of the thesis

This thesis is devoted to the development of a ^{3}He-free high-rate thermal neutron gaseous detector based on the Gas Electron Multiplier (GEM) technology for applications at spallation sources.

The first part of the presented work provides a brief description of the state of the art of neutron scattering science, including the features of the new ESS facility, and

the historical and economical context that motivates the development of detectors alternative to ^{3}He-based ones.

Chapter 2 reports a theoretical introduction about thermal neutron interaction with matter and ^{3}He properties relevant for gaseous detectors are also discussed.

Two planar converter GEM detector prototypes assembled during this thesis are described in Chapter 3 along with the results of characterisation and diffraction experiments carried out at the ISIS spallation source. The excellent results reached in terms of counting rate at the ORPHEE facility are presented, showing improvements of several orders of magnitude relative to the ^{3}He detectors, well in excess of count rate requirements for use at ESS. The main limitation of the GEM technology is the detection efficiency, which depends on the geometry and composition of the neutron converter.

The evolution of the GEM-based detector from a planar to a 3D converter lead to the BAND-GEM detector technology. Two different BAND-GEM prototypes were assembled and tested during the project as described in Chapter 4 (BAND-GEM with lamellas) and 5 (BAND-GEM with grids). In particular, the latter provided encouraging results in terms of efficiency ($\epsilon \approx 40\%$ at $\lambda = 4\,\text{Å}$).

Chapter 6 reports a study performed within a Geant4-based simulation framework aiming at the optimisation of the BAND-GEM technology for the LoKI instrument at ESS.

The main findings of this thesis project are summarised in Chapter 7.

1.2 Neutron scattering science

Neutron scattering science investigates the atomic-scale structure and dynamics of materials using neutrons [19]. In particular, thermal neutrons have wavelengths similar to the spacing between atoms ($\approx 1 \quad \mathring{A}$) so they are well suited to study the structure of matter with atomic resolution; they have energies similar to those of

atom vibrations in materials ($\approx$ 1 meV) to study their dynamics. The neutral electric charge allows these particles to penetrate deeply into materials and perform non-destructive measurements in bulk. Neutron scattering provides information that is highly complementary to that from photon or electron scattering techniques. Indeed, whereas the X-ray atomic scattering factor increases linearly with atomic number the neutron cross section can vary greatly between elements of similar atomic number and even between isotopes of the same element. As a consequence hydrogen nuclei, for instance, are almost invisible to X-rays while they scatter neutrons strongly and their presence and motion can be easily found in a neutron scattering experiment making this technique very useful to study organic sample. All these properties make the neutron scattering technique applicable to many fields of study including Chemistry, Biophysics, Condensed Matter science, Engineering and Cultural Heritage.

Many different techniques that profit from the neutron scattering properties in material are exploited. For instance neutron diffraction (ND) [20] provides information on the structure of a material, *i.e.* location of atoms within a sample, which may be a single crystal, a polycrystalline powder. *Small Angle Neutron Scattering* (SANS) [21] is generally used to study the bulk properties of a material (such as size, structure and particle interaction) otherwise neutron reflection (NR) is used to characterise thin film systems in the direction perpendicular to the surface to give information such as layer thickness and orientation. The length scales probed by SANS and NR techniques range from tens to hundreds of nanometers which make them ideal for studying material such as surfactants, colloids and polymers.

The measurement principle of ND is based on Bragg diffraction (Fig. 1.1). When electromagnetic radiation or subatomic particle beams are incident on a crystalline lattice with wavelength comparable to atomic spacings ($\sim$ Å), constructive interference is observed due to waves reflection by parallel crystalline planes in accordance

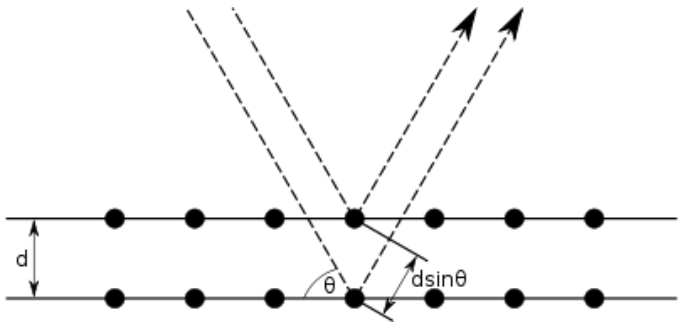

FIGURE 1.1: Representation of Bragg diffraction on a crystalline lattice. It can be noticed that the difference in the the path between two waves undergoing interference is given by $2d\sin\theta$.

to Bragg's law:

$$2d\sin\theta = n\lambda \tag{1.1}$$

where d is the distance between two parallel planes, θ is the beam incidence angle, n is an integer determined by the diffraction order, and λ is the beam wavelength. In a typical diffraction experiment the number of scattered neutrons in function of 2θ and λ is measured where λ depends on neutron energy and 2θ depends on detector position. Since a nuclear reactor is a continuos source of neutron with different energies [22], a diffraction experiment can be performed settling a specific λ with a monochromator and measuring different 2θ with a movable detector. Conversely in a pulsed source such as a spallation source the diffraction experiment can be performed using the *Time-of-Flight* (ToF) technique [22] in which a fixed detector system defines 2θ and a white (*i.e.* not monochromatic) neutron beam is used.

The extreme limits of extensions of the Bragg law is SANS [21] that is generally used by biophysics and soft-matter users to study materials such as colloids, polymers or solution structures of proteins on the micrometer to nanometer scale length. A description of this technique is reported in Sec. 6.1.1.

Inelastic neutron scattering [23] is widely used to study molecular oscillations like vibrations and rotovibrations. In fact neutrons may be inelastically scattered

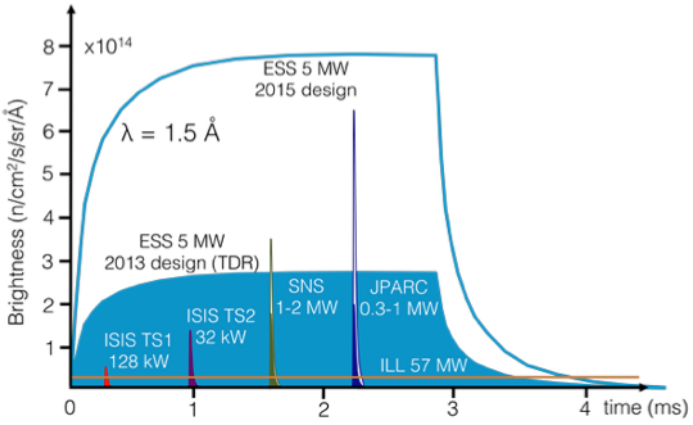

FIGURE 1.2: ESS pulses compared to the pulses of present-day spallation sources or reactors.

by exciting (or absorbing) a vibrational state in a molecule, much like in infrared spectroscopy with the advantage of absence of selection rules.

1.3 European Spallation Source

The European Spallation Source in Lund, Sweden, will offer neutron beams of unparalleled brightness (about 7×10^{14} n/s/cm^2/sr/Å) for cold neutrons and with higher peak intensity than any other spallation source [3][4] (Fig. 1.2). The neutron pulse will be ≈ 2.86 ms long with a repetition rate of 14 Hz [4]. Investigations of structures and dynamics over several length- and time-scales will be possible. By the end of its construction in 2025, a suite of sixteen neutron scattering instruments will be available to the user community. A new generation of detection system will be developed for the ESS instruments [7].

1.4 The ^{3}He crisis

1.4.1 The ^{3}He shortage

^{3}He is a rare (natural abundance: 1.37 parts per million) isotope of helium; it is nontoxic and absorbs neutrons with a large cross section. For these reasons it plays a key role in neutron detection for applications in homeland security, industry and science. By far the most common source of ^{3}He in the United States is the U.S. nuclear weapons program [1], of which it is a byproduct. In fact ^{3}He is produced by tritium decay:

$$^3\mathrm{H}\,(\mathrm{t}_{1/2} = 12.3\,\mathrm{y}) \rightarrow {}^3\mathrm{He} + \mathrm{e}^- + \bar{\nu_\mathrm{e}}. \tag{1.2}$$

For many years the ^{3}He demand was small enough that a significant stockpile accumulated. After the terrorist attacks of September 11, 2001, the federal government began using neutron detectors at the U.S. border to avoid the introduction of smuggled nuclear and radiological material, enhancing the ^{3}He demand. Moreover the use of this isotope increased in medical imaging techniques. As a consequence, the size of the stockpile was significantly reduced causing the current worldwide ^{3}He-shortage [1] [2]. Potential sources of ^{3}He beyond the nuclear weapons program, include tritium produced as a byproduct in commercial heavy-water nuclear reactors, extraction of ^{3}He from natural gas or the atmosphere and production using particle accelerators [1]. These alternative sources were not considered economic until the ^{3}He supply was available, so at present ^{3}He is only produced as a byproduct of the manufacture and purification of tritium for use in nuclear weapons. This means that the tritium needs of the nuclear weapons program, not the demand for ^{3}He itself, determine the amount of ^{3}He produced. Policymakers have to decide about how or whether to increase ^{3}He supply or reduce ^{3}He demand and about possible alternative mechanisms for allocating supply. It is likely that a combination of policy approaches will be fundamental. In Fig. 1.3 the ^{3}He production, demand and supply from 1999 to 2010

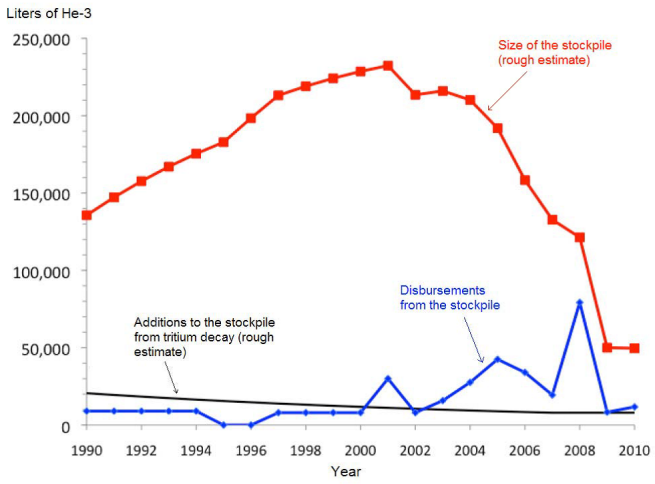

FIGURE 1.3: The ^{3}He stockpile grew from roughly 140000 litres in 1990 to roughly 235000 litres in 2001. Nevertheless, since 2000 ^{3}He demand has exceeded production. By 2010, the increased demand had reduced the stockpile to roughly 50000 litres.

are shown in black, blue and red respectively.

1.4.2 Alternatives to ^{3}He in neutron detection

Detectors based on lithium or boron for thermal neutron detection represent nowadays the most promising candidates to solve the ^{3}He problem. A first technique is based on ZnS/LiF scintillator [24] coupled to a 2D system of wavelength shifting fibres used to cover large areas and to measure the interaction point. This technique offers a high spatial resolution but is rather expensive. Another example of neutron detector is the proportional counter with a gas mixture containing BF_3 [24]. This has the same geometry of ^{3}He counter but has a lower detection efficiency due to BF_3 pressure limitations. In addition BF_3 is highly toxic thus implying serious safety issues. Another class of detectors alternative to ^{3}He is represented by detectors based on solid state boron layers. For instance the Multi-Blade detector [25] [26] uses solid ^{10}B films in a proportional gas chamber. Although this detector has high spatial resolution and good performances in high rate environments, it is rather compact

in size and so suitable for reflectometry but it cannot be used in applications where large-area detectors are required, such as SANS. Another example of boron-based detectors is the CASCADE detector [18]. It is made of borated GEM foils and coupled to a read-out anode based on strips that limits the rate capability with respect to the ESS requirements.

2

Gaseous Neutron detectors

2.1 Thermal neutron interaction with matter

Neutrons carry no electric charge, thus the interaction with matter is mainly with nuclei by means of the strong force [27]. After the interaction neutrons can change their direction and energy or be captured and replaced by byproducts (generally heavy charged particles). These two processes are named scattering (that can be elastic or inelastic) and absorption, respectively [24]. The probabilities of the various type of neutron interactions change significantly with neutron energy so neutrons may be divided in two main categories: *fast* ($E_n > 0.5\,\mathrm{eV}$) and *slow* ($E_n < 0.5\,\mathrm{eV}$) where 0.5 eV is a conventional boundary corresponding to the *cadmium cutoff* energy. Therefore detector systems for neutrons are usually optimised for a specific energy range. We often refer to *thermal neutrons* that, at room temperature, have an average energy of about $E_{th} = 25\,\mathrm{meV}$ and they identify an energy range within the slow neutrons. This thesis project addresses the development of a detector for thermal neutrons.

Thermal neutrons have a high probability to interact by elastic scattering (*i.e.*

A(n,n)A) and neutron induced nuclear reactions. Since low energy neutrons transfer very little energy to the nuclei in the elastic scattering, it is impossible to detect thermal neutrons based on this reaction.

The thermal neutron interaction of real importance are neutron-induced reactions that can create secondary radiations of sufficient energy to be detected directly. Since the incoming neutron energy is very low, all such reactions must have a positive Q-value (*i.e.* the amount of energy released by the reaction and defined as $Q = K_f - K_i$) to be energetically possible. Thus nuclear reactions such as (n,α), (n,p), (n,fission) are good candidates for thermal neutron detection.

2.1.1 Nuclear reactions for thermal neutron detection

A typical neutron detector is composed of a target material designed to convert the primary neutron radiation in secondary charged radiations together with a conventional charged particle detector. The ideal nuclear reaction useful to detect thermal neutrons should have very high cross section (for an high detector efficiency). The target material should be of high natural isotopic abundance or alternatively an economical artificial source and the reaction should be suitable to discriminate gamma-rays (an ubiquitous background radiation in neutron measurements). The higher the Q-value, the greater is the energy transfer to byproducts and the easier is the γ-ray discrimination. Typical reactions used to convert thermal neutrons into directly detectable particles are:

- $^{10}\mathrm{B}(n,\alpha)^{7}\mathrm{Li}$ reaction.

$$^{10}\mathrm{B} + \mathrm{n} \rightarrow \begin{cases} ^{7}\mathrm{Li} + \alpha, & \mathrm{Q} = 2.792\,\mathrm{MeV}\ (\text{ground state, } 6\%) \\ ^{7}\mathrm{Li}^{*} + \alpha, & \mathrm{Q} = 2.310\,\mathrm{MeV}\ (\text{excited state, } 94\%) \end{cases} \tag{2.1}$$

  Since the neutron momentum is several orders of magnitude smaller than the momentum of the byproducts, it is possible to assume that they are directed

back-to-back. In the excited state (94% branching ratio) their energy values are:

$$E_{Li} = 0.84\,\mathrm{MeV} \qquad \text{and} \qquad \mathrm{E}_{\alpha} = 1.47\,\mathrm{MeV} \tag{2.2}$$

The cross section for thermal neutrons is 3840 barns. ^{10}B is readily available and its natural isotopic abundance is 19.8%.

- ^{6}Li(n, α)^{3}H reaction.

$$^{6}\mathrm{Li} + \mathrm{n} \rightarrow ^{3}\mathrm{H} + \alpha \qquad \mathrm{Q} = 4.78\,\mathrm{MeV} \tag{2.3}$$

Also here the reaction products are assumed to be emitted back to back and the energies are:

$$E_{^{3}H} = 2.73\,\mathrm{MeV} \qquad \text{and} \qquad \mathrm{E}_{\alpha} = 2.05\,\mathrm{MeV} \tag{2.4}$$

The thermal neutron cross section for this reaction is 940 barns, the natural isotopic abundance of ^{6}Li is 7.40%.

- ^{3}He(n, p)^{3}H reaction.

$$^{3}\mathrm{He} + \mathrm{n} \rightarrow ^{3}\mathrm{H} + \mathrm{p} \qquad \mathrm{Q} = 0.764\,\mathrm{MeV} \tag{2.5}$$

For reactions induced by slow neutrons the byproducts are assumed to be emitted back to back with energies:

$$E_{p} = 0.573\,\mathrm{MeV} \qquad \text{and} \qquad \mathrm{E}_{^{3}\mathrm{H}} = 0.191\,\mathrm{MeV} \tag{2.6}$$

The thermal neutron cross section for this reaction is 5330 barns, significantly higher than that of ^{10}B.

Although the cross section of the thermal neutron capture reaction in ^{10}B is lower than that of ^{3}He, the Q-value of the former is about 3 times the latter, in principle allowing a better discrimination with low energy γ events. However, since the ^{10}B

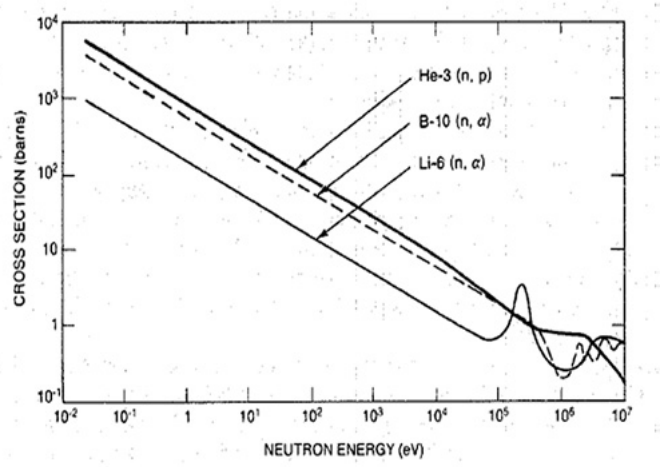

FIGURE 2.1: Cross section versus neutron energy for some reactions of interest in neutron detection

.

converter is generally used in solid layers, the energy loss in the solid causes a mix up with the lower part of the spectrum and even loss of the reaction byproducts (see Chapter 3).

In Fig. 2.1 the cross sections *vs* neutron energy for the discussed reactions are shown [28]: it can be seen that the cross sections scale as $1/v$, where v is the neutron velocity. In thermal neutron detectors the information on the neutron energy is completely lost in the conversion process of a neutron into charged particles, and so thermal neutron detector cannot give information about the initial neutron energy, they detect only the neutron passage in the material.

2.2 Thermal neutron gaseous detectors

Thermal neutron detection can be achieved either with gas detectors containing ^{3}He or ^{10}B or scintillators containing ^{10}B or ^{6}Li. Since this thesis aims to develop a thermal neutron gaseous detector alternative to ^{3}He the focus is on this kind of technology.

When a charged particle passes through a gas, ionisation and excitation of gas molecules occur along the particle track. Most gas filled detectors are based on the collection of all the charges created by ionisation within the gas through the application of an electric field. In the following section the operation mode of the most used gas detectors are shown.

2.2.1 Modes of gas detector operation

Gaseous detectors have three main regions of operation [24]:

- ionisation mode;
- proportional mode;
- Geiger-Muller mode;

and they are defined by the detector geometry, the field configuration and the amplification process. Fig. 2.2 shows the different operating regions as function of the applied voltage. Based on these features, gaseous detectors may be divided in three categories: ionisation chambers, proportional chambers and Geiger-Mueller detectors.

Ionization Mode

A gaseous detector working in ionisation mode is called ionisation chamber. After ionisation by the charged particles the most important electron interactions that normally occur are:

- charge transfer: an electron is transferred from a neutral molecule to an ion, reversing the two initial states;
- electron attachment: a free electron is kept by a neutral molecule, which becomes a negative ion;

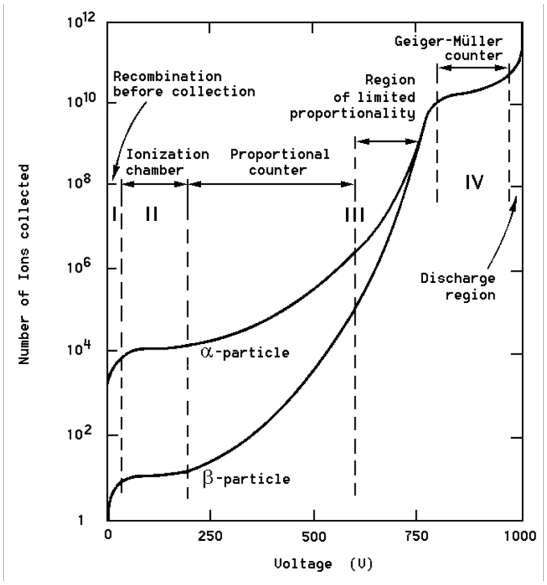

FIGURE 2.2: Number of ions (α or β particles) collected in a gas detectors as a function of the applied voltage.

- recombination: in which an electron is absorbed by a positive ion, giving rise to a neutral molecule.

Diffusion also takes place due to collision between electrons and atoms.

In ionisation chambers a potential difference is applied between anode and cathode. If a sufficiently high electric field is generated, electrons drift towards the anode and ions towards the cathode avoiding recombination. The signal is generated by the movement of the primary charges inside the gas volume towards the two electrodes. Highly ionising particles, such as α-particles or heavy ions, are more easily detectable with ionisation chambers since their energy loss is large and so the generated signal is high enough to overcome the noise usually present in the read-out electronics.

Proportional Multiplication Mode

Gas multiplication occurs when the applied electric field is sufficiently high so that free electrons are accelerated to an energy that can be greater than the ionisation

energy of the neutral gas molecules. In this case an additional electron-ion pair may be created in the collision. Since the average electron energy increases with an increasing electric field, there is a threshold value for the field above which this secondary ionisation occurs. In typical gases at atmospheric pressure, the threshold field is $\sim 10^6\,\mathrm{V/m}$. These secondary electrons are then accelerated by the electric field and can ionise the gas further. This kind of cascade gas multiplication process is known as the *Townsend Avalanche*. The increase in the number of the electrons per unit path length is described by the corresponding Townsend Equation [24]:

$$dn = n\alpha dx \tag{2.7}$$

where n is the number of electrons, dn is the new created number and α is the *First Townsend Coefficient* for the gas, *i.e.* the inverse of the mean free path for ionisation. Its value is zero for below-threshold field and increases with the electric field. α is constant for a uniform field and the solution of the Townsend Equation predicts the electron density grows exponentially with distance during the avalanche:

$$n(x) = n(0)e^{\alpha x} \tag{2.8}$$

In the cylindrical geometry the electric field increases in the same direction as the avalanche. When all free electrons are collected at the anode the avalanche ends. Under suitable conditions the number of secondary ionisation events may be kept proportional to the number of primary ion pairs formed.

The proportional chambers takes advantage of the charge multiplication in order to detect X-Rays or of the so-called Minimum Ionising Particles (MIPs) that produce a small amount of ion pairs. The initial energy of the ionising particle can be measured because the amount of charges produced in the avalanche is still proportional to the number of pairs created by the radiation and, therefore, to the energy loss in the gas.

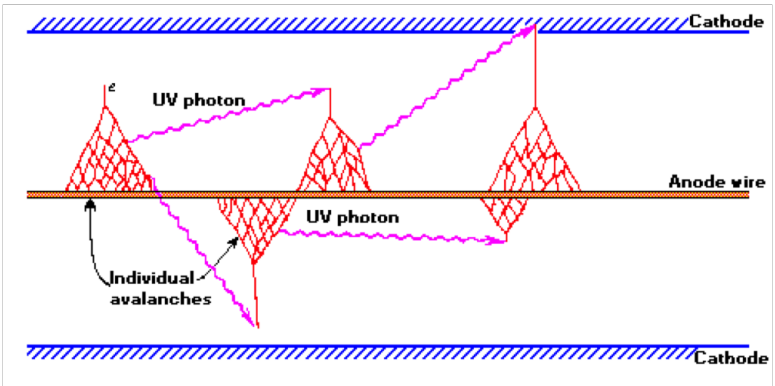

FIGURE 2.3: Cross section of a Geiger counter and description of the mechanism by which additional avalanches are triggered in a Geiger discharge.

Geiger-Mueller Multiplication Mode

If the value of the electric field is sufficiently high, the charge created by the positive ions may become completely dominant in determining the subsequent history of the pulse. Under this condition, an avalanche is able to trigger a second avalanche in a different position in the chamber through the emission of a UV photon. This *Geiger Discharge* continues until a sufficient number of ion pairs have been created in order to reduce the electric field below the threshold at which additional gas multiplication can take place. The process is then self-limiting and terminates when the same number of positive ions are formed regardless of the number of initial ion-pairs created by the incident radiation. Each output pulse from a detector operating in this mode is of the same amplitude and no longer reflects any property of the incident radiation. In Fig. 2.3 the operation of a Geiger-Mueller counter is shown [24]. The detector consists of a central anode wire inserted into a cylindrical metallic envelope that encloses the gas volume. Noble gases are usually employed in a Geiger Counter.

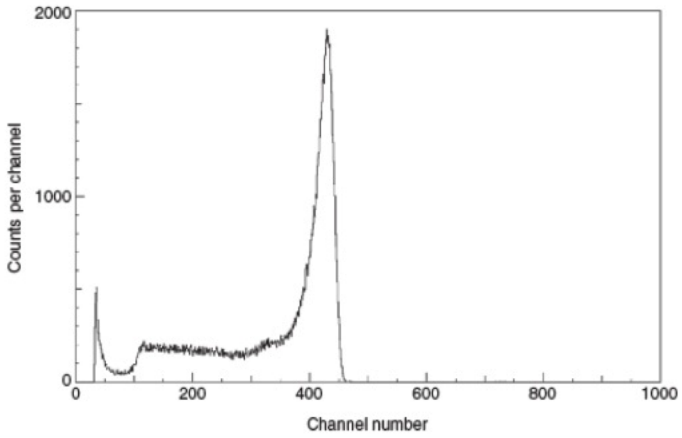

FIGURE 2.4: Differential pulse-height spectrum for thermal neutrons detected by a ^{3}He-filled gas counter.

2.2.2 Pulse Height Spectrum (PHS) and counting plateaus

In thermal neutron detectors the information on the neutron energy is completely lost in the conversion process of a neutron into charged particles. On the other hand the energy of capture byproducts can be measured. When a detector is operated in pulse mode, each individual pulse amplitude provides information on the energy deposited in the gas volume. Pulse amplitude information may be deduced by the *differential pulse height distribution* (PHS or Pulse Height Spectrum) [24]. Fig. 2.4 is a typical PHS from a ^{3}He proportional counter. The abscissa is a linear pulse amplitude scale that runs from zero to a value larger than the amplitude of any pulse observed and its unit is V. The ordinate is the differential number dN of pulses observed with an amplitude within the differential amplitude increment dH, divided by that increment, or dN/dH and it has units of inverse amplitude (V^{-1}). The shape of the PHS in Fig. 2.4 is due to the kinematics of the conversion process and the choice of amplifier time constants. The full energy peak represents the 764 keV released in the reaction. In the ideal case of a very large tube, the byproducts release all their energy inside the gas volume, thus generating pulses of the same amplitude. However

if a neutron is converted very close to the detector wall one of the two fragments may hit the wall without releasing its energy into the gas and the related output pulse will have a smaller amplitude. The cumulative effect of this kind of process is the *wall effect* and the result on the PHS is shown in Fig. 2.4 where a tail in the energy distribution toward smaller energies from the full energy peak is visible. Since the byproducts are emitted back-to-back, at least one of them is detected. Thus, there is a minimum collection energy, with a wide valley below, and then a low energy increase due to the noise and piled-up γ-ray events.

The degree of charge collection from the tube is determined by the choice of the amplifier time constant. Time constants of $2\,\mu$s or greater result in nearly complete charge collection leading to the spectrum in Fig. 2.4 with a 10% resolution (FWHM) of the full energy peak. A $0.5\,\mu$s time constant is a commonly used compromise between good resolution and high-rate capability [28].

In performing a pulse counting measurement, it is important to establish an operating point that will provide maximum stability over long period of time. Such a point lies in correspondence of the valley in the differential pulse height spectrum, indeed small changes in the discrimination level (*i.e.* the level H_d that a signal pulse must exceed in order to be registered) will have a minimum impact on the total number of pulses recorded. In general these operation areas are called *counting plateaus* and they can also be found varying the gain (or directly the applied voltage to the detector) [24]. A typical counting plateau curve is shown in Fig. 2.5 [28].

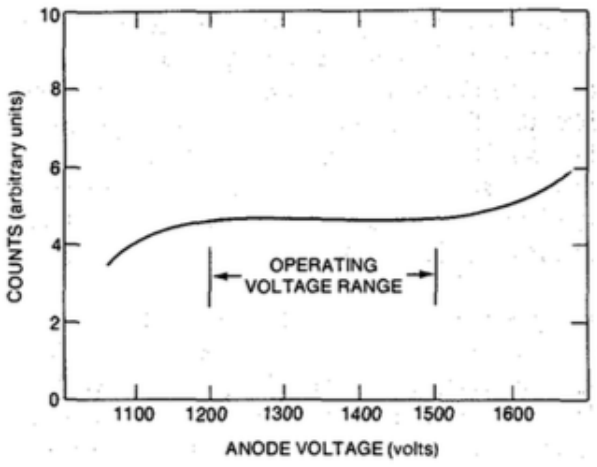

FIGURE 2.5: Typical counting plateau curve for a gas-filled ^{3}He counter.

3

bGEM neutron detector

The bGEM [16] is the first thermal neutron detector tested during this PhD project.

The bGEM detector is based on the *Gas Electron Multiplier* (GEM) technology, which is a charge amplification technique invented by Fabio Sauli in 1997 [10] and used in position sensitive detectors for ionising radiation.

The bGEM foils were produced at CERN [29] and the assembly was made at the *"Instituto di Fisica del Plasma Piero Caldirola"* (IFP) at CNR in Milan, Italy.

In this Chapter the GEM technology and the bGEM detector are described in Sec. 3.1 and in Sec. 3.2. In Sec. 3.3 the results of the first application of the bGEM in diffraction measurements are presented. Further results concerning the detector counting rate capability are shown in Sec. 3.4.

3.1 GEM detectors

Since the GEM detectors are based on gas ionisation by charged particles, they are not directly sensitive to neutrons, thus they need to be coupled to a suitable converter. A GEM consist of a very thin ($\approx 50\,\mu$m) insulating foil, generally a polyimide (kapton) [30], coated on both sides by a conductive material, usually

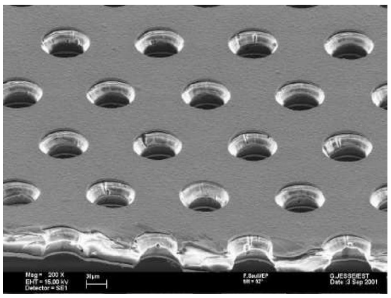

FIGURE 3.1: Microscopic view of a Gas Electron Multiplier foil.

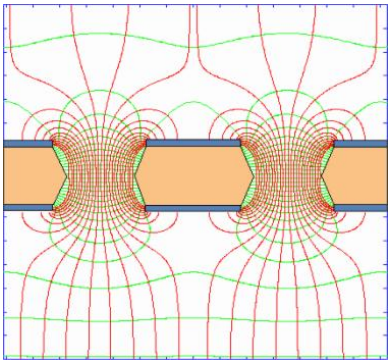

FIGURE 3.2: Drift field lines (red) and equipotential lines (green) in the holes of a GEM foil.

copper, perforated by a high density regular matrix of micro holes with a diameter $d \approx 70\,\mu$m and a pitch of $\approx 140\,\mu$m created with the pholitographic method [31]. A picture of a GEM foil is shown in Fig. 3.1. If a potential difference is applied at the boundary of the foils, an intense dipole electric field ($\approx 60\,$kV/cm) is created inside the holes (Fig. 3.2). This field allows for the ionisation electrons to drift in the holes, multiply and transfer to a collection region. Three regions are defined in a single GEM detector as shown in Fig. 3.3. The *drift gap* is the region between the cathode and the GEM foil where the primary ionisation charge is created. This region represents the sensitive volume of the detector and the length of the gap must be chosen taking into account the range of the ionising particles. The *multiplication region* is composed by the holes in the GEM foils. The electronic charge is amplified

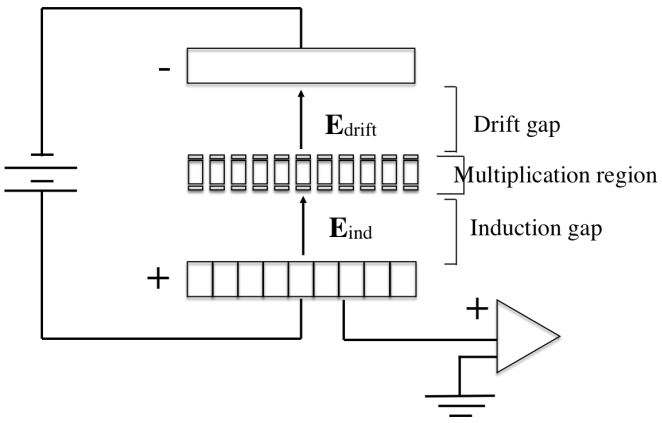

FIGURE 3.3: Sketch of a single GEM detector.

by a factor that depends on the field intensity and the thickness of the foil. By using a cascade of several GEM foils (typically three) lower voltages are needed on each GEM foil to achieve high gains, thus reducing the discharge probability. Finally, the *induction gap* is the region between the GEM foil and the anode where the multiplied charge induces a signal that can be amplified and collected. The signal of a GEM detector is completely generated by electrons. Indeed the electrons move along the field lines from the drift region across the GEM foil towards the induction gap, where an induced current can be measured as soon as the electrons move. On the contrary the positive ions are directed from the drift region to the cathode and the signal induced by the movement of the positive charges is completely shielded by the GEM foil. Thus the accumulation of positive ions from gas ionisation does not modify the induction field and consequently the gain. This property allows for the GEM to reach rate capabilities much higher than standard ^{3}He tubes where the space charge of positive ions makes the shaping time of signals longer. The gain is changed by acting on the drift field E_{drift} and on the induction field E_{ind}. Two different gains

can be defined in the detector:

$$G_{real} = \frac{\text{n. of multiplied } e^-}{\text{n. of primary } e^-} \tag{3.1a}$$

$$G_{eff} = \frac{\text{n. of detected } e^-}{\text{n. of primary } e^-} \tag{3.1b}$$

Since a fraction of the multiplying electrons, dependent on the field, is lost on the bottom of the GEM foil, the effective gain is always lower than the real gain [11]. The charge collection in the drift gap towards the multiplication region depends on a correct tuning of E_{drift}. In fact low values of E_{drift} can cause a gain loss due to recombination of electrons; on the other hand, if the field is too high the electrons knock into the top of the GEM foil. Typical values for this kind of detector are $E_{drift} \approx 1.8\,\text{kV/cm}$. The effective gain depends on the induction field. The number of electrons that reach the anode is enhanced if the induction field increases, but also the discharge probability increases. The effective gain raises exponentially with the potential applied to the GEM foils. The induction field is about $E_{ind} \approx 2.5\,\text{kV/cm}$.

The detector is filled with a continuous gas flow of a Ar/CO_2 (70%−30%) mixture and it is not sealed.

The advantages of this technology are several. Firstly the gas mixture is safe and non explosive, it has a low cost compared to other technologies such as solid state detectors and it can be operated in a harsh radiation environment with a very high γ-rays background such as reactors and spallation sources. Moreover they can praise high count rate capability ($\sim$ MHz/mm^2) and good resolution both in time (few ns) and in space (from $80\,\mu m$ up to few mm). Finally the multiplication region is independent from the read-out; this means that the electronics can be optimised for specific applications and possible discharges do not affect the read-out.

The GEM technology has many applications both in high energy physics [32] and in plasma diagnostics [17] [33] where a very high rate capability is needed. Another

Table 3.1: Current specifications of the GEM technology [31].

Physical quantity	**Values**
Maximum active area	200 cm x 50 cm
Flux rate	1 MHz/mm^2
Spatial resolution	40 μm
Achievable gain	10^5
Energy resolution	$15 - 20\%$
Holes pitch	140 μm
Holes diameter in copper	70 μm $\pm$ 5 μm
Maximum leakage current	10 nA at 600 V

field where the application of GEM detectors is growing is medical imaging.

In Table 3.1 the current specifications of the GEM technology are reported [31]. The rate capability reported in Table 3.1 refers to [34], where it is shown that the proportional gain, measured on a single GEM exposed to X-rays, is constant up to a flux of $\approx 1\,\mathrm{MHz/mm^2}$. A difference in the rate capability of GEMs is expected if they are exposed to neutrons instead of X-rays. Indeed, in the case of X-rays less primary charge is generated: for instance, in the same gas mixture, a 6.6 keV X-ray produces about 250 primary pairs whereas the α of the neutron capture in ^{10}B generates about 50000 pairs. For this reason with X-rays a higher gain operation is usually used with respect to neutrons. Some publications [35] [36] suggests that in presence of α particles the rate capability of GEMs tested with X or γ-rays may decrease and this would pose a potential problem. In this thesis the first measurement of the rate capability of GEMs using a neutron flux (and thus directly measuring the energy deposit from α particles) was carried out and the results are presented in the following sections.

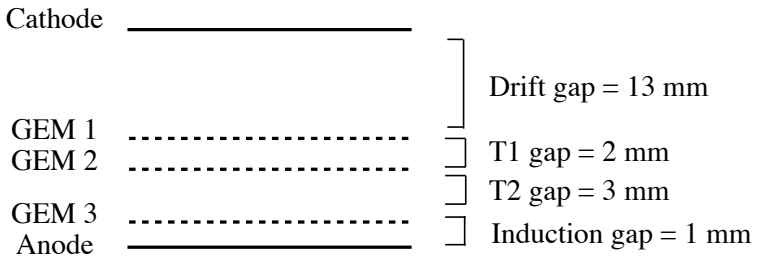

FIGURE 3.4: bGEM scheme.

3.2 bGEM description

Our bGEM is a triple GEM detector with an aluminium cathode 400 μm thick coated with a 1 μm thick film of natural boron carbide B_4C (20% of ^{10}B and 80% of ^{11}B) as neutron converter where charged byproducts are emitted through the capture reaction in ^{10}B. The gas mixture is composed by Ar/CO_2 (70%/30%): argon is a noble gas that is ionised by the charge particles and carbon dioxide is a *quenching* gas able to absorb photons emitted by the de-excitation of argon molecules excited by charge particles avoiding the creation of unwanted electronic avalanches. To guarantee a *clean* gas environment and prevent ageing and consequently discharges the flux is continuos, at a rate of about 5 l/h. The characterisation of our bGEM detector has been made at the VESUVIO [37] beam line at ISIS [38]. The working point, *i.e.* the optimum value of the voltage applied on the GEM foils to make the detector efficient and stable at the same time, is found by making a voltage scan and choosing a point lying in the *plateau*. For the bGEM this point is found to be at $\Delta V_{GEM} = 870\,V$ [16] where the gain is $G \approx 100$ and the detector sensitivity to γ-ray background is $\approx 10^{-7}$ [39]. A bGEM detector scheme is shown in Fig. 3.4 and a summary of its characteristics is reported in Table 3.2.

Table 3.2: bGEM specifications

Specifications	
Cathode	Al 400 μm
Converter	B_4C 1 μm
ΔV_{GEM}	870 V
Gain	10^2
Gas mixture	Ar/CO_2 70%30%
Gas flux	5 l/h
Drift/T1/T2/Ind	13/2/3/1 mm

3.2.1 Boron-based planar converter

In the bGEM detector the converting stage of thermal neutrons into charged particles is a 1 μm thick layer of natural boron carbide deposited on the aluminium cathode. The converter layer has been deposited with a PVD DC Magnetron Sputtering Technique at the Institute of material research at the Helmholtz-Zentrum Geesthacht [40]. The converter is based on the $^{10}B(n,\alpha)^7Li$ reaction. The thickness of the converter is chosen to be the optimum between two competing processes: efficiency of neutron conversion in α and ^7Li and the escape probability of the byproducts from the boron carbide layer.

In [41] and [26] analytical counts and simulations were made to determine the thickness of the boron layer that maximises the detector efficiency keeping into accounts different parameters, such as neutron wavelength, beam incidence angle, number of layers, etc. For thermal neutrons of 2.5 Å and multiple crossed layers (as expected in our detector geometry) the best compromise is $t_{opt} \approx 1\,\mu$m.

Since the tolerance of the deposition technique is $\approx 0.1\,\mu$m (and thus it is expected to have layers between 0.9 μm and 1.1 μm) the thickness of 1.1 μm was chosen for the following analytical calculations because it represents the worst case for the escape probability of α and ^7Li inside B_4C. Such calculations were made as follows: the

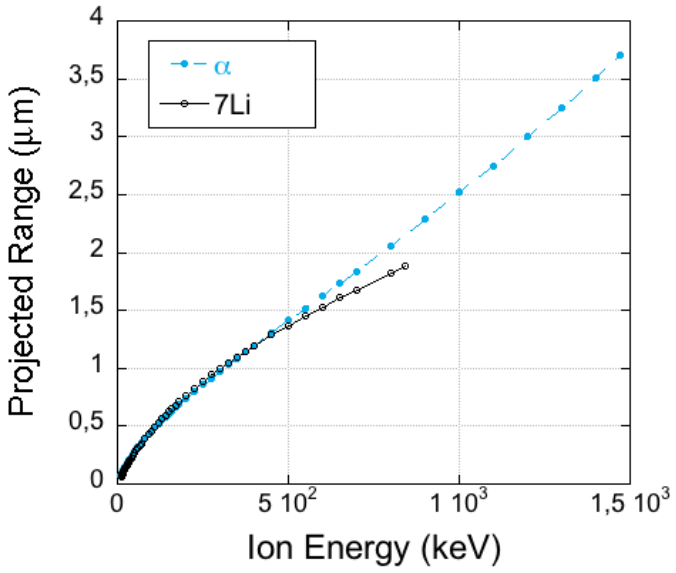

FIGURE 3.5: Range *vs* ion energy for the byproducts of the excited state (94% probability occurrence) of the neutron capture in boron carbide.

projected range, calculated with SRIM [42], of α in B_4C is $r_\alpha = 3.7\,\mu$m and the range of ^{7}Li is $r_\alpha = 1.9\,\mu$m as shown in Fig. 3.5. A density of $\rho = 2,275\,\mathrm{g/cm^3}$ was used. Consider the sphere of radius equal to the range of the byproducts (Fig. 3.6): the escape probability of $\alpha/^7$Li is the ratio of the spherical cap volume C and the semisphere volume S. Particles emitted towards the Al substrate are considered lost. The spherical cap volume, and so the escape probability, depends on the depths of the conversion d as shown in Fig. 3.7 . The ratio between the area under the escape probability curve and the entire area is the escape probability of $\alpha/^7$Li keeping into account all possible conversion depths. The resulting escape probability is 77% and 63% for α and ^{7}Li respectively is for a $1\,\mu$m thick boron layer. This value represents a lower limit because it does not take into account the attenuation of the neutron beam inside the boron carbide layer: the complete calculation can be found in [43].

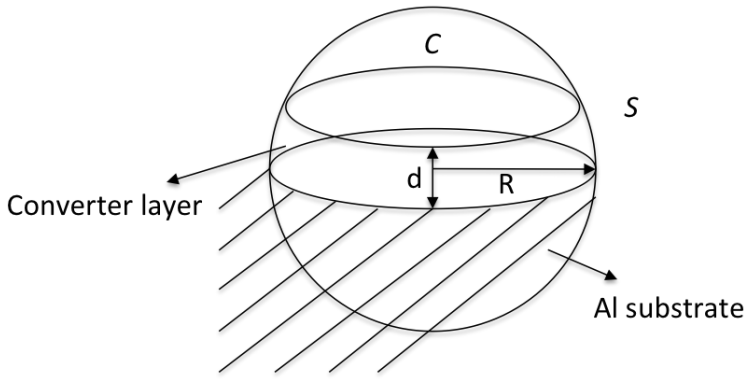

FIGURE 3.6: The sphere or radius R (R = range) represents the volume where α or ^{7}Li can be emitted after the neutron capture reaction. The shaded part represents the aluminium substrate of the cathode and d represents the depth in the thickness of the boron carbide where the capture takes place.

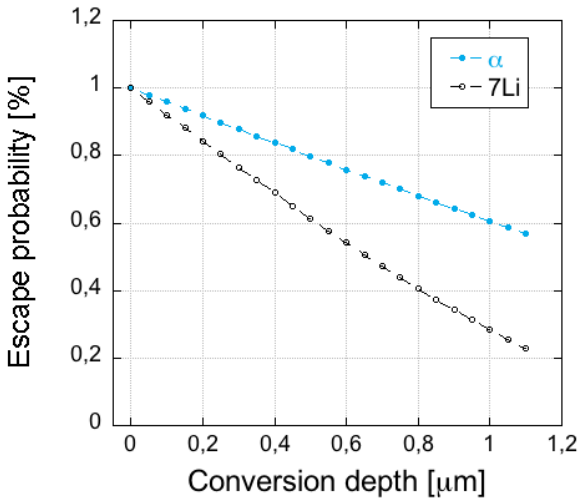

FIGURE 3.7: Analytical calculation of the escape probability of α (light blue) and ^{7}Li (black) at different depth of the B_4C converter layer.

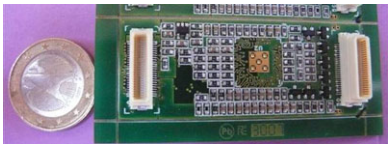

FIGURE 3.8: A CARIOCA-GEM digital chips

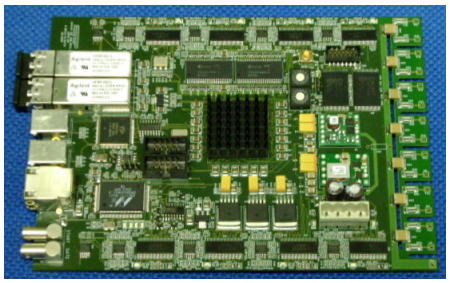

FIGURE 3.9: FPGA mother board.

3.2.2 Electronics read-out

The bGEM anode is a copper electrode with a padded readout structure with 132 pads of $8 \times 8\,\mathrm{mm}^2$ made of gold-plated few microns thick copper plus 4 L-shaped pads with area of $192\,\mathrm{mm}^2$. The total active area of the detector is $10 \times 10\,\mathrm{cm}^2$. A picture showing the padded anode is reported in Fig.1 of Paper I. The substrate of the anode is made of fiberglass which is few mm thick. The read-out electronics is composed by CARIOCA-GEM digital chips [44] (Fig. 3.8) and an FPGA mother board (Fig. 3.9) that analyses the LVDS (Low Voltage Differential Signal) signals coming from the chips. The CARIOCAs are 8 channel amplifier shaper discriminator chips designed for the LHCb experiment and later adapted for the bGEM technology [33]. The charge sensitivity of each channel is 2-3 fC and the output are time-over-threshold LVDS signals with a typical width of 10-30 ns.

3.3 Diffraction measurements

A diffraction test measurement on the INES beamline [45] at ISIS [38] was chosen, as a suitable benchmark for the GEM, for two main reasons: first of all diffraction is one of the most flexible measurements that can be performed with thermal neutrons to check the detector properties; in fact diffraction peaks are a feature easily used to study efficiency and ToF and spatial resolution. Moreover the INES instrument is especially convenient for detector tests because of the presence of a dedicated bank where detectors could be positioned and used along with ^{3}He detectors (used for comparison).

3.3.1 The INES instrument at ISIS

Two different experiments with the bGEM detector were performed on the INES diffractometer at ISIS. The first experiment was performed in April 2014 to test the performance of the detector in a diffraction experiments in term of efficiency, timing resolution and *signal-to-background ratio* (S/B). The second one was performed with a bGEM fitted with a more efficient converter and was performed in July 2014. These two experiments led to the publication of Paper II and Paper V attached to this thesis.

The ISIS neutron spallation source

The ISIS source in Didcot, UK produces neutron beams through the *spallation* process: an 800 MeV proton accelerator produces intense pulses of protons 50 times a second directed on a tungsten target. The proton energy is enough to disintegrate the heavy nuclei of the target producing neutrons, charged particles, γ-rays and heavier fragments. This technique results in an extremely intense neutron pulse (1.4×10^{16} n/s) with a neutron production yield of about 25 n/p. After production neutrons are slown down to thermal speeds by a set of hydrogenous moderators

around the target. The moderators are viewed by different neutron instruments, each optimised to explore different properties of materials.

The INES instrument

INES is a diffractometer based on the *Time-of-Flight* (*ToF*) technique with neutron wavelengths that range between 0.17 Å and 3.24 Å. The INES detector system is equipped with 144 high-pressure (20 bar) squashed ^{3}He tubes with an effective sensitive area 100.0 mm × 12.5 mm and 2.5 mm depth. The detectors are placed along a circle of 1000 mm radius centred on the sample position. The ^{3}He detectors are numbered starting from the highest scattering angle to the lowest one and they are estimated to have efficiency between 60% and 70% for neutrons in the thermal energy range [45]. A bank dedicated to detector tests is positioned at a scattering angle $\theta = 90^\circ$, symmetrically to ^{3}He tube No. 74.

3.3.2 Experimental set-up

Two different experiments were performed on the INES instrument. The first one (*Exp.1*) was carried out with the bGEM detector provided with a natural boron carbide converter (bGEM-1) and the second one (*Exp.2*) was performed with the bGEM detector equipped with a ^{10}B enriched boron carbide converter (bGEM-2). In *Exp.1* the bGEM-1 was positioned on the INES dedicated support with a scattering angle with respect to the beam equal to $\theta = 90^\circ$ as shown in Fig. 3.10. Only half of the detector area (64 pads out of 128) was connected and read through the standard ISIS Data Acquisition Electronics (*DAE*) known as *DAE2* [46] that measures the time interval $\Delta t = ToF - t_0$ between the time in which a neutron signal is generated in the detector and the time in which the pulse starts. This choice was forced by two main reasons: first of all the detector configuration parameters such as the ΔV_{GEM} , the CARIOCAs' thresholds and the starting and switching off are

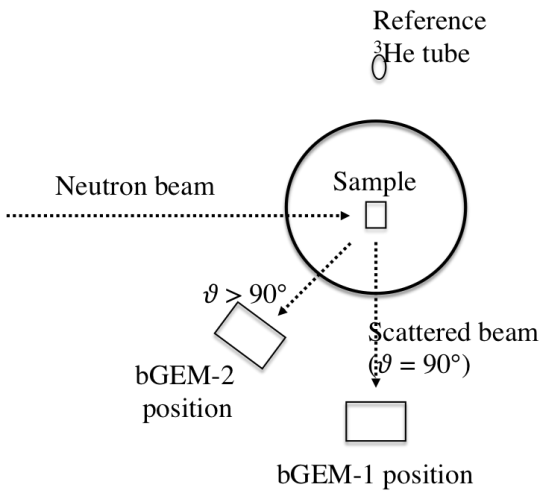

FIGURE 3.10: bGEM-1 position during the *Exp.1* and bGEM-2 position during the *Exp.2*.

managed by a Labview interface installed on a laptop, so it is necessary to have part of the bGEM-1 linked to the configuration interface. Moreover the *DAE2* allows for each pad to be connected to a different acquisition channel, but the number of *free* channels is limited by the availability of the instrument. The bGEM-1 active area was $8\,\text{mm} \times 8\,\text{mm} \times 36\,\text{pads} = 2304\,\text{mm}^2$ split in three columns, in order to better match the active area of two reference ^{3}He detectors, that is $2 \times 100\,\text{mm} \times 12.5\,\text{mm} = 2500\,\text{mm}^2$). The chosen sample was representative for a diffraction measurement and it was a bronze parallelepiped of dimensions $20\,\text{mm} \times 50\,\text{mm} \times 5\,\text{mm}$.

In *Exp.2* the bGEM-2 was positioned on a proper support in the backscattering area, *i.e.* with a scattering angle $\theta > 90^\circ$ as shown in Fig. 3.10. The configuration parameters and the connection with the *DAE2* were the same as *Exp.1*. This time the diffraction sample was a bronze parallelepiped of dimensions $10\,\text{mm} \times 60\,\text{mm} \times 60\,\text{mm}$. The copper sample was chosen because it is a good compromise between scattering intensity (to have a high counting rate) and well defined and separated diffraction peaks distributed all the way long the accessible ToF interval (0-20 ms).

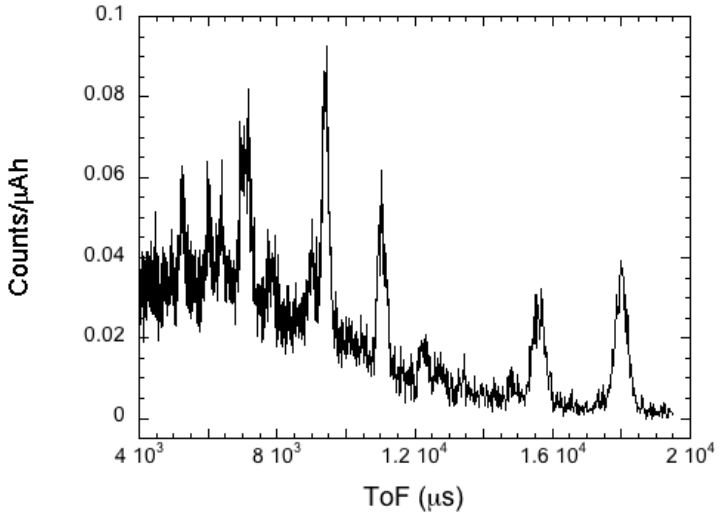

FIGURE 3.11: ToF diffractogram recorded by the bGEM-1 detector. The visible peaks represent different families planes of the crystalline solid satisfying the Bragg conditions.

The connection to the *DAE2* in both the experiments was made with a FPGA mother board that analyses the LVDS signals from the CARIOCAs. Further details about the FPGA board operation are described in Paper II. The *lower level discriminator* (LLD) thresholds in the CARIOCA chips were set at 1200 mV. This value had been determined in previous tests [16] to be adequate to safely remove the electronic noise; such tests also showed that with the applied voltage used in the two experiments ($\Delta V_{GEM} = 870\,V$) the detector sensitivity to gamma-ray background is negligible, $\approx 10^{-7}$ compared to a detector efficiency for thermal neutrons of $\approx 10^{-2}$ [47].

3.3.3 Results and Performances

The bGEM-1 and bGEM-2 diffractograms are shown in Fig. 3.11 and in Fig. 3.12 respectively. These plots were obtained starting from the raw data collected by the

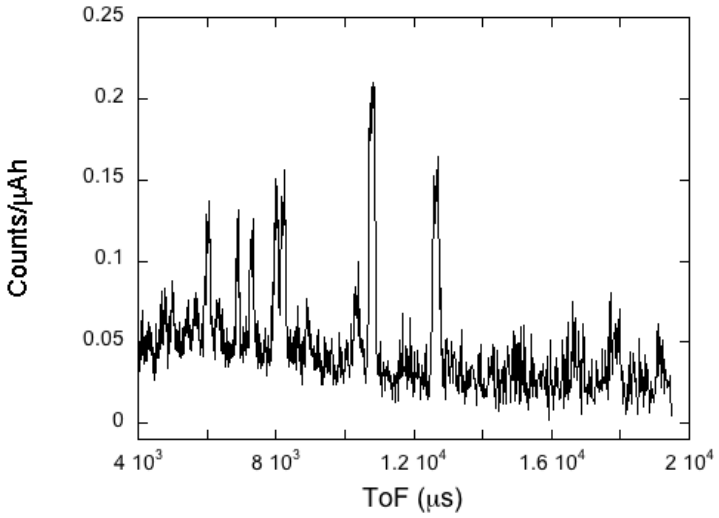

(a)

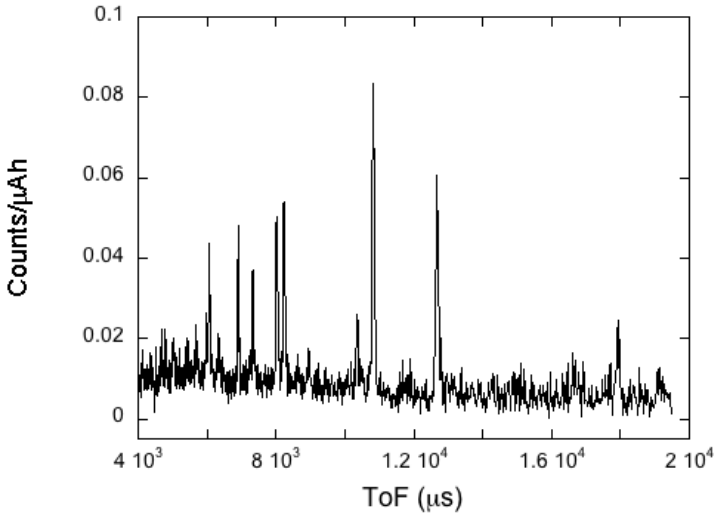

(b)

FIGURE 3.12: ToF diffractogram detected by the bGEM-2 detector without (a) and with (b) the *focussing* procedure.

DAE2 during the two experiments and using a series of algorithms inside the *MantidPlot Package* [48] [49] interfaced with the INES instrument. Since each bGEM pad is coupled to a separate *DAE2* channel, the relevant ToF spectra, each corresponding to a pad, have been summed, rebinned and normalised by the integrated current of the measurement (*i.e.* the total proton charge on the target). The data are thus presented in the form of counts/μAh *vs* time (μs). Each figure represents a ToF diffractogram of the sample: the visible peaks are the Bragg peaks due to the different Miller planes of the sample phase (*i.e.* copper). Identification of observed peaks can be found in Table 1 of Paper II. In Fig.2 of Paper II the comparison with the corresponding ^{3}He reference detectors is shown.

Efficiency

Since the flux of the beam scattered on the sample is not known *a priori*, it is not possible to perform an absolute efficiency measurement. Moreover the differences in setup of the two experiments may cause discrepancies in the measured efficiency (for instance, due to different background conditions and/or textured samples). For this reason a comparison was made of the bGEM and ^{3}He counting rate. The neutron efficiency to thermal neutrons (1.8 Å) increased by a factor 4 for bGEM-2 relative to bGEM-1. Setup uncertainties may easily be responsible for the small discrepancy regarding the expected increase in efficiency due to the use of an enriched cathode. In Table 5 of Paper V the expected ratios of bGEMs count rates with respect to an ideal ^{3}He tube with a 65% efficiency and the ratios of measured count rates of the bGEM detectors with respect to the respective ^{3}He tubes on INES are reported in greater detail as resulting from a quantitative analysis of the data in Fig. 3.11 and Fig. 3.12(b).

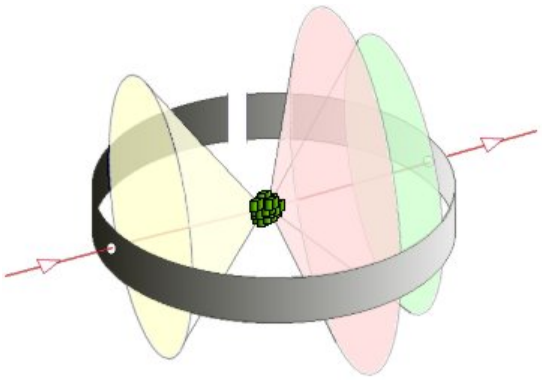

FIGURE 3.13: Representation of Debye-Scherrer cones due to neutron diffraction on a randomly oriented polycrystalline sample.

Timing resolution and Signal-to-background ratio

In Table 2 and 3 of Paper V we report the FWHM values of relevant peaks in the time diffractograms collected in *Exp.1* and *Exp.2*, respectively, and the comparison with the corresponding values for ^{3}He tubes.

The difference in timing resolution between the bGEM-1 and the ^{3}He detectors is dominated by the wider angular extension of the bGEM. Indeed the full sensible area used in the measurement spanned about 2.6° compared to about 1° for the two adjacent ^{3}He tubes, thus causing a loss of angular resolution. The plot referring to the *Exp.2* in Fig. 3.12 is the result of the *focusing procedure*. A randomly oriented polycrystalline sample (*e.g.* a powder) contains a very large number of crystallites. A beam impinging on the sample will find a representative number of crystallites in the right orientation for diffraction. Diffraction occurs only at specific angles, those where Bragg's law (Eq. 1.1) is satisfied as explained in Sec. 1.2. At each angle of diffraction correspond a Debye-Scherrer cone [19], as shown in Fig. 3.13. The focusing technique has the aim of summing spectra of pads that lie on the same Debye-Scherrer cone, *i.e.* summing pads that have a constant $Lsin\theta$ where L is the neutron flight path and θ is the angle of the reflected radiation from the sample.

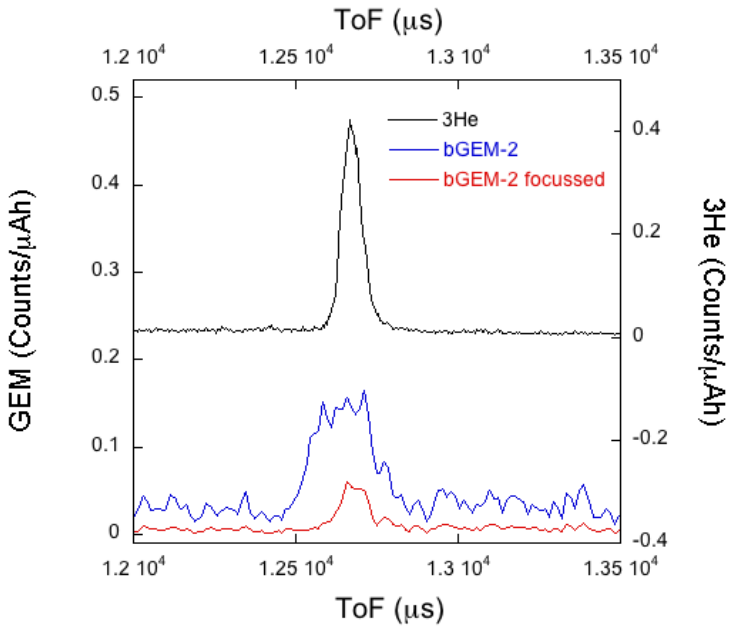

FIGURE 3.14: Comparison of a diffraction peak detected by the ^{3}He (black line), the bGEM-2 without *focussing* (blue line) and the bGEM-2 with *focussing* (red line). The FWHMs of the peaks represent the resolution of the detection system. Using the focussing technique the FWHM is reduced from FWHM=235 $\pm$ 2μs (blue line) to FWHM=94 $\pm$ 5μs (red line) to be compared with FWHM=80.1 $\pm$ 0.5μs for the ^{3}He.

When the detector is positioned at $\theta = 90°$, as in the case of *Exp.1*, pads of a single column well approximate a single Debye-Scherrer cone, as shown in Fig. 2b in Paper V. The focusing technique leads to a significant improvement in S/B with respect to straight pads columns only when the detection position is $\theta \neq 90°$. In Fig. 3.14 the peaks of the *bGEM-2* with and without focussing and the comparison with the ^{3}He tube are shown and they evidence that the timing resolutions of bGEM-2 is reduced by roughly a factor 2 and it is comparable to the ^{3}He resolution. The focussing procedure also improves the *Signal-to-background ratio* (S/B): if focusing is not applied, then S/B ratio of the bGEM is 2.8 times lower than S/B of the ^{3}He. After the focusing the S/B ratio of the bGEM becomes only 1.9 times lower than

the ^{3}He (see Paper V for details). The S/B improvement is visible by eye when comparing Fig. 3.11 and Fig. 3.12(b).

3.4 High-rate measurements

In order to fully profit from the unprecedented intensity of ESS neutron beam, with a brightness of about 7×10^{14} n/s/cm^2/sr/Å, an optimised detector should have high-rate capability while preserving good linearity. For X-rays GEM-based detector have very high-rate capabilities, up to 1 MHz/mm^2 [29]. A real detector at some point always reaches a saturation preceded by a region of limited proportionality. The results of the experiment described in this paragraph aim to show that the bGEM can reach very high rate capability and that it has slight deviation from linearity in high radiation environment.

3.4.1 ORPHEE reactor and G3-2 irradiation station

The ORPHEE reactor [50] located in Saclay, France is a 14 MW reactor with a core of very small size, highly enriched in ^{235}U which provides a thermal flux of 3×10^{14} n/cm^{2}s with a nearly Maxwellian shape peaking at a wavelength of 1.7 Å, corresponding to a neutron kinetic energy of 30 meV.

The G3-2 irradiation station is suitable for testing the high rate capability and radiation hardness of a detector. It stands 20 m from the reactor core and provides a white neutron beam peaked at 3.5 meV with a rectangular spot of 25×50 mm^2.

3.4.2 Experimental set-up

The detector used in this experiment is the bGEM-1 described in Section 3.3. The parameters of the detector are the same used in the diffraction experiment (*Exp.1*) presented in the same section. The detector was positioned on a dedicated bank in the beam. The expected neutron flux on the detector is 7.88×10^8 n/cm^{2}s. Since the

detector efficiency is estimated to be $\epsilon \approx 5\%$ the expected count rate is $\sim$ MHz/cm^2. As a reference for linearity tests, a fission chamber (FC) is added in the experimental setup in front of the detector, so that the neutron flux hitting the two devices is the same.

3.4.3 Results

To study the detector linearity two options can be considered: in the ideal case of a sufficiently accurate knowledge of the absolute neutron flux, the counts acquired by a linear detector plotted versus flux must lie on a straight line passing through the origin. On the other hand, if the flux is not exactly known, a reference detector, supposed to be *perfectly* linear, could be used as reference and a comparison between them gives information on the linearity deviation of the bGEM-1 provided the reference detector is operated in a linear regime. In this case the second experimental option was chosen. To tune the flux a series of 1.8 mm thick plastic absorbers that are credited to reduce the flux of about a factor 2 for every 1 mm were used. The non linearity results to be $\approx 20\%$ where no absorbers are used and $\approx 9\%$ with one plastic slab. For details please refer to Fig. 2 in Paper III. The maximum rate capability was found by carrying out a series of count rate measurements varying the applied voltages on the three GEM foils. A plateau is reached at $V > 850\,V$. At this point with a LLD threshold of 1300 mV a count rate of 40 MHz/cm^2 is reached. Lowering the LLD threshold to 900 mV the counting rate is enhanced to 50 MHz/cm^2. For details please refer to Fig. 3 in Paper III. A stability test was also performed to demonstrate that the bGEM can work reliably for many hours in a high neutron flux. The bGEM-1 was inserted in the full beam for 9 consecutive hours and it was found to be stable at the 0.5% level.

3.5 Conclusions

This chapter shows that the GEM technology has a good potential for thermal neutron detection. In particular excellent results are reached in terms of counting rate showing improvements of several orders of magnitude relative to ^{3}He detectors, well in excess of count rate requirements for use at ESS. The main limitation of the GEM technology is the detection efficiency, which depends on the geometry and composition of the neutron converter.

4

BAND-GEM neutron detector: first prototype

The *Boron-Array Neutron Detector* (BAND-GEM) is the first prototype of a GEM-based detector with a 3D converter (3D-C) developed during this thesis project. Different tests carried out both at reactors and spallation sources to perform a complete characterisation of the BAND-GEM and test its performance in real diffraction experiments are reported in this chapter.

4.1 From planar to 3D converters

As shown in Chapter 3, the limit of the GEM technology in thermal neutron detection does not lie in the operation principles; in fact GEMs can reach very high rate capability (MHz/mm^2), can cover large areas ($\sim$ m^2) and can reach good resolution both in time (few ns) and in space (from 80 μm up to few mm). However, limits are present in the neutron converter that is the responsible for the relatively low efficiency ($< 5\%$). The detector efficiency is the result of two competing processes: the neutron capture efficiency and the escape probability of the α and ^{7}Li byproducts from the boron carbide layer. Therefore, to enhance the efficiency it is necessary to

increase the quantity of ^{10}B crossed by neutrons and, at the same time, keep the boron layer thin enough to allow for the reaction byproducts to reach and ionise the gas. Thus, a 3D-C has been realised to be coupled to a standard GEM detector. The BAND-GEM design and its performance compared to standard ^{3}He tubes are described in this chapter and in Paper IV and V.

4.2 The BAND-GEM detector design

A sketch of the BAND-GEM detector is shown in Fig. 4.1. Starting from the bottom it is composed by a 400 μm thick aluminium $10 \times 10\,\mathrm{cm}^2$ cathode. The converter is composed of forty-eight $10 \times 6\,\mathrm{cm}^2$ *lamellas* (Fig. 4.2), each composed of 15 2 mm-wide strips of 250 μm thick alumina (Al_2O_3), coated on both sides with a 1 μm thick $^{10}B_4C$ layer. The lamellas are stacked orthogonally to the GEM foils one next to the other with a 2 mm gap. The converter lamellas and the GEM foils are sealed in a gas box where a constant flow of Ar/CO_2 $(70\% - 30\%)$ at room temperature and pressure is caused to flow. The lamellas are electrically biased at different voltages so that the electric field across the whole 3D-C is tunable. With a proper regulation of the field, the charged particles produced by the $^{10}B(n,\alpha)^7Li$ nuclear reaction ionise the gas and a fraction of the ionisation electrons reaches the GEM foils.

A feature of the 3D-C is that, if the whole detector is tilted by an angle ϕ with respect to the sample-detector direction, the thickness of each $^{10}B_4C$ layer crossed by the neutrons path is increased by a factor $1/sin(\phi)$ and the neutron conversion probability is enhanced accordingly (see Fig. 4.3). Moreover the absorption locations of the neutrons happen closer to the surface and consequently also the escape probability improves with the angle. The padded anode coupled to the GEM is in this case composed of 128 $6 \times 12\,\mathrm{mm}^2$ pads.

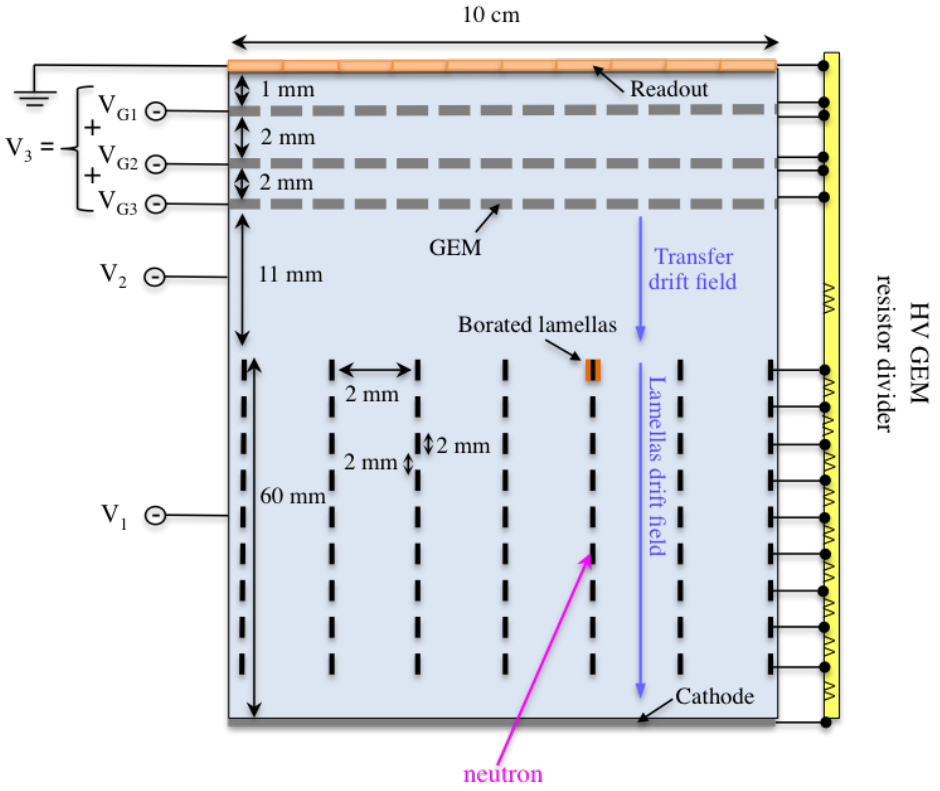

FIGURE 4.1: Global sketch of the BAND-GEM detector. After $^{10}B(n,\alpha)^7Li$ nuclear reaction if one of the two byproducts can reach the gas it ionises the mixture and a primary electronic charge is created. The drift field along the 6cm 3D-C is kept uniform by the voltage divider on the strips and it leads the electrons towards the GEM foils.

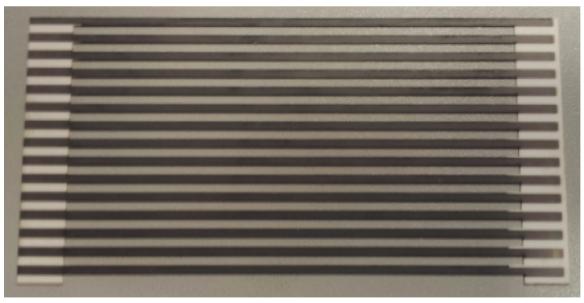

FIGURE 4.2: Photo of an Al_2O_3 lamella ($10 \times 6\,cm^2$), coated on both sides with a $1\,\mu m$ thick $^{10}B_4C$ layer. The lamella is composed by 15 2 mm-wide strips. The space between the strips is 2 mm.

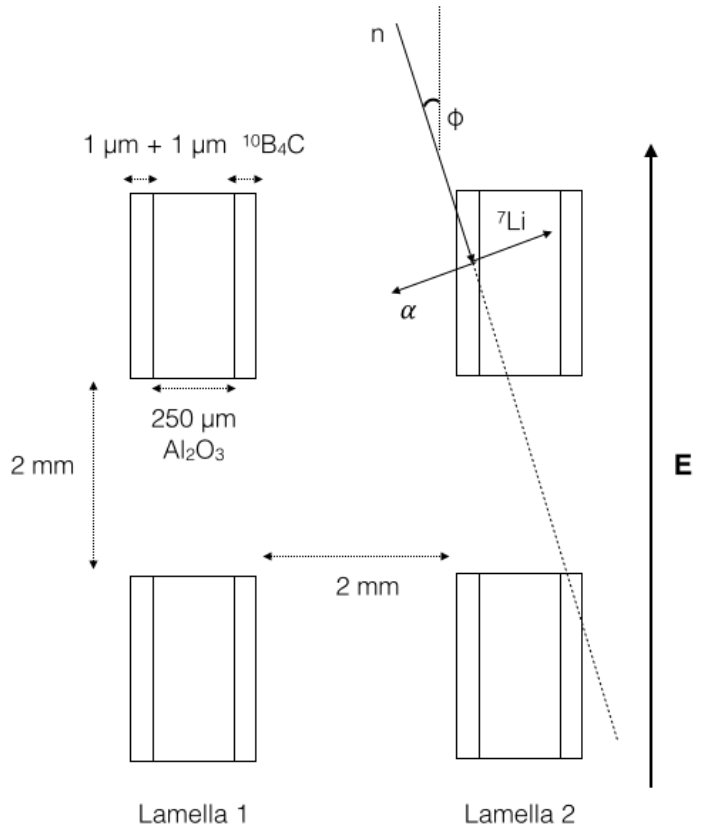

FIGURE 4.3: 4 strips belonging to 2 different lamellas are shown. ϕ is the tilt angle of the detector in the neutron beam. α and ^{7}Li produced in the $^{10}\mathrm{B}(n,\alpha)^7\mathrm{Li}$ nuclear reaction are emitted back-to-back. The electric field due to the voltage divider on the strips directs electrons from ionisation towards the GEM foils.

4.3 Neutron radiography analysis

In order to estimate the detector performance, it is necessary to carry out a complete characterisation of the converter deposition on lamellas, *i.e.* measure the converter thickness, the deposition uniformity and the atomic composition. During this PhD project a non-destructive method for diagnosing the neutron converters was developed using the advantages of the neutron radiography (or *neutrography*). The development of the diagnostic method required a set of destructive measurements, such as the Scanning Electron Microscopy (SEM), the Energy Dispersive X-ray Spectroscopy

Table 4.1: $^{10}B_4C$ coating characterisation results obtained with a set of destructive measurements on a limited number of lamellas.

Measurements	**Results**
SEM	$z = 0.90\,\mu\text{m} \pm 0.05\,\mu\text{m}$
EDS	B, C, Fe, Cr, Ni, Cu
ERDA	B, C, O, Mg, Al
XPS	B (68%), C (28%), O (7%), Fe (2%)

(EDX), the Elastic Recoil Detection Analysis (ERDA) and the X-ray photoelectron spectroscopy (XPS), on a limited number of samples to complement and make a comparison with the neutrography results obtained on the ROTAX beam line at ISIS [51] [52]. In the next sections all the steps done to develop the above-mentioned method are described. For the sake of simplicity the elaborated method presented here is relative to a single lamella. In order to use this procedure for a large-scale production it is necessary to automate the images analysis and then use an iterative method to perform a statistic calculation of the results. This work is presented in Paper IV.

4.3.1 Destructive measurements

Destructive measurements are necessary to characterise with high precision a limited number of lamellas. Indeed the SEM measurement gives informations about the thickness of the $^{10}B_4C$ coating on alumina and the uniformity of the coating. An estimation of the impurities contained in the coating was studied with the EDS and ERDA analysis. The point-like results of these measurements are completed with the XPS analysis that shows that the atomic composition of the coating is constant all along its thickness. The destructive measurements are more deeply described in Paper IV and the results are summarised in Tab. 4.1.

4.3.2 Theoretical calculations

Non-destructive measurements can be performed using the technique of the neutron radiography that allows to reproduce an image of the sample using the attenuation properties of the imaged object. A neutron beam is used to irradiate a sample, the attenuation of the beam crossing the object is due to neutron capture and/or neutron scattering whose cross sections are different depending on the isotopes composing the sample materials. To reconstruct the image of the neutron beam attenuation after the sample, a system composed of a scintillator screen, a mirror and some lenses is used to generate a photon signal that is registered by a CCD camera. The physical law describing the attenuation of a neutron beam crossing a material is:

$$I(E) = I_0(E)e^{-\Sigma_{tot}(E)z} \tag{4.1}$$

where I_0 is the intensity of the incoming radiation, $I(E)$ is the intensity of the attenuated neutron beam after crossing the sample as a function of the neutron energy E, in this case a lamella, and z is the thickness of the crossed material. Σ_{tot} is the inverse attenuation length, *i.e.* the probability per unit path length that any type of interaction will occur. It is defined as $\Sigma_{tot} = \Sigma_{capture} + \Sigma_{scatter}$. The absorption and the scattering in the alumina substrate and other impurities in the $^{10}B_4C$ coating are one order of magnitude lower compared with the one of the boron carbide, so for simplicity only the borated film is taken into account in the beam attenuation. The inverse attenuation length can be expressed as:

$$\Sigma_{tot} \sim \frac{\rho\sigma(E)N_{Av}}{P} \tag{4.2}$$

where $\rho = 2.275\,\mathrm{g/cm^3}$ is the density of the $^{10}B_4C$ coating, $\sigma(E)$ is the ^{10}B cross section of the neutron capture, N_{Av} is the Avogadro number and P is the molecular weight. If the neutron beam used to carry out the radiography is white (*i.e.* not

monochromatic) the transmitted radiation can be written in the following form:

$$\left(\frac{I}{I_0}\right)^{expected} = \frac{\int_{E_{min}}^{E_{max}} I_0(E) e^{-\sigma(E) N_{Av} t^{expected}} \, \mathrm{d}E}{\int_{E_{min}}^{E_{max}} I_0(E) \, \mathrm{d}E} \tag{4.3}$$

where $t^{expected}$ is defined as the equivalent thickness:

$$t^{expected} = \frac{\rho z}{P} \tag{4.4}$$

that represents the number of $^{10}B_4C$ moles per unit area and can be calculated using the thickness resulting from the SEM analysis ($z = 0.9\,\mu$m) and the molecular weight obtained considering all the impurities found in the XDS analysis.

The analysis for the characterisation of the film uniformity is done by comparing the expected transmitted radiation (Eq. 4.3) and the measured one, the latter directly accessible from the image analysis. The equivalent thickness $t^{measured}$ can be extracted from the measured transmitted radiation as shown by the following calculations. Starting from the Eq. 4.1 it is possible to define the absorption probability:

$$P_{capt}(E) = 1 - e^{-\sigma(E) N_{Av} t}. \tag{4.5}$$

In the wavelength region of interest, the energy dependence for the ^{10}B cross section of the neutron capture $\sigma(E)$ can be written as:

$$\sigma(E) = \sigma(E_{th}) \sqrt{\frac{E_{th}}{E}} \tag{4.6}$$

and consequently the measured transmitted radiation can be written as:

$$\left(\frac{I}{I_0}\right)^{measured} = (1 - P_{capt}(E_{th})) \int_{E_{min}}^{E_{max}} e^{-\sqrt{E_{th}/E}} \, \mathrm{d}E. \tag{4.7}$$

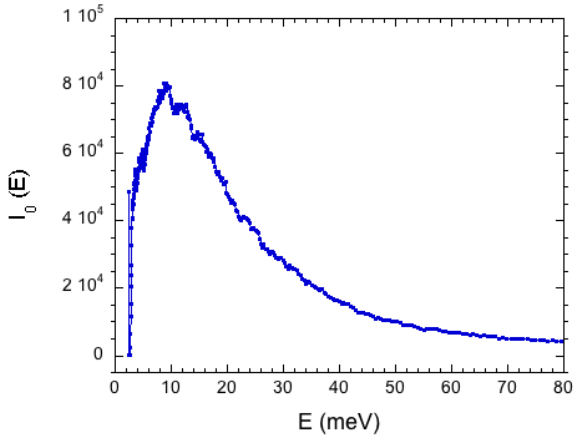

FIGURE 4.4: Measured neutron beam spectrum in the ROTAX beam line used for the neutrography.

By further developing this equation the following expression for the measured equivalent thickness is obtained:

$$t^{measured} = -\frac{1}{\sigma(E_{th})N_{Av}} ln \left(\frac{(I/I_0)^{measured}}{\int_{E_{min}}^{E_{max}} e^{-\sqrt{E_{th}/E}}\, \mathrm{d}E} \right) \tag{4.8}$$

where $(I/I_0)^{measured}$ is directly accessible from the image analysis, and the integral in the denominator can be determined from the measured neutron spectrum (Fig. 4.4).

4.3.3 Experimental set-up and image analysis

Neutron radiography measurements were performed at the ROTAX beam line at ISIS using an existing radiography-tomography system. Lamellas are irradiated with the neutron beam ($40 \times 35\,\mathrm{mm}^2$) in different positions and at different angles and the transmitted beam is collected with a scintillator screen which "converts" the incoming neutrons into photons, that are detected through a mirror by a digital

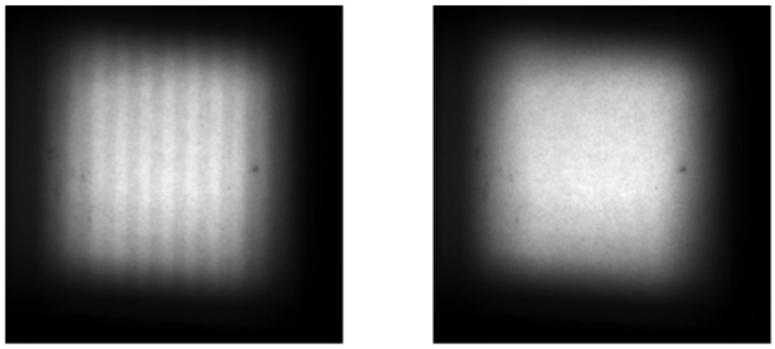

FIGURE 4.5: CCD acquisition images. (a) represents the reconstructed image of the lamella when it is inserted orthogonally with respect to the beam. The dark bands represent the absorption volume of the lamella, *i.e.* the physical strips, and the light lines are the empty spaces between strips where the beam is not attenuated. In (b) the image of the open beam (without the lamella) is shown.

camera (CCD), producing a file containing a matrix of 512×512 16-bit pixels. A typical lamella neutrography is shown in Fig. 4.5(a) while in Fig. 4.5(b) the image of the open beam, *i.e.* the ROTAX neutron beam with no sample, is shown. The analysis of the images is made with the ImageJ software [53] that allows us to do operations, such as sum, subtraction and division, on the images. To avoid the gamma-ray background due to the activation of the surrounding materials in the ROTAX block-house, a so called "dark signal" (*i.e.* the image registered when the beam shutter is closed and no sample is inside the sight view of the beam) is measured and subtracted from both images in Fig. 4.5. The resulting image intensity profiles are shown in Fig. 4.6. The data are then filtered to reduce the noise, normalised to the open beam intensity I_0 and averaged along the y axis. An example of how such data appear before and after this operation is shown in Fig.7 of Paper IV. From this plot profiles an average of the height of the peaks gives the measure of $I_0^{measured}$ while averaging the holes' values the quantity $I^{measured}$ is obtained. Once a single value of the quantity $(I/I_0)^{measured}$ has been measured for each lamella the equivalent thickness $t^{measured}$ can be extracted using the Eq. 4.8. The analysis procedure for a

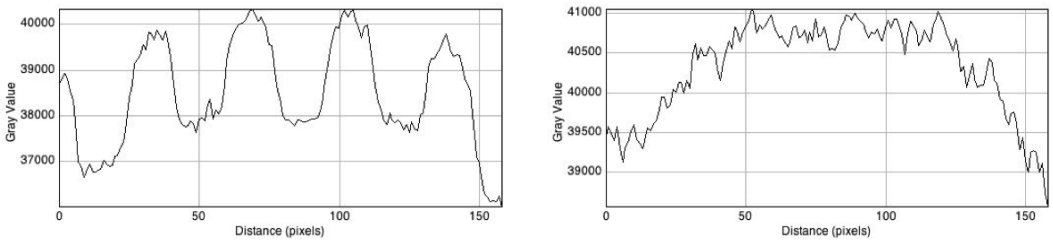

FIGURE 4.6: Image intensity profile of the intensity of the transmitted neutron beam when the sample is inserted orthogonally with respect to beam (a) and in the case of the open beam shot (b). In (a) the holes represent the strips of the lamella where the beam is absorbed, and the peaks represent the empty spaces between the strips. In (b) the intensity is higher in the centre due to neutron scattering.

single imaged lamella described in this section can be automated using an IDL code as described in Paper IV. This characterisation method was used to select 48 borated lamellas among all the available samples. A lamella is accepted if the $t^{measured}$ value differs at maximum from the 10% with respect to the $t^{expected} = 7.7 \times 10^{10}\,\mathrm{mol}/\mu\mathrm{m}^2$. In Fig.10 of Paper IV a sample of accepted lamellas with their $t^{measured}$ values is shown. In order to test the technique, some lamellas were by purpose coated with $1.1\,\mu$m of $^{10}B_4C$ instead of $1\,\mu$m. Fig. 13 in Paper IV shows that using this technique two different values of $t^{measured}$ are obtained for the lamellas with $1.1\,\mu$m and $1\,\mu$m of $^{10}B_4C$, respectively.

In conclusion this method will be used in the future to test the suitability of converters coating deposited on a substrate for the construction of neutron detectors.

4.4 Counting rate measurements versus tilt angle

The first BAND-GEM test with neutrons was performed at the JEEP-II reactor at the *Institute for Energy Technology* (IFE) in Kjeller, Norway. The choice of this laboratory was led by the need of a very well collimated beam to measure the neutron detection counting rate versus the tilt angle of the detector. Moreover during this measurement a first characterisation of the detector was made.

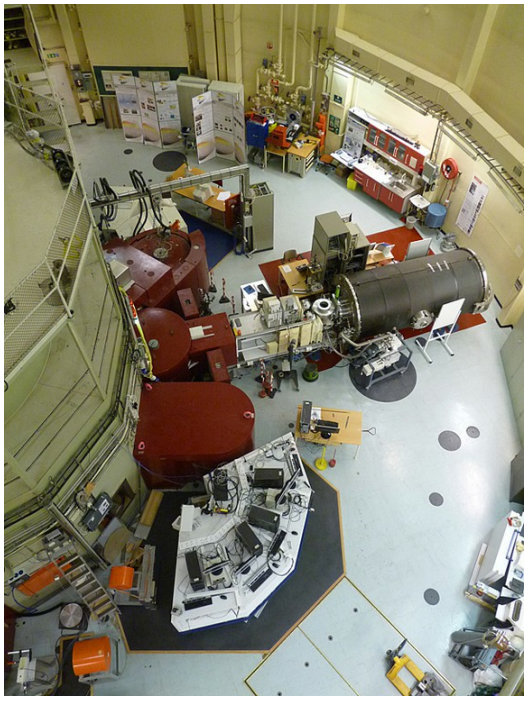

FIGURE 4.7: JEEP-II reactor hall view.

4.4.1 Experimental set-up

The JEEP-II reactor is a research reactor with a heavy water moderator with temperature $T \approx 50°\text{C}$. The reactor is operated at atmospheric pressure and the maximum thermal power is $\approx 2000\,\text{kW}$. A view of the experimental hall is shown in Fig. 4.7. The experiment was performed at the RD2D beam line positioning the detector on the rolling positioner generally used for material samples. A scheme of the experimental set-up is shown in Fig. 4.8 and a picture is shown in Fig. 4.9. The beam flux is of the order of 10^5 thermal neutrons s/cm^2 and it comes from the reactor through a shutter with two opening positions: full open or Soller collimated (*i.e.* a multiple parallel plates collimator). The Soller-type collimator in the shutter is made of Cd layers and has a 36' divergence. The beam is then monochromated by a composite Ge wafer monochromator, and exits the shielding at 90 degrees through a 30' Gd Soller collimator inserted in a borated-polyethylene tube. Two commercial slits with

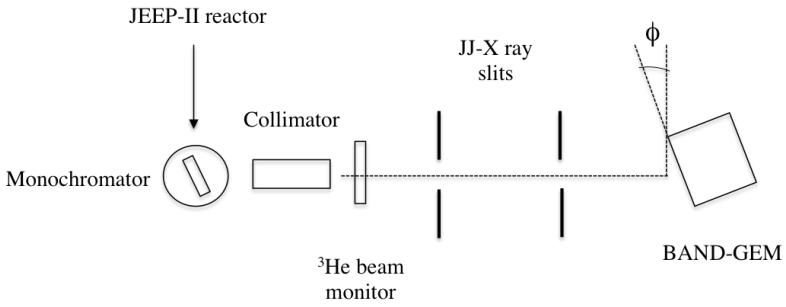

FIGURE 4.8: Scheme of the experimental setup of the first BAND-GEM test at the RD2D beam line at the JEEP-II reactor.

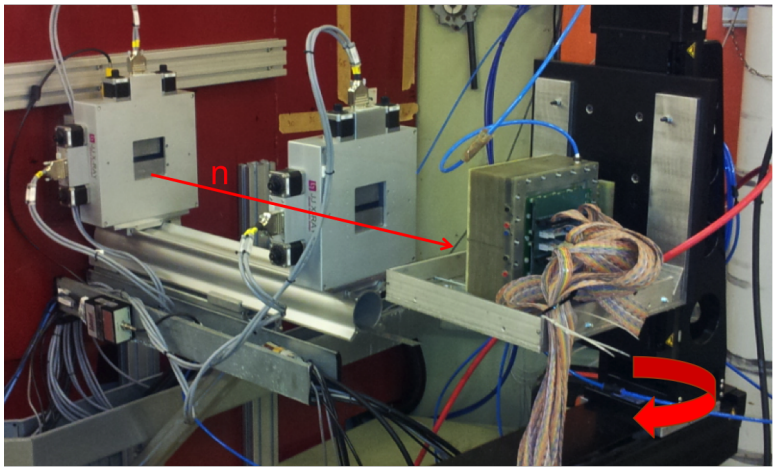

FIGURE 4.9: View of the experimental setup of the first BAND-GEM test at the RD2D beam line at the JEEP-II reactor.

borated aluminium blades are placed before the sample position where the detector stands to reduce the spot size.

Two different neutron wavelengths are available via the rotation of the monochromator: $\lambda_1 = 1.54\,\text{Å}$ corresponding to an energy $E_1 = 34.5\,\text{meV}$ and $\lambda_2 = 2\,\text{Å}$ corresponding to $E_2 = 20.45\,\text{meV}$.

The setup is motor-controlled using both commercial and in-house software.

The drift field was setup at $E_d = 230\,\text{V/cm}$, the transfer fields are $E_{T1} = E_{T2} = 3\,\text{kV/cm}$ and the induction field is $E_i = 5\,\text{kV/cm}$.

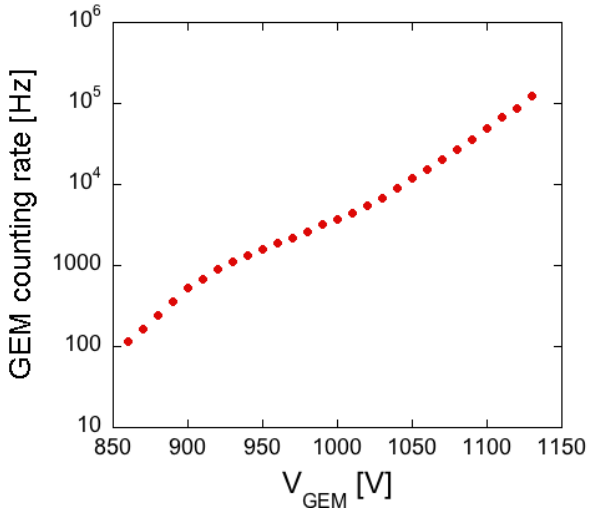

FIGURE 4.10: BAND-GEM counting rate versus the potential difference applied on the three GEM foils when a neutron beam with $\lambda_1 = 1.54\,\text{Å}$ impings on the detector with a tilt angle $\phi = 6°$. The electronic threshold applied is THR0=980 mV.

4.4.2 Performance results

In Fig. 4.10 the results of the HV scan (i.e. the scan of BAND-GEM counting rate versus the potential difference applied on the three GEM foils) is shown. This measurement allows to set the working point (as defined in Chapter 3) of the BAND-GEM. As explained in Chapter 3 the bGEM working point was set at $V_{GEM} = 870\,\text{V}$, where a counting plateau is reached and where the γ-rays background is negligible ($\approx 10^{-7}$) [39]. In the case of BAND-GEM a counting plateau is not visible. Thus, the working point was setup at $V_{GEM} = 980\,\text{V}$ where the γ-rays background is negligible as shown in Fig. 4.11.

Once the detector was set up, a counting rate measurement with respect to the tilt angle ϕ (see Fig. 4.8) is performed. In Fig. 4.12 it is possible to see the intense variation of the BAND-GEM counting rates at different tilt angles. The maximum is reached for a tilt angle $\phi \approx 7°$. Because no other parameters are changed, it can be

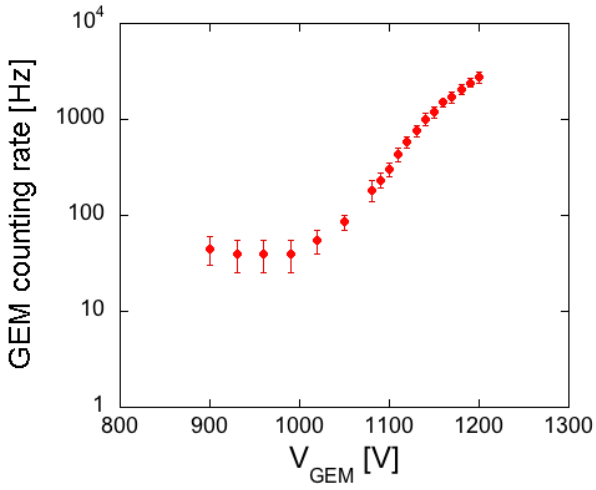

FIGURE 4.11: BAND-GEM counting rate versus the potential difference applied on the three GEM foils when a ^{127}Cs γ-ray source (662 keV) is put in front of the detector. This measurement was used to set up the working point at a ΔV where the sensitivity to γ-rays is negligible.

concluded that this strong variation is due only to the geometry of the 3D converter.

An absolute efficiency measurement with respect to the tilt angle is not possible since the neutron flux incident on the BAND-GEM detector is not known.

4.5 Diffraction measurements

Once the BAND-GEM efficiency has been studied varying the tilt angle of the detector in a neutron beam, and established that the count rate reaches its maximum for a tilt angle $\phi \approx 7^{\circ}$, the device can be used in a diffraction measurement. For the sake of coherence the diffraction experiment with the BAND-GEM has been expressly performed at the same beam line than the previous diffraction experiments with the planar cathodes detectors described in Chapter 3. In this way a complete comparison of the performances in the detector evolution can be carried out. The results concerning the improvements in performances of the three detector prototypes

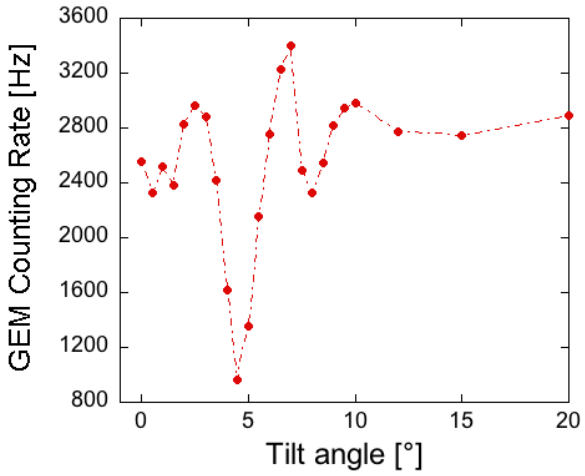

FIGURE 4.12: BAND-GEM counting rate versus the tilt angle ϕ when a neutron beam with $\lambda_1 = 1.54$Å and 9x9 mm^2 impings on the detector with a tilt angle ϕ. The potential difference applied on the GEM foils is $V_{GEM} = 980$ V.

presented in this thesis are reported in Paper V.

4.5.1 Experimental set-up

The diffraction experiment with the BAND-GEM detector was carried out at the INES instrument at ISIS, previously described in Sec. 3.3. The detector was positioned at a scattering angle $\theta = 90^\circ$ and tilted of about an angle $\phi \approx 7^\circ$ as shown in Fig. 4.13. The definition of scattering angle and titling angle are also shown in Fig. 2 of Paper V.

The sample was a bronze parallelepiped of dimensions 10mm x 60 mm x 60 mm, the same used in *Exp.2* described in Sec. 3.3.

The BAND-GEM configuration was the same used at IFE experiment described in Sec. 4.4 (*i.e.* $V_{GEM} = 950$ V, $E_d = 230$ V/cm, $E_{T1} = E_{T2} = 3$ kV/cm and $E_i = 5$ kV/cm).

A cadmium mask was constructed at the ISIS workshop and applied on the

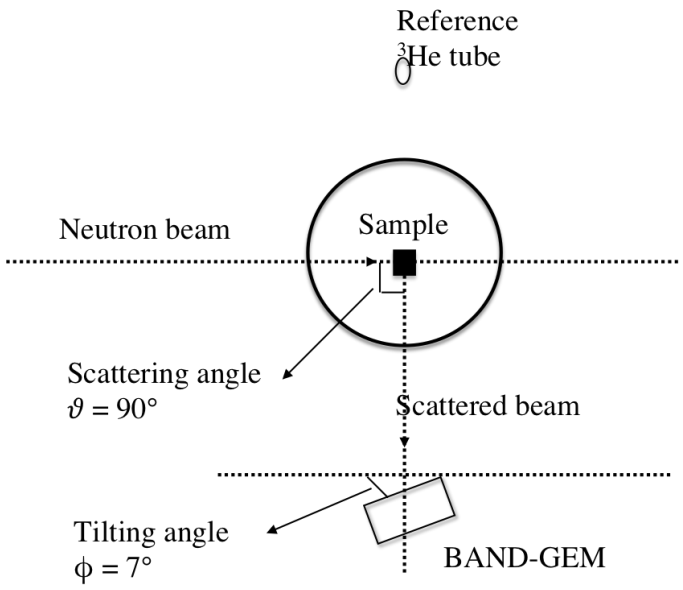

FIGURE 4.13: Experimental setup of the BAND-GEM experiment performed at the INES instrument at ISIS. The BAND-GEM was positioned on a dedicated bank placed at $\theta = 90^{\circ}$ with respect to the incident neutron beam.

BAND-GEM front face to reduce the amount of neutron scattering on the frame.

The acquisition area for this experiment was limited to a single pad column, equal to 8 x (6 x 12 mm^2), to better match the active area of the reference ^{3}He tube (active area equal to 100.0 x 12.5 mm^2 x 2.5 mm depth). Thus the following results are referred to this acquisition area.

4.5.2 Results and Performances

The BAND-GEM and ^{3}He diffractograms are shown respectively in Fig. 4.14 and in Fig. 4.15. Since each BAND-GEM pad is coupled to a separate *DAE2* channel, the relevant ToF spectra, each corresponding to a pad, have been summed, rebinned and normalised by the total proton charge on the target during the measurement using a series of standard algorithms inside the *MantidPlot Package* [48] [49].

As in the previous diffraction experiments, the ToF window is restricted from 4 ms to 20 ms to avoid the γ-rays background due to both the spallation process on

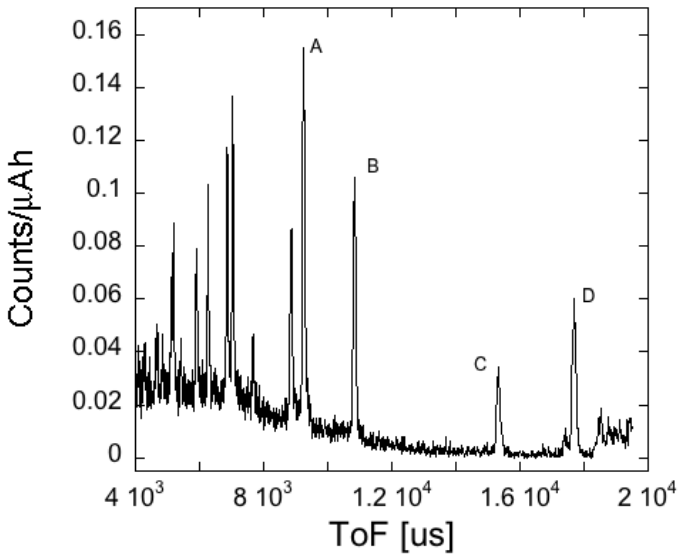

FIGURE 4.14: *ToF* diffractogram recorded by the BAND-GEM detector on the INES instrument at ISIS. The visible peaks represent different families planes of the crystalline solid satisfying the Bragg conditions.

the target, and the neutron capture in the converter and other materials in the INES block house.

For the sake of simplicity four visible peaks were chosen (named A, B, C and D), to carry out the analysis. Indeed, looking at the two diffractograms it is possiile to notice differences in the intensities of the peaks. This discrepancy is due to the fact that the sample is texturised (*i.e.* the main directions of the crystallites are not isotropically distributed but concentrated along selected directions, so the Bragg peaks result to be more intense in some directions than in others). These differences can be bypassed in the analysis if only parameters related to single peaks are taken into account, such as FWHM and S/B.

The count rate reported is integrated on the whole spectra, thus overcoming the texturing differences. The results of the fitting procedure for each peak are reported

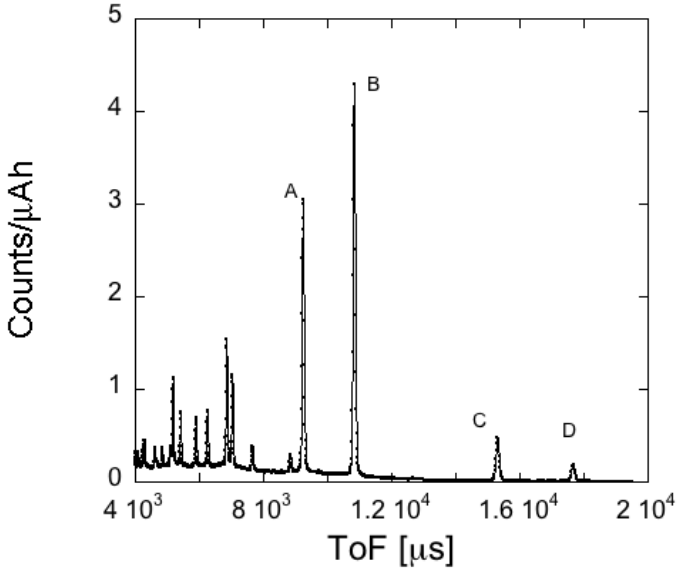

FIGURE 4.15: *ToF* diffractogram detected by the ^3He detector taken as reference.

in Table 4 in Paper V.

The precise value of the neutron flux on the copper sample is not known, and so the efficiency cannot be absolutely measured. Thus, a comparison between the BAND-GEM count rate and the ^{3}He taken as reference is made. The BAND-GEM count rate is about $\approx 25\%$ the ^{3}He count rate as shown in Table 5 in Paper V.

The timing resolution of a ToF diffraction is defined as the FWHM of a peak. The FWHM is measured using a fitting procedure inside the *MantidPlot* package as discussed in Sec. 3.3. Each peak was fitted with a Gaussian distribution and a linear background. The results of the fit for the BAND-GEM and the ^{3}He are reported in Table 4 of Paper V. From the comparison between the GEM detector and the reference tube, it is possible to see that the resolutions are compatible within about $\approx 3\sigma$.

4.5.3 Conclusions

The results of the BAND-GEM test as a neutron diffraction detector presented in this section can be compared with the results previously obtained with detectors equipped with a planar converter, presented in Sec. 3.3. Improvements in efficiency, timing resolution and S/B are visible following the detector evolution. In particular the count rate per unit area significantly increased from about 7% for the bGEM, relative to the ^{3}He count rate, to 25% for the BAND-GEM. The timing resolution of the BAND-GEM is comparable with that of ^{3}He within 3σ, and the S/B ratio of a BAND-GEM is about a factor 2 lower with respect to the ^{3}He. The evolution of GEM-based detectors from planar to 3D converters is presented in the Paper V.

5

BAND-GEM: second prototype

In this chapter the design of a second BAND-GEM prototype and the results of tests made on the EMMA [54] instrument at ISIS [38] are presented.

5.1 Limits of the first prototype

The main limitation of the first BAND-GEM prototype is the low electronic charge extraction in the 3D converter limiting the detection efficiency. The drift field (*i.e.* the electric field along the 3D converter) extracts the primary electronic charge towards the GEM foils, and it depends on the potentials applied to the 3D boundaries and the first GEM foil. In Fig.7 of Paper V the field lines between two different lamellas of the first prototype, simulated using the Ansys software [55] [56], are shown. For the sake of simplicity the field lines could be considered as the preferred electron trajectories. It can be noticed that at least one third of the electrons trajectories are projected through the next pair of electrodes and lost. The charge extraction efficiency can be improved by optimising the geometry of the converter, for instance by increasing the distance between lamellas. Herein a description of the second prototype and the results of the experiment on EMMA are reported; a com-

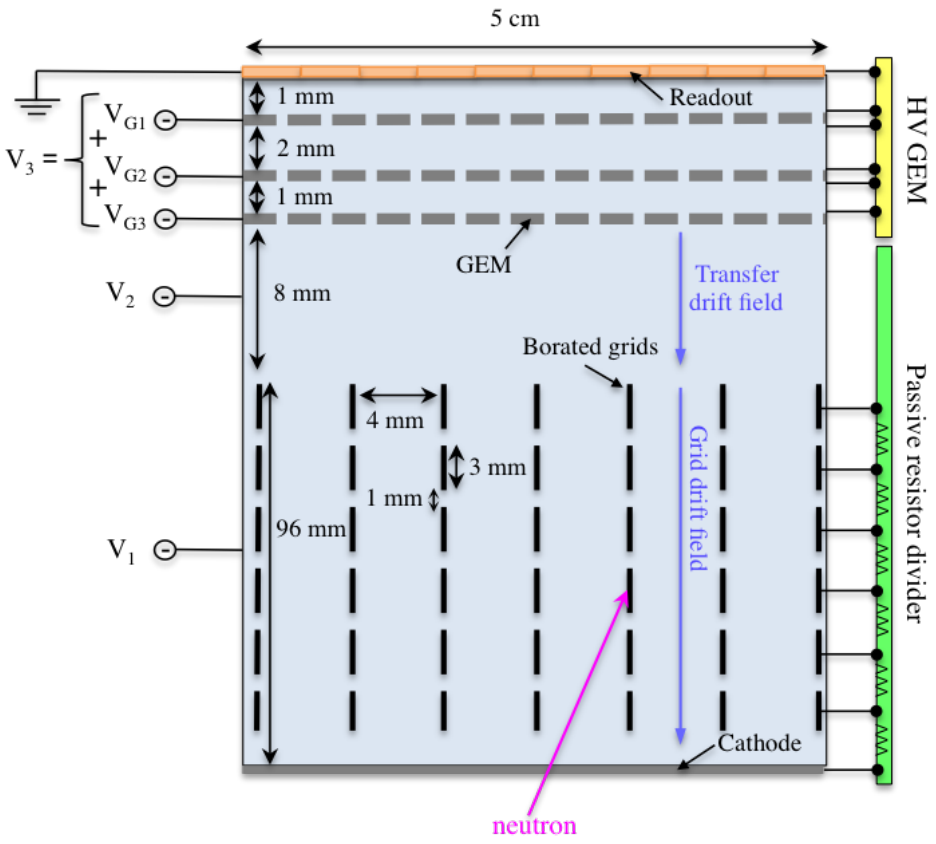

FIGURE 5.1: Scheme of the new BAND-GEM prototype with active area of $5 \times 10\,\mathrm{cm}^2$.

plete description of the optimisation study leading to the construction of the second prototype will be described in future publications, along with the feasibility study of the converter practical realisation.

5.2 Second prototype design

The scheme of the new BAND-GEM prototype is shown in Fig. 5.1. The detector has an active area of $5 \times 10\,\mathrm{cm}^2$. Starting from the bottom of the sketch there is the cathode: a $400\,\mu$m thick aluminium foil. The 3D converter is made of twenty-four aluminium grids (Fig. 5.2) coated with $1\,\mu$m of $^{10}B_4C$ and stacked on the cathode. Each grid is 3 mm high, has an overall area of $12 \times 7\,\mathrm{cm}^2$ and is composed by eleven

FIGURE 5.2: Aluminium grid used for the 3D converter of the new BAND-GEM prototype. The frame hosts some holes for grids alignment.

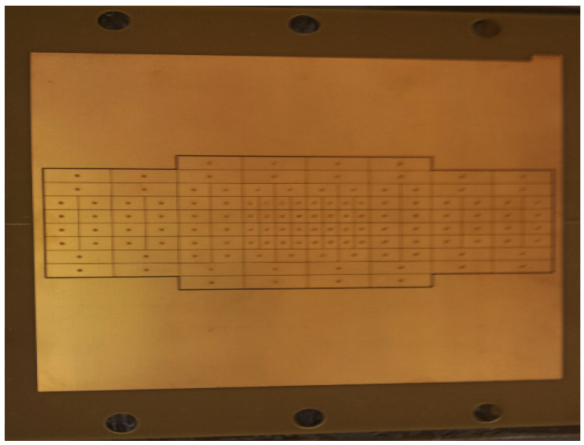

FIGURE 5.3: Padded anode used for the new BAND-GEM prototype. The pads have three different dimensions, $4 \times 3\,\mathrm{mm}^2$ the smallest, $4 \times 6\,\mathrm{mm}^2$ the intermediate and $4 \times 12\,\mathrm{mm}^2$ the largest.

strips 10 cm long, 3 mm high and 200 μm thick. The pitch between the strips is 4 mm. Three standard GEM foils and an anode with pads of different dimensions (Fig. 5.3) are placed on top of the borated grid stack.

During the boron deposition process [57] [58] the high temperature ($\approx 400^{\circ}$C) causes deformation of the aluminium and a tensioning is required to bring the strips straight again. The tensioning is made through screws hosted in the side holes of the grids frame.

Each grid is kept at a different voltage through passive resistor divider outlined

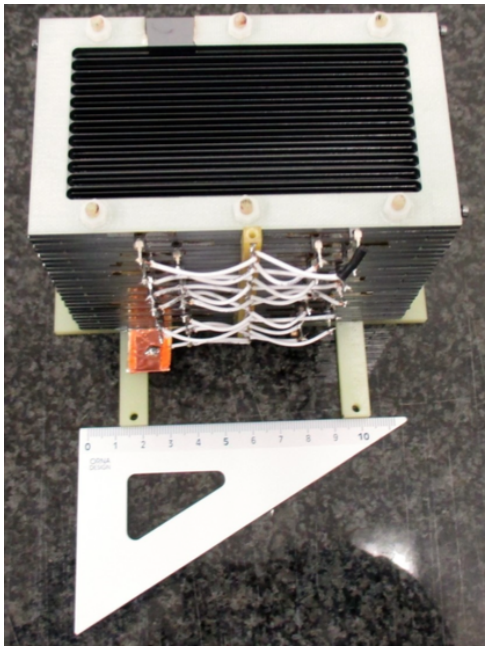

FIGURE 5.4: View of the 3D converter in the BAND-GEM with electrical contacts.

in Fig. 5.1 so that a uniform drift field is created along the conversion region. A picture of the 3D converter and the corresponding divider is shown in Fig. 5.4. The voltage difference on each GEM foil is provided by a standard HV GEM module [59]. The anode with different pad dimensions has been chosen to study the effect of the pad dimensions on the spatial resolution and multiple hits.

5.3 Detector test

The detector was tested for the first time with a neutron beam on the EMMA instrument at ISIS. The aim of the experiment was to do a characterisation of the detector, and measure the efficiency of the detector with respect to the tilt angle and the neutron wavelength. This experiment demonstrated the detector suitability for neutron scattering applications, such as diffraction or SANS.

The EMMA instrument at ISIS, the experimental setup and finally the characterisation and the test results are presented in Sec. 5.3.1, Sec. 5.3.2 and Sec 5.3.3

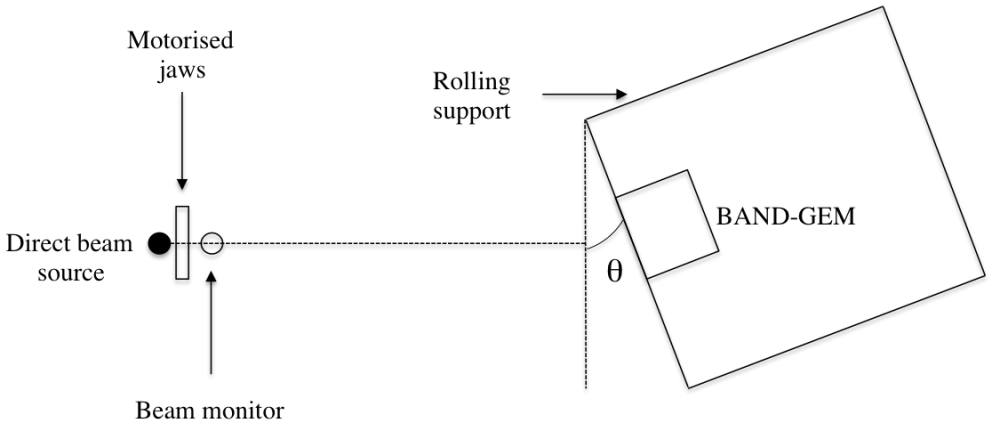

FIGURE 5.5: Scheme of the experimental setup on EMMA.

respectively.

5.3.1 EMMA instrument

EMMA is a new instrument at ISIS. It is located at the place of the previous HET instrument [54]. The EMMA beam has dimensions $45 \times 45\,\mathrm{mm}^2$, but motorised jaws can define smaller beam sizes. The sample position is 16 m from the moderator and it is provided with a rotating and movable support.

The range of neutron wavelength is about $\lambda \in [1 - 4\,\text{Å}]$ corresponding to the energy range $E_n \in [5 - 81\,\mathrm{meV}]$.

The incident beam monitor, positioned immediately after the jaws, is a commercial GS-20 Lithium Glass Scintillator [60] with an efficiency at $\lambda = 1\,\text{Å}$ of $\epsilon = 0.60\% \pm 0.06\%$. The beam monitor efficiency scales linearly with λ in the range of interest $\lambda \in [1 - 4\,\text{Å}]$.

5.3.2 Experimental set-up

A scheme of the EMMA instrument is shown in Fig. 5.5. For the entire experiment the beam dimensions were set to $4 \times 4\,\mathrm{mm}^2$.

Different setups were used for the various measurements performed, as sum-

Table 5.1: EMMA experimental setups. θ is the tilt angle of the movable support. The potential difference V_1, V_2 and V_3 are defined in Fig. 5.1.

Experimental setup	**Measurements**
$\theta = 0^\circ$	V_1, V_2, V_3
$\theta = 90^\circ$	z scan
$\theta \in [0^\circ - 6^\circ]$	efficiency
$\theta \in [0^\circ - 5^\circ]$	FWHM
$\theta = 5^\circ$, $\lambda \in [1\AA - 4\AA]$	efficiency

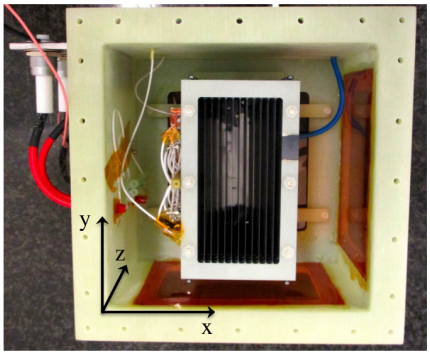

FIGURE 5.6: Definition of x,y and z axis used in the experiment.

marised in Table 5.1. The definition of the x, y and z axis is shown in Fig. 5.6 where two diagnostic windows are visible on the cathode plane (xy) and along the 3D converter. In Fig. 5.7 the setups for $\theta = 0^\circ$, with the cathode facing the beam source and $\theta = 90^\circ$ where the beam hits the side of the 3D converter passing through a diagnostic window are shown.

5.3.3 Performance results

The data analysis was performed with the *MantidPlot Package* [48] [49]. Since each BAND-GEM pad is coupled to a separate data acquisition channel, the relevant ToF spectra, each corresponding to a pad, have been summed, rebinned and normalised by the total proton charge on the target during the measurement using a series of standard algorithms inside the above-named software.

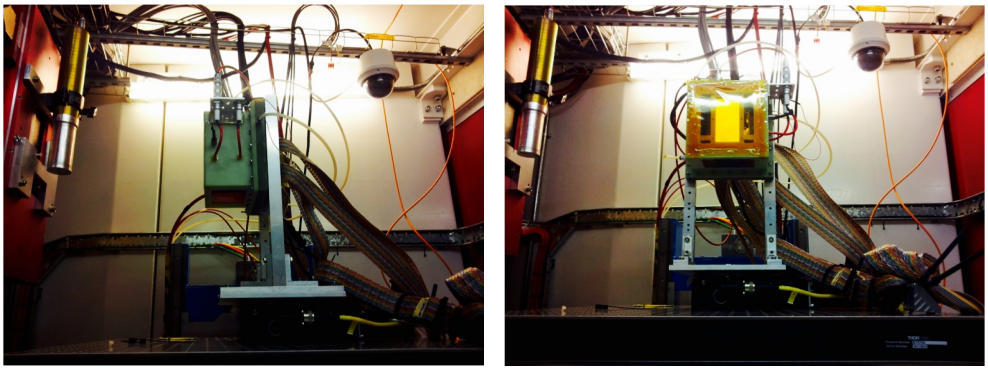

FIGURE 5.7: BAND-GEM setup on EMMA for $\theta = 0°$ and $\theta = 90°$.

Electrical characterisation

In Fig. 5.8 the ToF spectra of a single BAND-GEM pad and the beam monitor are shown. A threshold on the ToF and consequently on the neutron wavelength is chosen at $t = 4\,\text{ms}$ corresponding to a wavelength of $\lambda = 1\,\text{Å}$. Thus, the "GEM counts" referred to in Fig. 5.8 are defined as:

$$I_{BAND-GEM} = \int_{t=4ms}^{t=20ms} BandGEM(t)dt \tag{5.1}$$

i.e. counts due to neutrons with wavelength $\lambda > 1\,\text{Å}$. The same definition applies to the monitor counts:

$$I_{monitor} = \int_{t=4ms}^{t=20ms} Monitor(t)dt. \tag{5.2}$$

The efficiency of the detector can be estimated as:

$$\epsilon_{BAND-GEM}(\lambda(t)) = \frac{I_{BAND-GEM}(\lambda(t))}{I_{monitor}(\lambda(t))} \times \epsilon_{monitor}. \tag{5.3}$$

HV scans were performed to determine the working point (*i.e* the optimised bias) of the three V_i (see Fig. 5.1). By comparing figures Fig. 5.9, Fig. 5.10 and Fig. 5.11 it can be noticed that:

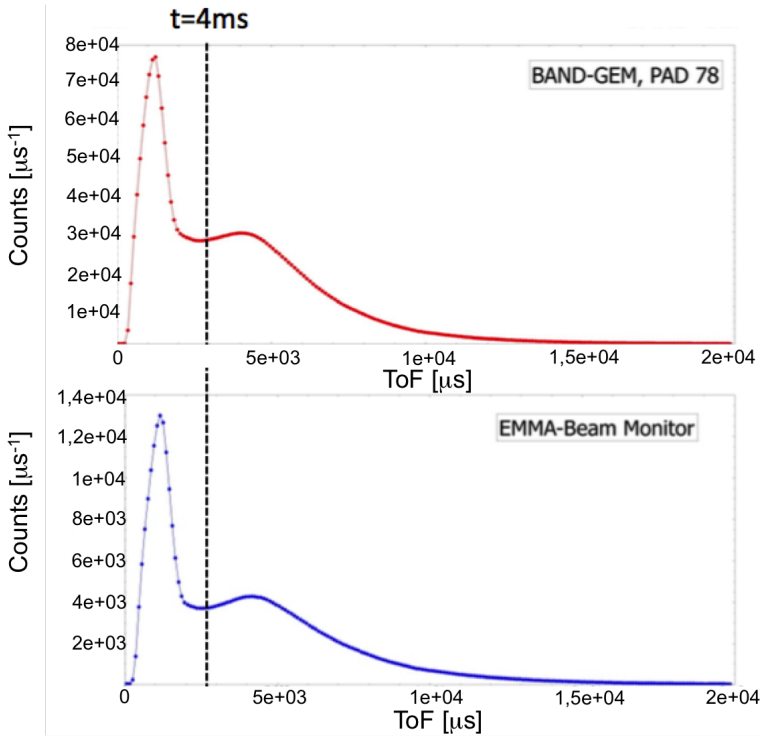

FIGURE 5.8: Time of flight spectrum recorded by one BAND-GEM pad (top) and the beam monitor (bottom) on the EMMA instrument.

- the count rate has a strong dependence on V_1. The $I_{BAND-GEM}$ versus V_1 shows a plateau at high voltages and the working point was set at $V_1 = 11.1\,\mathrm{kV}$;
- the count rate only has a weak dependence on V_2 (working point set at $V_2 = 1500\,\mathrm{V}$);
- being the BAND-GEM in principle sensitive to γ-rays, a V_3 scan was performed (as described in Chapter 3) to set the working point of this parameter: $V_3 = 900\,\mathrm{V}$. A 1 mm cadmium sheet was used as a γ-rays source towards the neutron capture reaction $^{113}\mathrm{Cd}(\mathrm{n},\gamma)^{114}\mathrm{Cd}$. This cadmium thickness is sufficient to guarantee a complete slow neutron absorption and a consequent γ-rays are emission.

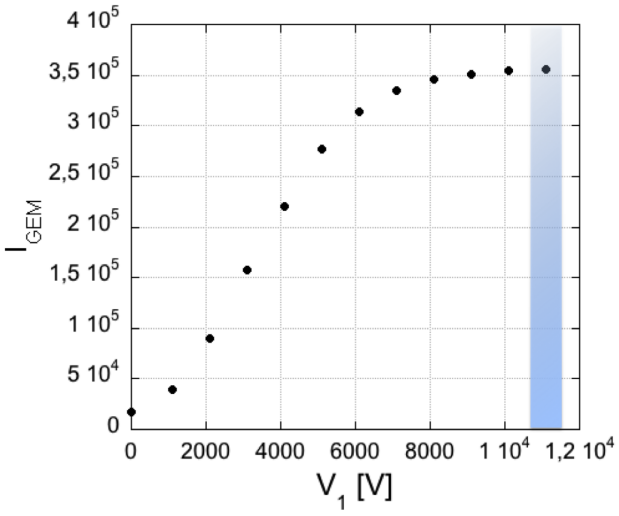

FIGURE 5.9: Scan of the voltage between the top of the 3D converter and the cathode (V_1 in Fig. 5.1). $V_2 = 1500\,\mathrm{V}$ and $V_3 = 900\,\mathrm{V}$. The counts of the BAND-GEM on the y axis are defined as the BAND-GEM counts above 1Å (see Eq. 5.1).

Having thus confirmed that the field inside the 3D converter is the most critical parameter for charge collection, a measurement of the relative charge extraction efficiency along the 3D converter from $z = 0\,\mathrm{mm}$ and $z = 96\,\mathrm{mm}$ was done by making a scan along the depth of the detector positioned at $\theta = 90°$. In Fig. 5.12 the plots of the z scan for six different values of V_1 are shown. Since the width of the lateral diagnostic window is $\sim 75\,\mathrm{mm}$ the neutrons that hit the detector at lowest and highest z are blocked by the frame. However the values of $I_{BAND-GEM}$ for such extremes z can be extrapolated from the measured ones (see Fig. 5.12 where the extrapolation is shown in blue). The relative charge extraction efficiency η_C is defined as:

$$\eta_C = \frac{I_{BAND-GEM}(z = 0\,\mathrm{mm})}{I_{BAND-GEM}(z = 96\,\mathrm{mm})} \tag{5.4}$$

and the values for different applied V_1 are summarised in Table 5.2. Ideally one would like η_C to be as close as possible to unity, that means that the charge extraction

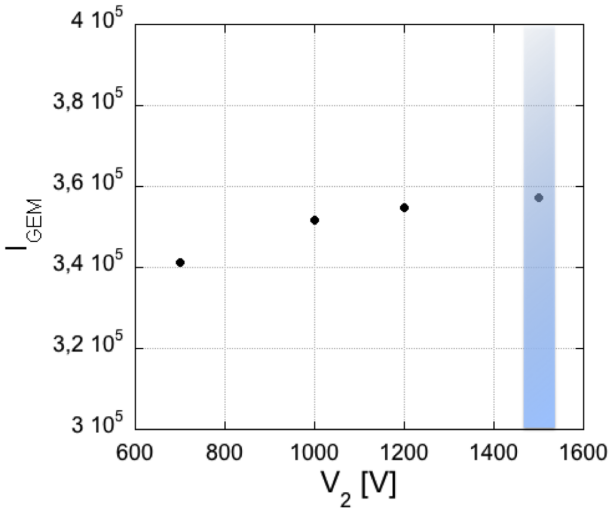

FIGURE 5.10: Scan of the voltage between the bottom of the last GEM foil and the top of the 3D converter (V_2 in Fig. 5.1). $V_1 = 11.1\,\mathrm{kV}$ and $V_3 = 900\,\mathrm{V}$. The counts of the BAND-GEM on the y axis are defined as the integral of the BAND-GEM counts above 1Å (see Eq. 5.1).

efficiency is uniform along the whole 3D converter. The panels of Fig. 5.12 show that this is not quite the case and that a fraction of charge is always lost inside the 3D converter. The linear dependence of $I_{BAND-GEM}$ on z is probably due to charges diffusing and hitting the grids. The last panel of such figure however shows that at too low voltages the charge extraction is incomplete even at z = 96 mm *i.e.* even when no obstacles are present on the electron paths.

Efficiency measurements

Since the flux of the EMMA instrument is not precisely known, an absolute efficiency measurement is not possible. Consequently the efficiency was measured relatively to the beam monitor (Eq. 5.3). The efficiency estimated in such a way is shown in Fig. 5.13 for neutrons of 1 Å and 2 Å as function of the tilt angle θ. The observed dependence $\epsilon(\lambda)$ can be explained as follows: it is a consequence of the loss of charge

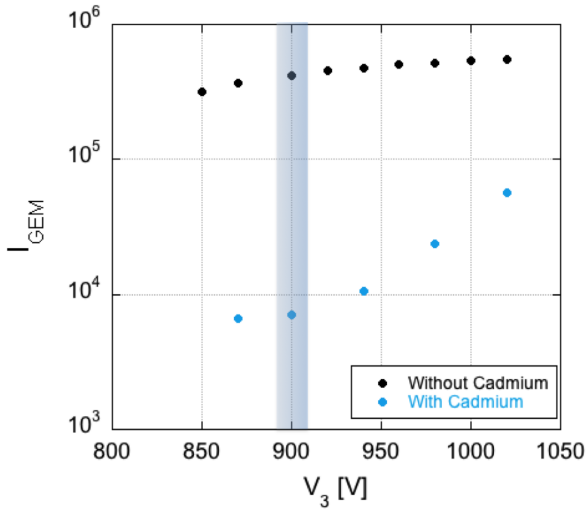

FIGURE 5.11: Scan of the voltage along the GEM foils (V_3 in Fig. 5.1) with (blue) and without (black) a 1 mm cadmium foil inserted in the beam. The voltage between the top of the 3D converter and the cathode is $V_1 = 11.1\,\text{kV}$ and the potential difference between the bottom of the GEM foils and the top of the 3D converter is $V_2 = 1500\,\text{V}$.

from the $z = 0\,\text{mm}$ extremity of the 3D converter. Higher wavelength neutrons have a higher probability to be absorbed into the very first boron layers; thus a higher fraction of the electrons they produced is lost. Lower wavelength neutrons are comparatively absorbed all along the 3D converter, even into the boron layers closest to the GEMs, thus resulting in a lower fraction of electrons being lost. In Fig. 5.14 the measured efficiency of the BAND-GEM versus the neutron wavelength for a tilt angle equal to $\theta = 5^\circ$ is shown.

Spatial resolution measurements

Even in the ideal case one neutron trajectory could give signals in N adjacent gaps and so more than one pad per event can collect charge. This is due to the probability p of a neutron to be absorbed in a single strip (each made of two boron layers). p only depends on the boron capture cross section and the angle at which the strip is

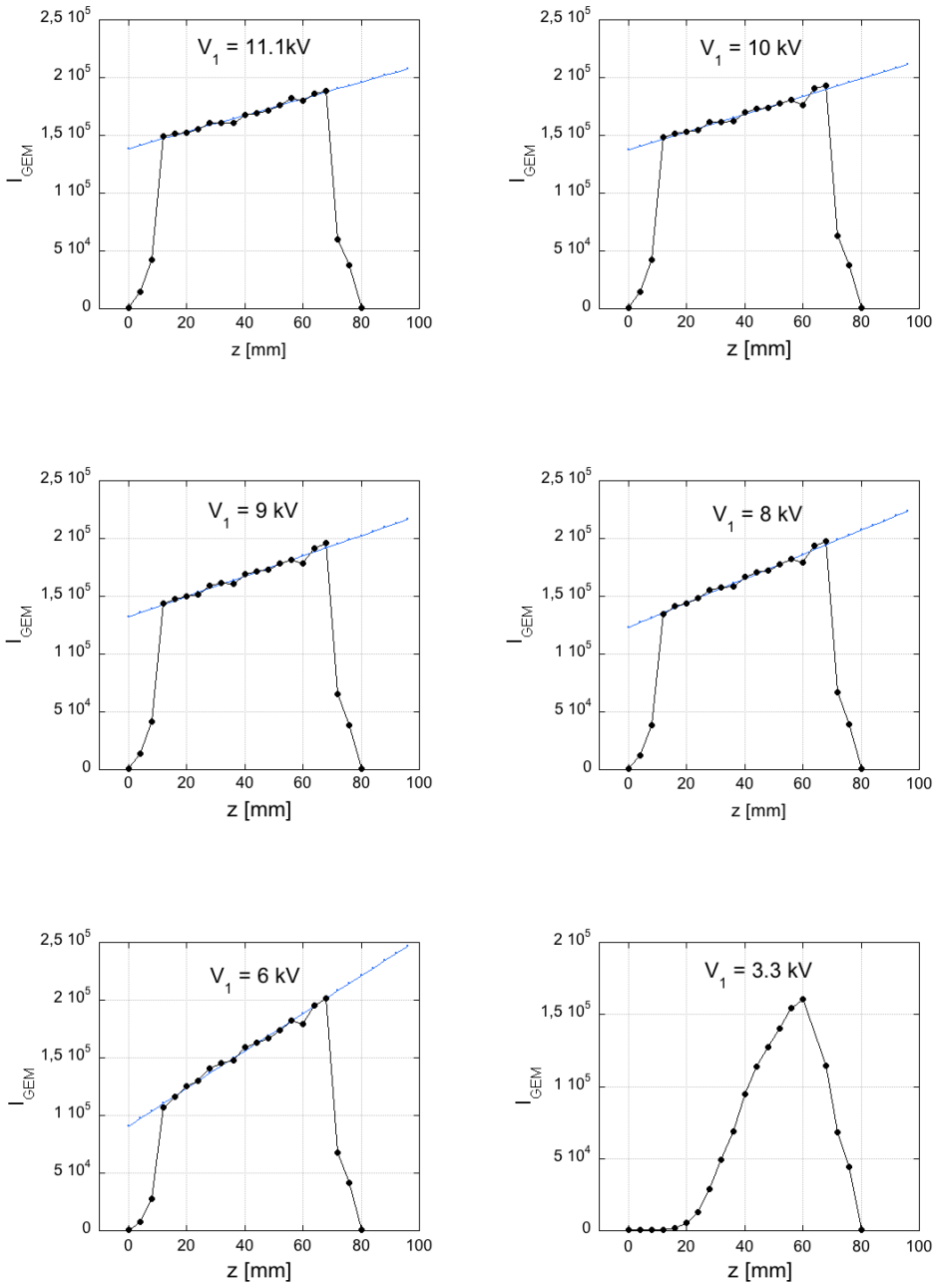

FIGURE 5.12: Scan along the depth of the BAND-GEM starting from the bottom of the cathode at $z = 0\,\text{mm}$ and the top of the 3D converter at $z = 96\,\text{mm}$ for six different values of V_1.

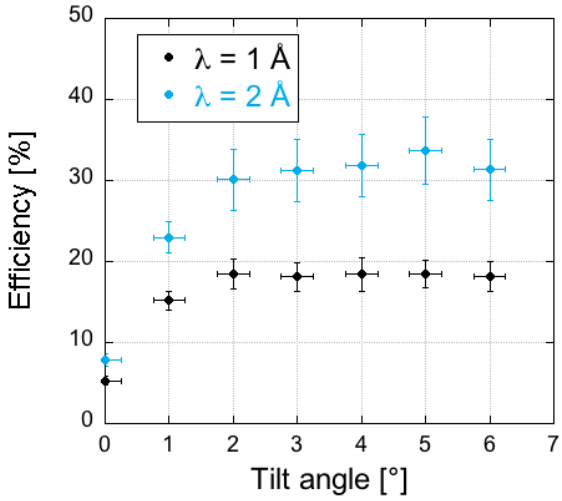

FIGURE 5.13: Measured BAND-GEM efficiency for neutrons of 1 Å (black) and 2 Å (blue) with respect to the tilt angle θ.

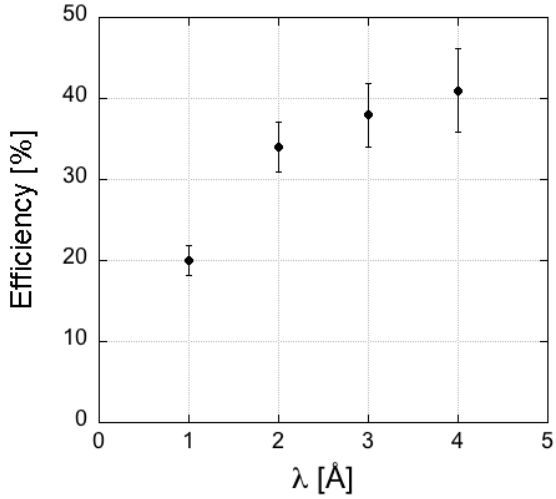

FIGURE 5.14: Measured BAND-GEM efficiency versus the neutron wavelength.

Table 5.2: Relative charge extraction efficiencies.

V_1	**Relative charge extraction efficiencies**
$V_1 = 11.1\,\mathrm{kV}$	$\eta_C = 67\%$
$V_1 = 10\,\mathrm{kV}$	$\eta_C = 65\%$
$V_1 = 9\,\mathrm{kV}$	$\eta_C = 61\%$
$V_1 = 8\,\mathrm{kV}$	$\eta_C = 55\%$
$V_1 = 6\,\mathrm{kV}$	$\eta_C = 37\%$
$V_1 = 3.3\,\mathrm{kV}$	$\eta_C = 0\%$

crossed. The spatial resolution could so be defined as the FWHM of the distribution of the joint probability P of a neutron to:

- be absorbed in either one of the two strips adjacent to a specific gap;
- release byproducts into this specific gap.

If n is the intercepted layer, such joint probability may be written as:

$$P(x) = \frac{1}{2}p_n + \frac{1}{2}p_{n+1}. \tag{5.5}$$

Using the values tabulated in Fig. 5.15 for the (discontinuous) distribution P, the centroid and FWHM can be calculated (in dependance of p) as follows:

$$\mu = \frac{\int xP(x)dx}{\int P(x)dx} \tag{5.6}$$

$$\sigma^2 = \frac{\int (x-\mu)^2 P(x)dx}{\int P(x)dx} \tag{5.7}$$

$$FWHM = 2.35\sqrt{\sigma^2}. \tag{5.8}$$

Results of such calculation are shown in Fig. 5.16 along with measured FWHM values at different angles. These were obtained illuminating the detector with a pencil beam of neutrons ($4 \times 4\,\mathrm{mm}^2$) directed so to exactly match a single pad. Since

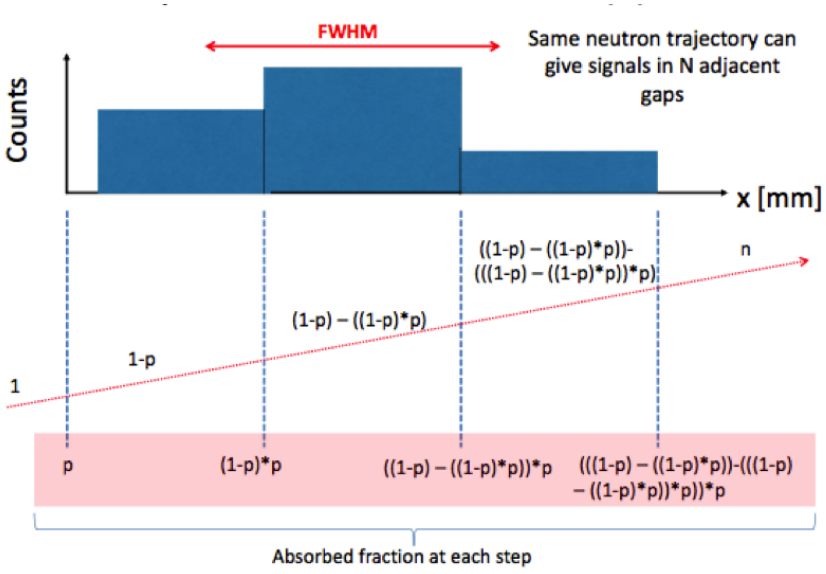

FIGURE 5.15: Definition of spatial resolution. The arrow represents the neutron trajectory that crosses N adjacent gaps. The absorbed fraction (*i.e.* the probability of the neutron capture reaction in boron) for each crossed layer and the fraction of neutrons transmitted to the next gap are shown in the red rectangle and in the gaps respectively.
The probability of a neutron to be absorbed in a *specific* boron layer is given by the product of the probability to be absorbed in a single boron layer (p) and the probability to have crossed the previous layer.

the number of events per pad can be found with the Mantid software a distribution of the collecting charge pads for each tilt angle the FWHM could be easily calculated fitting the data with a gaussian distribution. It can be seen from the Fig. 5.16 that geometrical effects on the detector have a negligible effect on the FWHM of the counts distribution, and that the resolution approaches the one defined for the ideal case.

5.4 Conclusions

In this chapter an improved BAND-GEM detector was described. The detector was tested on the EMMA instrument at ISIS and provided encouraging results: the relative charge extraction efficiency along the 3D converter was found to be $\eta_C = 67\%$,

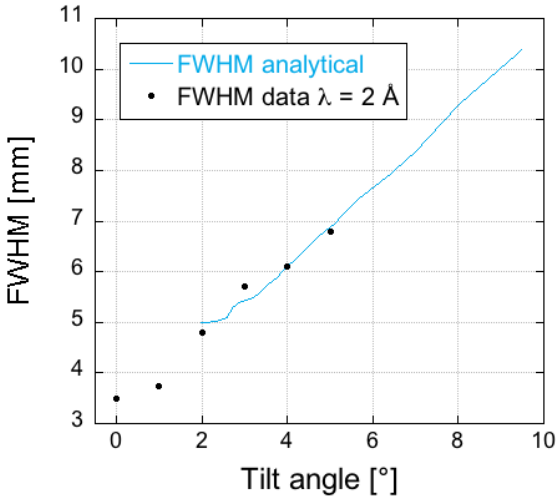

FIGURE 5.16: Measured BAND-GEM spatial resolution versus the tilt angle.

resulting in an efficiency $\epsilon \approx 40\%$ at $\lambda = 4\,\text{Å}$ for a tilt angle $\theta \approx 5°$.

6

BAND-GEM for SANS applications

A possible application of BAND-GEM detectors at ESS is the *Small Angle Neutron Scattering* (SANS) [19] [21] instrument LoKI [61] [62], one of the first instruments to be built at ESS.

This requires optimisation of the detector performance in order to meet the ESS requirements about efficiency, space and time resolution. The outcome of the development will be a "demonstrator" detector tested at neutron facilities to prove its suitability for LoKI. This goal can be achieved by carrying out different studies in parallel. On the one hand it is necessary to do an optimisation study of the geometry and the construction materials, which can be performed by simulations. On the other hand it is necessary to perform a feasibility study of the fabrication of the 3D converter and the electronics readout.

In this chapter a simulation study of the detector geometry is presented. This study represents the first attempt to develop a BAND-GEM detector technology inside the ESS simulation framework to study properties of the detector such as spatial and time resolution, detection efficiency and multiple hits between pads.
In Sec. 6.1 the SANS technique, the overview of the LoKI instrument and the detector

requirements are described. In Sec. 6.2 the simulation framework used to perform the study and the results are presented.

6.1 LoKI instrument

The LoKI instrument is designed primarily for users interested in biophysics, soft matter and materials science; they may profit of the SANS technique to study bulk properties of material like structure inhomogeneities in polymer and solutions.

6.1.1 Small Angle Neutron Scattering technique

SANS is an experimental technique that allows the investigation of materials on the micrometer to nanometer length scales. In a typical SANS experiment a well collimated neutron beam is directed on a sample, for example colloids, polymers or solution structures of proteins. Neutrons are elastically scattered by nuclear interaction with the material nuclei or by the interaction with the magnetic momentum of unpaired electrons. A detector of dimensions dx × dy, positioned at some distance, L_{sd} from the sample, and scattering angle, θ , from the sample records the flux $I(\lambda, \theta)$ of radiation scattered into a solid angle element, $\Delta\Omega = \mathrm{dx\,dy/L_{sd}^2}$ and the data can be used to extract information about shape, size, arrangement and interactions of the atoms or molecules of the sample. The flux may be expressed in the following way:

$$I(\lambda, \theta) = I_0(\lambda)\, \Delta\Omega\, \eta(\lambda)\, T\, V \frac{\delta\sigma}{\delta\Omega}(Q) \tag{6.1}$$

where I_0 is the incident flux, η is the detector efficiency, T is the sample transmission, V is the volume and the scattering vector Q is the modulus of the resultant between the incident, $\overrightarrow{k_i}$, and scattered, $\overrightarrow{k_s}$, wavevectors, (Fig. 6.1), and is given by:

$$Q = |\overrightarrow{Q}| \; = |\overrightarrow{k_s} - \overrightarrow{k_i}| \; = \frac{4\pi}{\lambda} \sin(\frac{\theta}{2}). \tag{6.2}$$

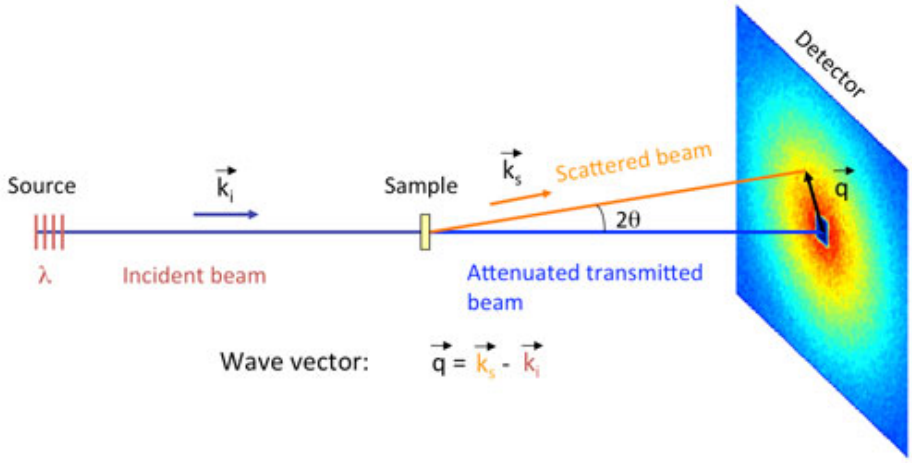

FIGURE 6.1: Scheme of a SANS experiment.

Q has dimensions [length^{-1}] and it is expressed in Å^{-1}.

The differential cross section $(\delta\sigma/\delta\Omega)(Q)$ is defined as:

$$\frac{d\sigma}{d\Omega} = \frac{\text{number of neutrons scattered per second into d}\Omega \text{ in direction } \theta \text{ , } \phi}{\Phi d\Omega} \tag{6.3}$$

where Φ is the number of incident neutrons per cm^2 per second.

The objective of a SANS experiment is to determine the differential cross-section, since this quantity contains all the information on the shape, size and interactions of the scattering centres in the sample. A typical sample may be a composite in which the part of sample of interest is coupled in an orderly way to a surrounding medium (for instance an absorbed layer on a substrate or a surface layered solute into a bulky solvent). The differential cross-section is given by:

$$\frac{\delta\sigma}{\delta\Omega}(Q) = N_p\, V_p^2\, (\Delta\delta)^2\, P(Q)\, S(Q) + B_{inc} \tag{6.4}$$

where N_p is the number concentration of scattering particles, V_p is the volume of one scattering particle, $(\Delta\delta)^2$ is the square of the difference in neutron scattering length density between the sample components, $P(Q)$ is a function known as the

form or *shape factor*, $S(Q)$ is the interparticle structure factor, Q is the modulus of the scattering vector and B_{inc} is the (isotropic) incoherent background signal. $(\delta\sigma/\delta\Omega)(Q)$ dimension is normally expressed in units of cm^{-1}.

Substituting Eq. 6.2 into Bragg's Law of Diffraction:

$$\lambda = 2d \sin \frac{\theta}{2} \tag{6.5}$$

yields a very useful expression:

$$d = \frac{2\pi}{Q} \tag{6.6}$$

where d is the characteristic length of the observed structure. Eq. 6.2 and Eq. 6.6 are central to SANS experiments because through their combined use it is possible to both configure an instrument (i.e., ensure that its "Q-range" allows you to explore the d range that you expect) and to quickly and rapidly "size" the scattering bodies in a sample from the position of any diffraction peak in Q-space.

SANS technique is applied in a wide range of scientific disciplines: biophysics, biology, chemistry, materials science and engineering. The LoKI instrument is designed primarily for the users from biophysics, soft matter and materials science. The trend in all of these fields is towards complexity and heterogeneity.

The need to build a new SANS instrument is motivated by the fact that the samples of interest in these fields of physics are more and more complex, heterogeneous (spatially and temporally) and smaller in volume [61].

Spatial heterogeneity manifests with different structure at different scales, and requires a wide Q range and small neutrons beams. Moreover these systems need to be studied with sufficient time resolution that can be provided by a high neutron flux and a wide simultaneous Q range.

LoKI is designed to satisfy these requirements by providing a high flux (at least 10 times the current leading reactor based instrument) and a broad simultaneous

Q range of at least three orders of magnitude [61]. This is achieved by positioning the sample 20 m from the moderator with 10 m of collimation and 10 m of distance between the sample and the detector system that covers a large solid angle. The main characteristics of LoKI are:

- broad simultaneous Q range: $1\text{x}10^{-3}\,\text{Å}^{-1} < \text{Q} < 1\,\text{Å}^{-1}$
- high neutron flux ($10^9\text{n/cm}^2\text{/s}$ on sample) exploiting the high source brightness at the ESS.
- the instrument should be capable of providing a Q resolution $(dQ/Q) < 10\%$ over the whole Q range.

6.1.2 Instrument overview and detectors

A layout of the LoKI instrument and its different components are shown in Fig. 6.2.

For a detailed description of the instrument please refer to [62]. In this thesis the focus is on the detector system inside the detector tank. The overall length of LoKI, from the moderator to the back of the detector tank, will be up to 40 m including shielding.

LoKI provides two modes of operation offering different wavelength bands and hence different Q ranges. The wavelength selection is made by two choppers, each of which is composed by two rotating disk of a neutron absorbing material and with slits that, when in correspondence of the beam deliver at a sample a pulse of neutrons with a specific range in λ. The two modes of operation for LoKI are:

- Mode 1: a chopper runs at the source frequency (14 Hz) providing the wavelength band from 3 Å to 10.5 Å (1.8 Å to 11.6 Å) whilst avoiding frame overlap.
- Mode 2: the chopper runs at half the source frequency (7 Hz) providing for measurement across two source frames and doubles the bandwidth compared to Mode 1 (from 3 Å to 19.9 Å, 1.8 Å to 21.0 Å with penumbra).

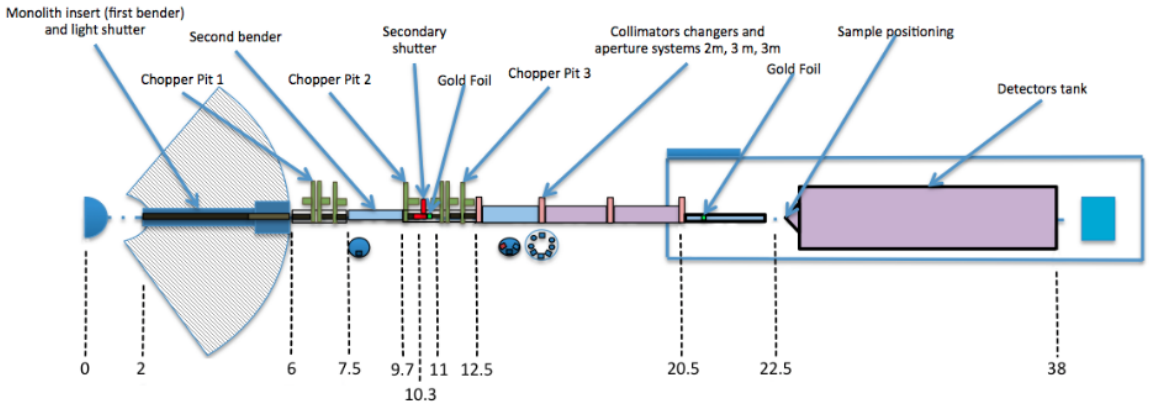

FIGURE 6.2: Layout of the LoKI instrument. The first component is a 4 m long bender positioned at 2 m from the source, used to avoid line-of-sight to the moderator and the consequent γ-ray background. A double-disk chopper located 6.5 m from the source perform the wavelength selection and the first resolution enhancement chopper is at 7 m. A second 2.1 m long bender is positioned between the first and second chopper pits. A second resolution enhancement chopper is at 10 m from the source. Then there is a guide to the third chopper pit where there is chopper pair at 11.5 m and the final resolution enhancement chopper at 12 m. Four aperture wheels respectively at 12.5 m, 14.5 m, 17.5 m and 20.5 m are spaced out by three guide changer drums. Then there is a 2m of evacuated flight path. After the sample the detector system is mounted.

A possible configuration for the LoKI detector system is the so called "window frame" arrangement as shown in Fig. 6.3, composed of a series of three octagonal detector panels with holes in centre and placed within a large vacuum vessel. With this configuration a large solid angle is covered. The outer radia of the octagons are 130 cm, 100 cm and 50 cm for the front, middle and rear detector respectively. The first two panels are fixed, whilst the rear detector is movable towards the beam axis to match the 5 m collimation setting if the lowest Q-values are not required.

6.2 Simulation of detector performance

A study of the rear detector performance achievable with the BAND-GEM technique is described in the next section. The study presented in this chapter is the first part

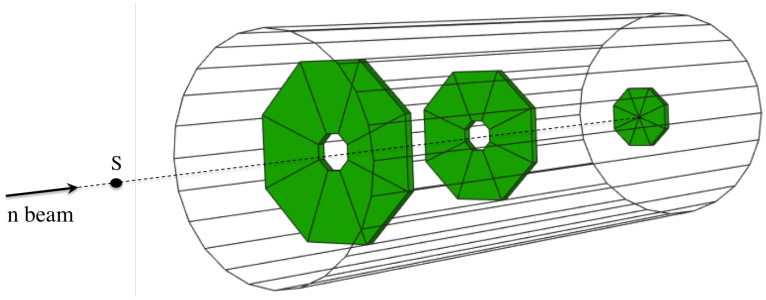

FIGURE 6.3: Window frame geometry of LoKI. The neutron beam is directed as the dashed line and the black point is represents the sample.

of a more complete study that will be developed in the future years and in support of the construction of the LoKI rear detector.

6.2.1 The dgcode simulation framework

The ESS detector group developed a coding framework named *dgcode* [63] that simplifies the collaboration between multiple developers working on one or more tasks using different platforms such as Linux servers and either Linux or OSX laptops [64]. The dgcode coding framework is a sort of collection of files written in different languages such as C++, C, python, Fortran or BASH that are organised in a directory structure that creates units of software or packages. Packages are connected between them in a hierarchical structure so that many developers can work on software avoiding duplication of work. The entire code is hosted inside a Mercurial repository at bitbucket.org that contains history information about the changes in all the files allowing more than one person to work on a project at the same time.

6.2.2 Advantages and limits of the MC simulations

A simulation study of the rear detector based on the BAND-GEM technology for the LoKI instrument has been made inside the *dgcode* framework using a software based on the Monte Carlo simulation toolkit Geant4 [65]. Any detector element is described by:

- a geometrical volume that contains the information regarding the shape of detector element, its dimensions and its position with respect to the other elements;

- a physical volume including all the information regarding the material of which the detector is made of, its temperature and pressure.

All the elements defined in the physical volume are associated to the cross section data available for all possible physical processes. Once the detector is completely defined the input particles are launched with an initial energy and direction. The particles propagate and if they enter the geometrical volume of the detector, the Monte Carlo routine of the code can either select a physical process or not, depending on its probability. All the particle information are recorded in a file from which the user can extract the parameters of interest (for instance position and energy when absorbed).

One of the advantages of the Monte Carlo simulation is the fact that it is possible to access the four contributions to the rear detector efficiency defined here:

- *the crossing efficiency* ϵ_{cross} defined as the number of neutrons that cross a boron layer divided by the number of neutrons incident on the detector surface;

- the *conversion efficiency* ϵ_{conv} defined as the number of neutrons that are captured by the $^{10}\mathrm{B}(\mathrm{n};\alpha)^{7}\mathrm{Li}$ reaction divided by the number of neutrons crossing the boron layer;

- the *escape efficiency* ϵ_{esc} defined as the number of capture events that generate an $\alpha/^{7}\mathrm{Li}$ able to reach the gas between lamellas divided by the number of captured neutrons;

- the *collecting efficiency* ϵ_{coll} defined as the number of events that deposit in

Table 6.1: Requirements of the rear detector of the LoKI instrument.

Requirements	**Values**
Q range	$1 \times 10^{-3}\,\text{Å}^{-1} < \text{Q} < 1\,\text{Å}^{-1}$
λ of detected neutrons	$2 - 22\,\text{Å}$
θ resolution	$\Delta\theta/\theta < 10\%$
Φ resolution	$\Delta\phi/\phi < 10\%$
Neutron efficiency	$\epsilon > 30\%$ at $1.8\,\text{Å}$

the gas a total energy higher than a certain threshold divided by the number of "escaped" events.

The total detection efficiency $\epsilon_{detection}$ defined as the number of events that deposit in the gas a total energy higher than a certain threshold divided by the number of neutrons incident on the detector surface can be approximately expressed as:

$$\epsilon_{detection} = \epsilon_{cross} \times \epsilon_{conv} \times \epsilon_{esc} \times \epsilon_{coll} = \frac{\text{no. of collected events}}{\text{no. of incident neutrons}} \tag{6.7}$$

With these assumption it is possible to decompose the detection efficiency and maximise each component to reach the highest efficiency: this is especially important for a detector with such a complicated geometry.

6.2.3 Detector design in Geant4

The requirements of the rear detector of the LoKI instrument are reported in Table 6.1. As shown in Fig. 6.3 the rear detector has an octagonal shape, a design choice reflecting the circular symmetry of some scattering patterns. The octagon allows to divide the rear detector in eight identical trapezoidal sections where the dead space is represented by the frames.

The study presented in this thesis has been done for a single octant *i.e.* a single trapezoidal frame.

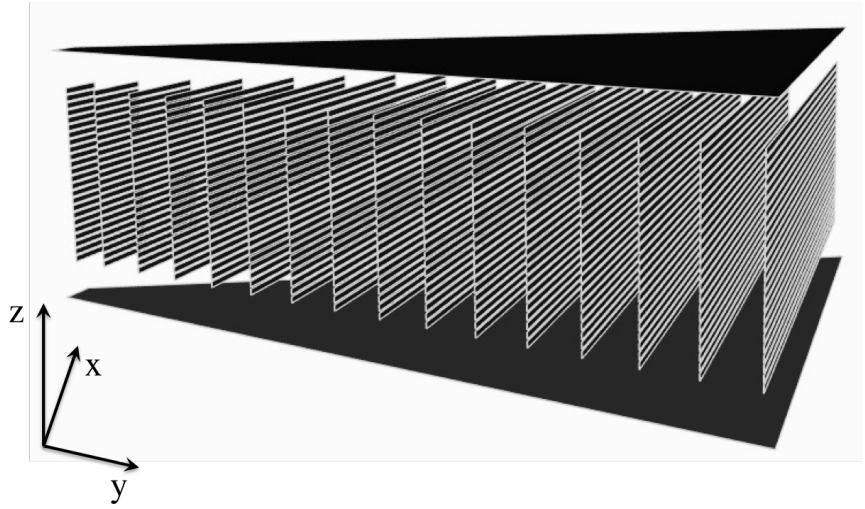

FIGURE 6.4: Exploded view drawing of the BAND-GEM in Geant4: cathode, 3D converter and anode starting from the bottom. Only a lamella out of five is shown for the sake of clarity. Neutrons come from the bottom.

The Geant4 model of the BAND-GEM detector is shown in Fig. 6.4 (exploded view). It has a trapezoidal shape with height 40 cm, short base 2.5 cm and long base 35.7 cm. It is composed by a 250 μm Al cathode. The 3D converter is made of ninety-nine lamellas stacked perpendicularly with respect to the cathode and a gap of 4 mm between two adjacent lamellas. Each lamella is made of a thick Al 200 μm grid with twenty-four 3 mm long strips alternated with 1 mm of empty space. A 1 μm thick coating of $^{10}B_4C$ is deposited on both sides of the Al lamella. A scheme of the detector components is shown in Fig. 6.5. The aluminium anode has a 100 μm depth and trapezoidal readout pads. The height of each pad is 4 mm (*i.e.* the gap between two adjacent lamellas) and there are 10 pads for each row. The GEM foils are not included in the module. All the components are inserted in a box filled with Ar/CO_2 (70%/30%) at STP.

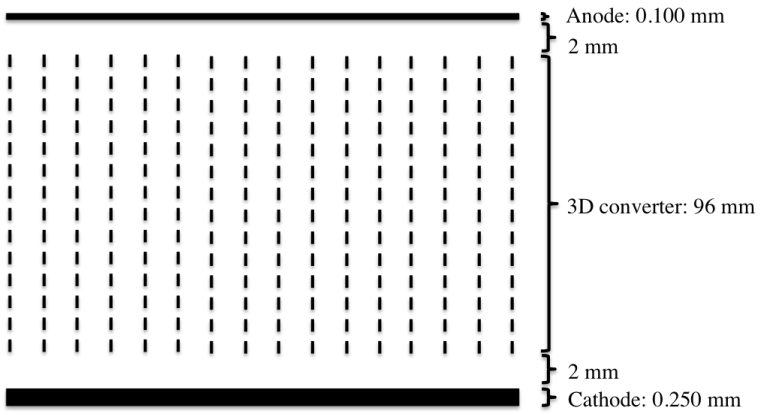

FIGURE 6.5: Scheme of the BAND-GEM detector components in the LoKI rear detector model.

6.2.4 Timing resolution

LoKI is a *Time-of-flight* instrument *i.e.* it is based on the measurement of the time that a neutron spends from the start t_0 to the instant in which the signal is detected in the readout electronics. Two neutrons of the same kinetic energy, and same t_0, could in principle be absorbed at different depths inside the 3D converter, thus giving signals at slightly different times. Therefore it is necessary to study the impact of the depth of the BAND-GEM on the ToF. Analytical calculations could be done knowing the wavelength spectrum of the neutrons and the geometry of the detector, but they do not take into account the scattering effect of the lamella material (*i.e.* aluminum) on the ToF. For this reason a Monte Carlo simulation, taking into account the scattering effect of the BAND-GEM materials, was done to compare the two results. Using Geant4 simulations it was possible to study the ToF broadening of a monochromatic and point-like neutron beam that hits the BAND-GEM detector model described in Sec 6.2.3. The ΔToF in this case could be defined as the time spent by a single neutron inside the BAND-GEM detector from the lowermost edge to the capture in $^{10}B_4C$. The simulation shows that a starting deltoid in ToF (the

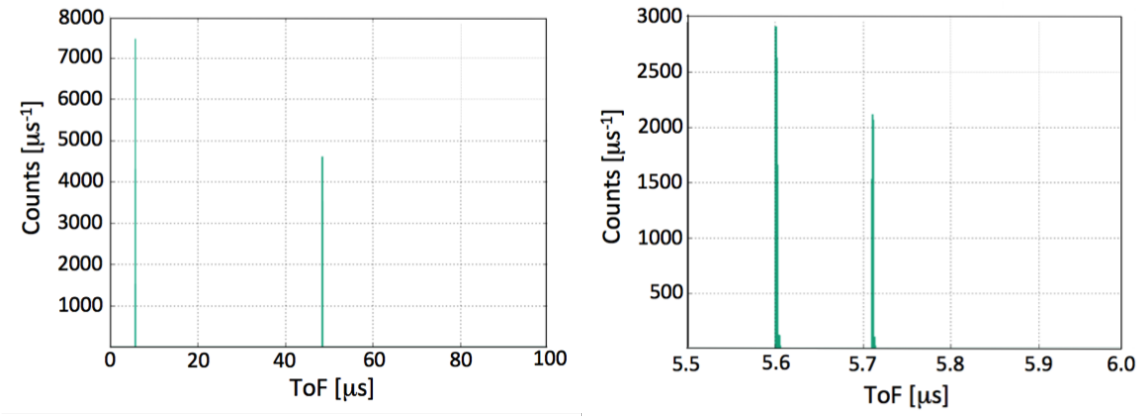

FIGURE 6.6: (a) Distribution of the time spent by a monochromatic ($\lambda = 2.2\,\text{Å}$) and point-like neutron beam inside the BAND-GEM detector from the lowermost edge to the capture in $^{10}B_4C$. Since the beam is directed in such a way that it crosses two different lamellas, two peaks are visible. The bin width is $1\,\mu$s.
(b) Zoom of the peak at $\approx 5\,\mu$s: the bin width is 1 ns. Since each aluminium lamella is coated on both sides with $^{10}B_4C$, two peaks are visible. The FWHM is ≈ 2 ns.

neutrons are launched at the same t_0) is split into four peak-shaped capture time distributions: two layers of $^{10}B_4C$ for two interaction points in the lamellas system as shown in Fig. 6.6. In Fig. 6.6(a) two peaks, corresponding to two different crossed lamellas, are visible: the bin width is $1\,\mu$s. In Fig. 6.6(b) the zoom of the peak at $\approx 5\,\mu$s is shown. The two peaks shown are due to the fact that two boron layer are crossed in a single lamella: the bin width is 1 ns.

If the neutron beam simulated is white inside the LoKI range of wavelengths ($2 - 12\,\text{Å}$) and isotropic on the detector, the obtained ΔToF distribution is shown in the plot in Fig. 6.7 (the bin width is $1\,\mu$s). The plot shows that the maximum broadening in ToF due to the BAND-GEM depth is $\Delta\text{ToF}_{\text{sim}} \approx 300\,\mu$s. From an analytical point of view the worst case in terms of ΔToF is represented by neutrons of $\lambda = 12\,\text{Å}$ that are captured by the ^{10}B immediately before the outermost detector edge. In fact an indetermination of the flight path affects more the long wavelengths (slower neutrons) than the short ones. For the setup represented in Fig. 6.8 the ΔToF

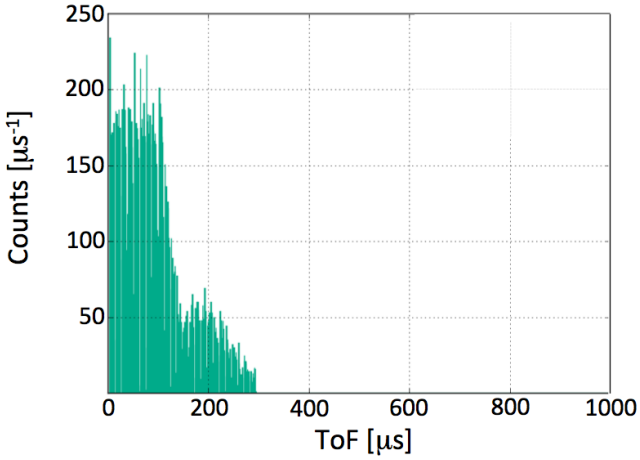

FIGURE 6.7: Distribution of the time spent by a white ($2 - 12$ Å) and isotropic neutron beam inside the BAND-GEM detector from the lowermost edge to the capture in $^{10}B_4C$. The bin width is 1 μs.

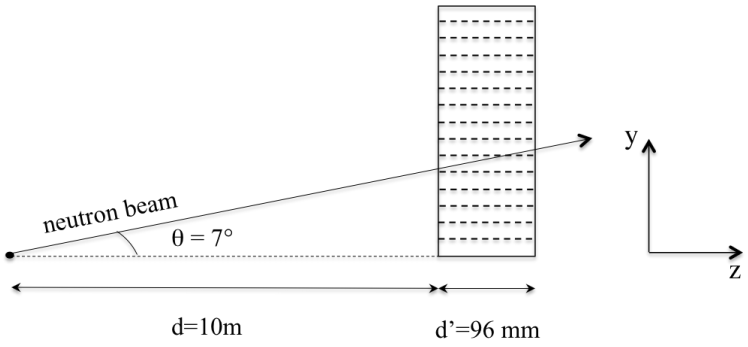

FIGURE 6.8: Setup used for the analytical calculation of the ΔToF and for the simulation with the monochromatic and point-like beam.

is $\Delta\text{ToF}_{\text{ana}} = 300\,\mu$s. The comparison of the two results shows that the scattering effect on the aluminium lamellas is negligible and that the ToF broadening is only due to the 3D converter geometry.

6.2.5 Energy deposition volume

The anode pad dimensions should be optimised to comply with the ESS requirements about the spatial resolution. Among others, the energy deposition of charged

byproducts into the gas is the dominant effect. In fact, the mean free path of α and ^{7}Li in the gas is several millimetres; thus, even if the neutron absorption reaction is point-like, the energy deposition in the gas (that originates the electron cascade that is eventually detected by the anode) is not. A study of the energy deposition volume of the charged byproducts of the capture reaction in the gas was done by Geant4 simulations [64]. Indeed a monochromatic and "point-like" beam, after capture in ^{10}B generates a cloud of α particles and ^{7}Li with a certain volume distribution given by the charged particles range. The energy deposition volume has a three dimensional structure and the FWHM of the projections on the xy an zy planes give information about the broadening of the charge cloud in space.

The energy deposition volume has been studied for neutron trajectories crossing one or two lamellas. A scatter plot of the energy deposition points inside the gas is shown in Fig. 6.9 for the xy, zx and zy projections in panels (a), (b) and (c) respectively, in the case of a single lamella hit. Among them the most interesting is the xy projection, lying parallel to the anode plane. This scatter plot shows how a point-like interaction is broadened by the physical process of the capture reaction only. The FWHM of this projection represents a lower limit to the spatial resolution of the detector. An immediate consequence is that the readout pad size need not to be much smaller than such FWHM. The x and y projections are shown in Fig. 6.10 and the FWHMs are $\mathrm{FWHM_x^{1hit}} = 3\,\mathrm{mm}$ and $\mathrm{FWHM_y^{1hit}} = 3.3\,\mathrm{mm}$.

The same study has been made for the worst case of a neutron beam crossing two different lamellas (Fig. 6.11). In this case the resulting FWHM are $\mathrm{FWHM_x^{2hits}} = 3\,\mathrm{mm}$ and the $\mathrm{FWHM_y^{2hits}} = 6\,\mathrm{mm}$. These results compare well with the FWHMs measurements obtained with the BAND-GEM tests (see Sec. 5.3.3).

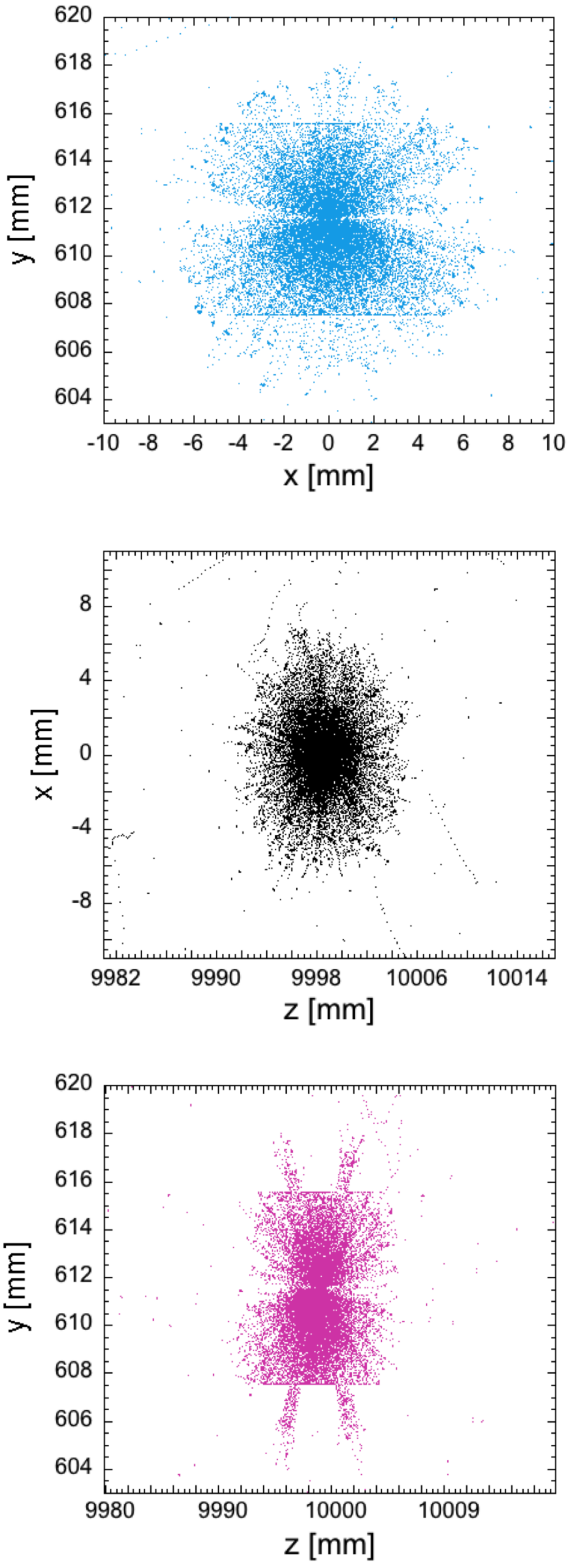

FIGURE 6.9: Energy deposition volume projections of a cloud of α particles and ^{7}Li generated by a monochromatic and "point-like" neutron beam that crosses a single lamella in his trajectory.

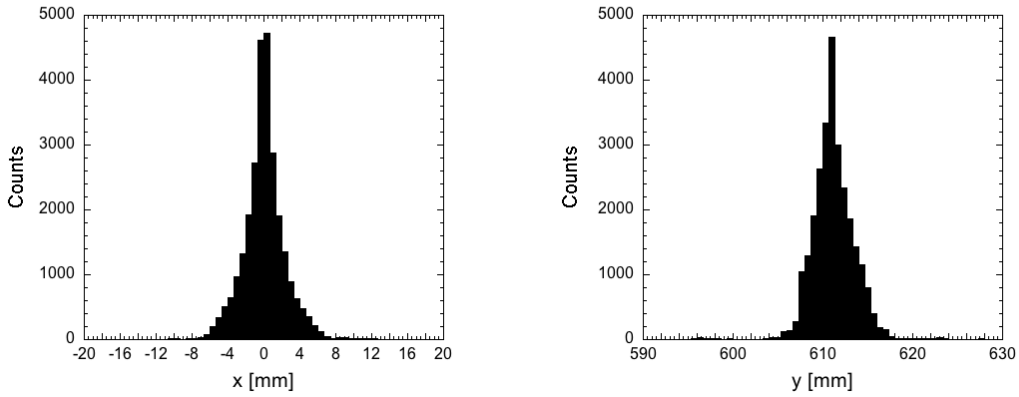

FIGURE 6.10: Projections of the energy deposition volume of α and ^{7}Li cloud generated by a monochromatic and point like neutron beam that crosses a single lamella in his trajectory.

6.2.6 Multiple hits

In an ideal detector the neutron capture reaction in boron at position (x, y, z) generates the triggering of a single readout pad allowing one to determine the (x, y) coordinates of the interaction with a precision equal to the pad dimensions. As shown in Sec. 6.2.5 the energy deposition of α and ^{7}Li has a certain volume distribution and thus it is possible that an over-threshold signal is detected in more than one pad. Furthermore the scattering of neutrons in the detector structure may cause the triggering of a different pad from the one expected. These phenomena (see Sec. 5.3.3) are best investigated with Monte Carlo simulations. Such simulations were performed inside the *dgcode* framework with the aim of estimating the multiple hits, here defined as the fraction of events in which more than one pad is triggered by a single neutron capture event. The simulation was performed by dividing the cathode area in trapezoidal sections so that each anode pad i corresponds to the projection $\tilde{i}$ on the cathode; multiple hits out i occur when a neutron crosses the pad projection $\tilde{i}$ on the cathode and generates an over-threshold signal (THR $\sim 100\,\mathrm{keV}$)

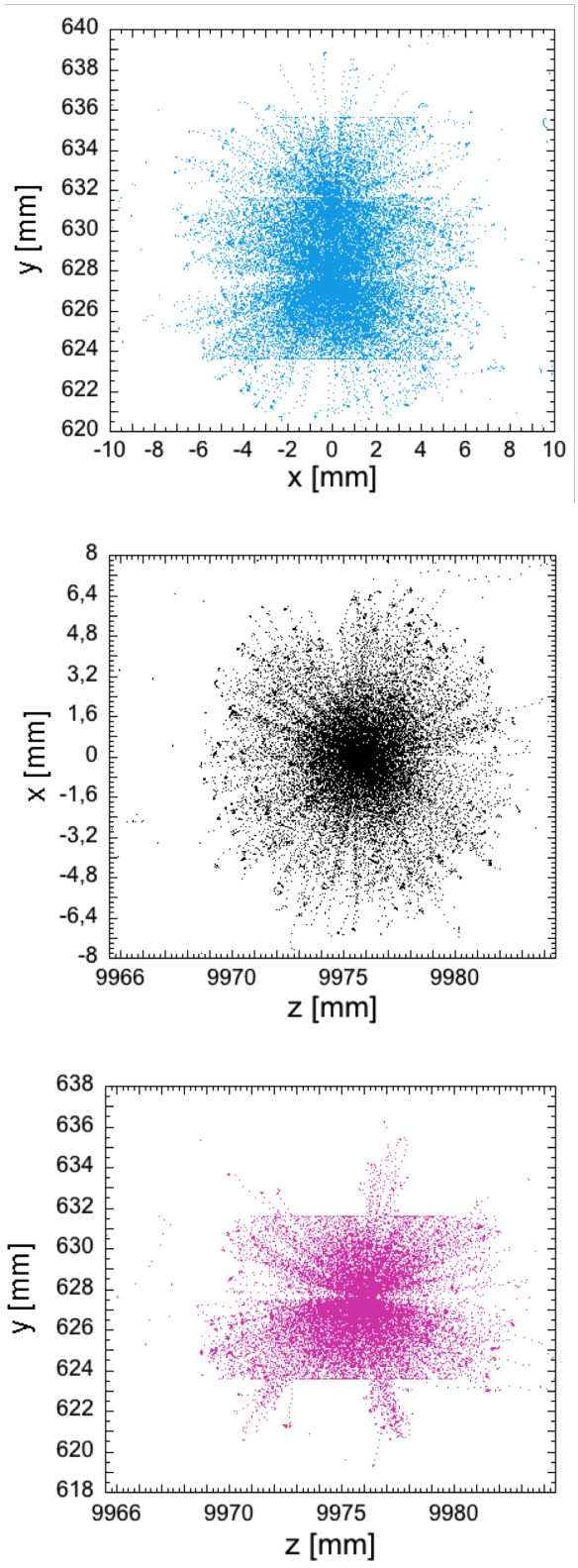

FIGURE 6.11: Energy deposition volume projections of a cloud of α particles and ^{7}Li generated by a monochromatic and point like neutron beam that crosses two lamellas in his trajectory.

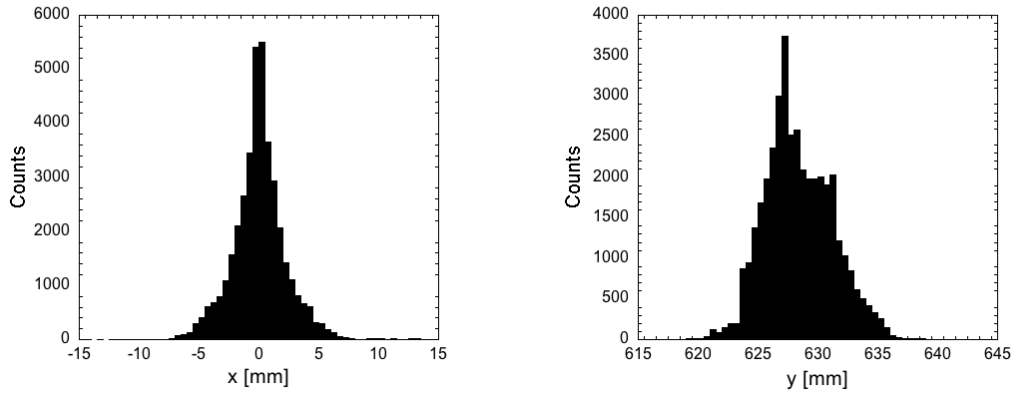

FIGURE 6.12: Projections of the energy deposition volume of α and ^{7}Li cloud generated by a monochromatic and point like neutron beam that crosses two lamellas in his trajectory.

in more than a single pad on the anode.

The fraction of neutrons that generate an over-threshold signal in n pads is shown in Fig. 6.13 for pads lying on the bottom (inner relative to the radius) (a), in the middle (b) and on top (outer relative to the radius) (c) of the detector. The incidence angle of the beam is $\theta_{min} = 2.57^\circ$, $\theta_{middle} = 3.72^\circ$ and $\theta_{max} = 4.85^\circ$ for (a), (b) and (c) respectively, θ_{min} and θ_{max} being the minimum and maximum incidence angles compatible with the LoKI detector geometry.

It can be noticed that the worst case is (a) where the highest multiple hits level is reached and it is about 6% of the total number of events and about 16% of the number of neutrons that generates a signal over-threshold in at least one pad. This percentage decreases for higher incidence angles and pad dimensions. For instance in (c) the cross-talk level is 1% of the total number of events and about 3% of the detectable events. This effect is expected because pads of bigger dimensions match better than the smaller pads the xy projection of the energy deposition volume of the α and ^{7}Li cloud.

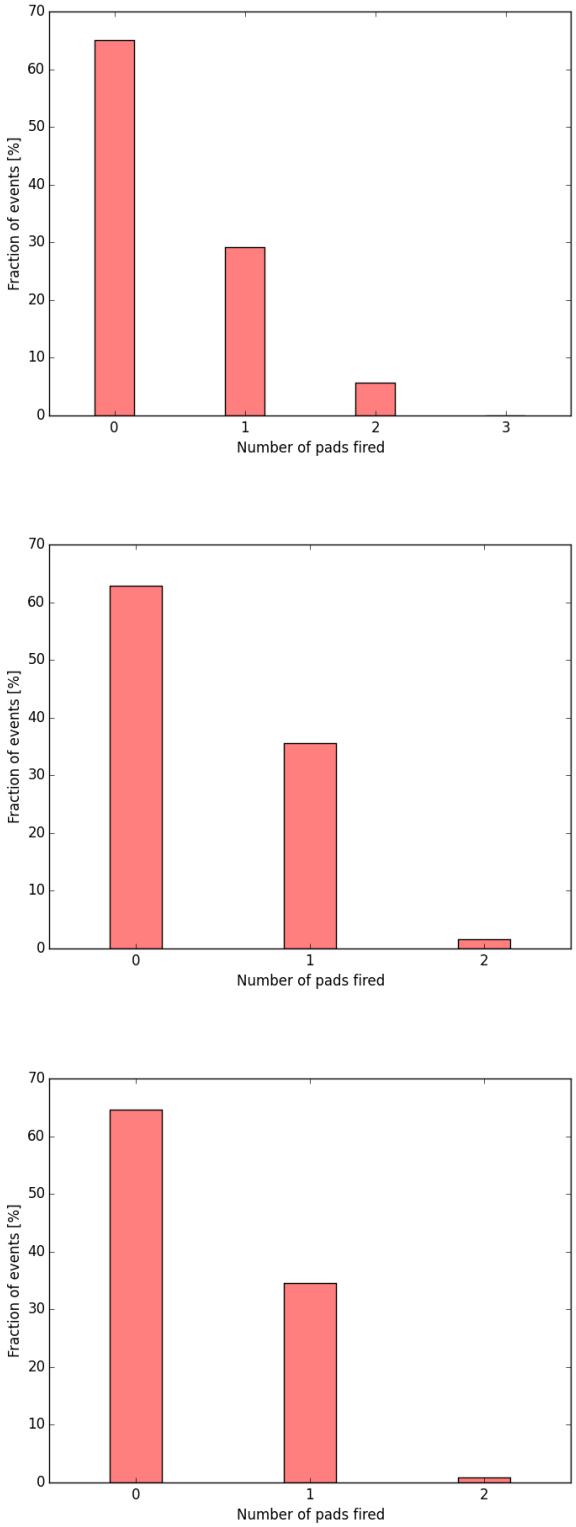

FIGURE 6.13: Fraction of neutrons that generate a signal over-threshold in n pads for a neutron beam hitting the bottom (a), the middle (b) the top (c) of the detector.

Table 6.2: Values of ϵ_{det} and its contributing factors ϵ_{cross}, ϵ_{conv}, ϵ_{esc} and ϵ_{coll} for different lamellas materials and thicknesses. The simulated beam is monochromatic (λ = 4Å) and point like and hits the detector with an angle of $\theta = 2.57°$. The threshold used for the ϵ_{coll} is equal to THR = 100 keV.

Material	**Thickness** [μm]	λ [Å]	ϵ_{cross}	ϵ_{conv}	ϵ_{esc}	ϵ_{coll}	ϵ_{det}
Ti	100	4	97%	93%	74%	90%	60%
Ti	200	4	87%	96%	72%	94%	56%
Al	400	4	100%	93%	71%	90%	60%
Al	20	4	93%	96%	78%	95%	66%

However a most important result is that, in the limit of the used statistics (100,000 starting neutrons per run), no neutron capture events are observed firing up more than two pads. This is an easily manageable level with standard software rejection techniques. Moreover, this level may be further reduced with a fine tuning of the threshold.

A more complete study of the multiple hits over the full detector will be performed once the LoKI detector design is finalised.

6.2.7 Efficiency

Of the four parameters shown in Eq. 6.7, three of them (ϵ_{cross}, ϵ_{conv} and ϵ_{esc}) depend on the detector geometry and materials and the angle with which the neutron beam hits the detector. ϵ_{conv} also depends on the neutron wavelength.

The study and separate optimisation of such factors may be easily performed via Monte Carlo simulations by changing parameters like lamellas thickness, materials, *etc.* Moreover simulations can explore the effects of such parameters in different parts of the full scale LoKI BAND-GEM once its design is finalised. Here some results are reported from simulations performed with different lamella thicknesses and materials (see Table 6.2). The simulations are done using a monochromatic ($\lambda = 4$ Å) and "point-like" beam that hits the detector with a tilt angle of $\theta = 2.57°$.

This is the minimum θ compatible with the LoKI detector geometry, corresponding to the minimum amount of boron crossed by the neutron beam. The values reported in Table 6.2 represent thus an estimate of the lower limit of the efficiency components in the whole detector.

6.3 Conclusions

On the basis of the performance results obtained with the BAND-GEM technology shown in Chapters 4 and 5, a collaboration with ESS was established during the PhD with the aim to develop a thermal neutron detector with a boron-based 3D converter, as part of the detector system of LoKI, a SANS instrument and one of the first to be installed on ESS. Simulations were performed within the Geant4-based ESS simulation framework (*dgcode*) to study the performance of the detector such as spatial and time resolution, detection efficiency and to study undesired effects like multiple hits of readout pads.

7

Conclusions

Neutron science is faced with the challenge of finding alternative technologies to ^{3}He as a thermal neutron detector with a rate capability matching the high fluxes expected at the European Spallation Source (ESS).

Aim of this PhD thesis was the development of a ^{3}He-free high-rate thermal neutron gaseous detector based on the Gas Electron Multiplier (GEM) technology for applications at spallation sources.

The starting point of this thesis was a small area ($100\,\mathrm{cm}^2$) GEM-based detector (bGEM) for thermal neutrons with a converter cathode made of aluminium coated by $1\,\mu$m of B_4C and with a padded readout structure (Chapter 3). The nuclear capture reaction $^{10}\mathrm{B}(\mathrm{n};\alpha)^7\mathrm{Li}$ provides the "conversion" of thermal neutrons into charged particles that ionise the detector gas. Previous measurements at the VESUVIO neutron beam line at ISIS had shown that this detector is fully able to detect thermal neutrons, but due to its low efficiency ($\approx 1\%$) it can only be used as a beam monitor.

A rate measurement on the bGEM was performed at the ORPHEE reactor and the maximum rate capability was found to be $50\,\mathrm{MHz/cm}^2$ with no sign of saturation, which is way beyond the rate capability of ^{3}He tubes.

The detector showed also the capability to correctly reconstruct the diffractogram of a copper sample in a diffraction experiment performed on the INES instrument at ISIS. The total count rate of the bGEM active area resulted to be about 7% the count rate of reference ^{3}He detectors, the S/B ratio for the bGEM was two times lower than the ^{3}He tube one and the bGEM FWHM was 1.75 times the ^{3}He tube one. With a cathode coated with 1 μm of $^{10}B_4C$ instead of natural B_4C the count rate became about 19% of the ^{3}He tube, the bGEM FWHM was comparable to the ^{3}He tube FWHM if focussing is applied and the S/B ratio was still two times lower than the ^{3}He tube.

The detector efficiency depends on the probability of neutron capture in the B_4C coating and the escape of α and ^{7}Li byproducts from it. A way to enhance the efficiency is to increase the effective layer of ^{10}B crossed by the neutron trajectory while keeping the coating thin enough to allow the byproducts to reach the gas and ionise it.

The *Borated Array Neutron Detector*-GEM (BAND-GEM) described in Chapter 4 is a practical application of the mentioned approach: the boron layers are distributed in a number of lamellas composing a so called 3D converter, and a proper regulation of the field inside the 3D converter ensures a proper charge collection.

A feature of the 3D converter is that, if the whole detector is tilted by an angle θ with respect to the sample-detector direction, the thickness of $^{10}B_4C$ crossed by the neutrons is increased by a factor $1/sin(\theta)$ and the neutron "conversion" probability is enhanced. The BAND-GEM detector was tested at the JEEP-II reactor in Norway to confirm this behaviour and the maximum count rate was found for $\theta = 7°$. The BAND-GEM was also used to perform a diffraction experiment at the INES beam line at ISIS. The BAND-GEM count rate per unit area was measured to be $\approx 25\%$ relative to the reference ^{3}He tubes and its time resolution is comparable with that of ^{3}He as the S/B ratio. These results demonstrate that the BAND-GEM is able to

reproduce diffractograms with a comparable quality to ^{3}He.

The BAND-GEM efficiency may be significantly improved by optimising the geometry of the converter (for instance the distance between lamellas) thus providing a better charge extraction in the conversion region. This optimisation resulted in the final BAND-GEM prototype described in Chapter 5.

The detector was tested for the first time on the EMMA instrument at ISIS. A measurement of the relative charge extraction efficiency across the 3D converter gave values up to $\eta_C = 67\%$. The efficiency is $\epsilon \approx 40\%$ at $\lambda = 4\,\text{Å}$ for a tilt angle $\theta \approx 5^\circ$.

These and other features obtained with this new technology, make it an attractive candidate for installation - after further optimisation - on LoKI, a *Small Angle Neutron Scattering* (SANS) instrument and one of the first ones to be installed at the ESS. Thus, preliminary simulations were accomplished, inside the Geant4-based ESS simulation framework (*dgcode*), to study the performance of the detector such as spatial and time resolution, detection efficiency and to study undesired effects such as multiple hits among the readout pads. The simulations show that the maximum time broadening due to the 3D converter finite extension (about 10 cm) is $\Delta\text{ToF}_{\text{max}} = 300\,\mu\text{s}$. This result is coherent with an analytical calculation that evaluates the ΔToF in the worst case of a $\lambda = 12\,\text{Å}$ neutron (the slowest neutrons in the LoKI spectrum) that is captured at the end of the 3D converter, near the GEMs. This means that the scattering effect (not considered in the analytical calculation) is negligible and that the ToF broadening is close to the ideal case.

The energy deposition volume of α and ^{7}Li particles produced by the capture reaction (simulated within the *dgcode*), when projected on the anode plane, results in distributions with $\text{FWHM}_{\text{x}}^{\text{1hit}} = 3\,\text{mm}$, $\text{FWHM}_{\text{y}}^{\text{1hit}} = 3.3\,\text{mm}$ and $\text{FWHM}_{\text{x}}^{\text{2hits}} = 3\,\text{mm}$, $\text{FWHM}_{\text{y}}^{\text{2hits}} = 6\,\text{mm}$ for a neutron trajectory hitting one and two lamellas, respectively. This result provides guidance regarding the choice of readout pad dimensions. Multiple hits, defined as the fraction of events triggering more than one pad,

was found to be at most 16% of the neutrons generating an over-threshold signal (THR $\approx 100\,\mathrm{keV}$) in at least one pad. This effect can easily be dealt with.

The results of this thesis demonstrate that the BAND-GEM is an attractive technology alternative to ^{3}He: it provides very high count rates and has the potential to cover large areas ($\approx 1\,\mathrm{m}^2$). The efficiency level reached (40% at $\lambda = 4\,\text{Å}$) is adequate for real applications including the LoKI instrument at ESS.

List of Tables

3.1 GEM technology specifications 27

3.2 bGEM specifications 29

4.1 $^{10}B_4C$ coating characterisation 49

5.1 EMMA experimental setups. 70

5.2 Relative charge extraction efficiencies. 78

6.1 Rear detector requirements 89

6.2 Efficiency for different materials and thicknesses. 100

List of Figures

1.1 Bragg diffraction. 5

1.2 ESS pulse. 6

1.3 ^{3}He supply 8

2.1 Cross section versus neutron energy for some reactions of interest in neutron detection. 14

2.2 Gas detectors operating regions. 16

2.3 Cross section of a Geiger counter and description of the mechanism by which additional avalanches are triggered in a Geiger discharge. . . 18

2.4 Differential pulse height spectra from a ^{3}He tube. 19

2.5 Counting curve plateau for a gas-filled ^{3}He detector. 21

3.1 Microscopic view of a Gas Electron Multiplier foil. 24

3.2 Drift and equipotential lines of a GEM detector. 24

3.3 Sketch of a single GEM detector. 25

3.4 bGEM scheme 28

3.5 α and ^{7}Li range in B_4C *vs* ion energy 30

3.6 Sphere model 31

3.7 α and ^{7}Li escape probability 31

3.8 CARIOCA chip 32

3.9 FPGA mother board 32

3.10 bGEMs setup on INES 35

3.11 bGEM-1 diffractogram 36
3.12 bGEM-2 diffractogram 37
3.13 Debye-Scherrer cones 39
3.14 *Focussing* results 40
4.1 BAND-GEM operation scheme 47
4.2 Photo of Al_2O_3 lamella 47
4.3 3D converter working principle 48
4.4 ROTAX measured neutron beam spectrum 52
4.5 CCD acquisition images 53
4.6 Neutrography plot profiles 54
4.7 JEEP-II reactor hall 55
4.8 BAND-GEM experimental setup scheme at the RD2D 56
4.9 BAND-GEM experimental setup view at the RD2D 56
4.10 BAND-GEM HV scan at R2D2 57
4.11 BAND-GEM counting rate of a γ-ray source 58
4.12 BAND-GEM counting rate at R2D2 59
4.13 Experimental setup of a diffraction measurement with the BAND-GEM 60
4.14 BAND-GEM diffractogram 61
4.15 ^3He diffractogram 62
5.1 Scheme of the new BAND-GEM prototype. 66
5.2 Aluminium grid used for the new BAND-GEM prototype. 67
5.3 Padded anode used for the new BAND-GEM prototype. 67
5.4 View of the 3D converter in the BAND-GEM with electrical contacts. 68
5.5 Experimental setup on EMMA. 69
5.6 Definition of x,y and z axis used in the EMMA experiment. 70

5.7 BAND-GEM setup on EMMA for $\theta = 0^\circ$ and $\theta = 90^\circ$. 71

5.8 Time of flight spectrum on EMMA 72

5.9 Scan of the voltage along the 3D converter. 73

5.10 Scan of the voltage between the GEMs and the 3D converter. 74

5.11 Scan of the voltage along the GEMs. 75

5.12 Relative charge extraction efficiency measurements. 76

5.13 BAND-GEM efficiency versus tilt angle 77

5.14 BAND-GEM efficiency versus λ 77

5.15 Definition of spatial resolution. 79

5.16 BAND-GEM spatial resolution versus the tilt angle. 80

6.1 Scheme of a SANS experiment. 83

6.2 Layout of the LoKI instrument 86

6.3 Window frame geometry of LoKI 87

6.4 Exploded view drawing of the BAND-GEM in Geant4 90

6.5 Scheme of the BAND-GEM detector components in the LoKI rear detector model. 91

6.6 ToF simulation of a monochromatic and point like beam. 92

6.7 ToF simulation of an isotropic neutron beam. 93

6.8 Model for the ΔToF calculation. 93

6.9 Energy deposition volume (1 hit). 95

6.10 Projections of the energy deposition volume of α and ^{7}Li cloud (1 hit). 96

6.11 Energy deposition volume (2 hits). 97

6.12 Projections of the energy deposition volume of α and ^{7}Li cloud (2 hits). 98

6.13 Fraction of neutrons that generate a signal over-threshold in n pads. . 99

Bibliography

[1] Dana A Shea and Daniel Morgan. The helium-3 shortage: supply, demand, and options for Congress. Congressional Research Service, Library of Congress, 2010.

[2] Richard T Kouzes. The ^{3}He supply problem. Technical report, Pacific Northwest National Laboratory (PNNL), Richland, WA (US), 2009.

[3] ESS Home Page: https://europeanspallationsource.se.

[4] S Peggs, K Andersen, D Argyriou, K Batkov, C B'ohme, S Bousson, I Bustinduy, C Carlile, P Carlsson, L Celona, et al. ESS Conceptual Design Report. 2012.

[5] Karl Zeitelhack. Search for alternative techniques to helium-3 based detectors for neutron scattering applications. *Neutron News*, 23(4):10–13, 2012.

[6] Oliver Kirstein, Richard Hall-Wilton, Irina Stefanescu, Maddi Etxegarai, Michail Anastasopoulos, Kevin Fissum, Anna Gulyachkina, Carina Höglund, Mewlude Imam, Kalliopi Kanaki, et al. Neutron position sensitive detectors for the ess. *arXiv preprint arXiv:1411.6194*, 2014.

[7] Richard Hall-Wilton, Carina Höglund, Mewlude Imam, Kalliopi Kanaki, Anton Khaplanov, Oliver Kirstein, Thomas Kittelmann, Björn Nilsson, and Julius Scherzinger. Detectors for the european spallation source. In *Nuclear Science Symposium and Medical Imaging Conference (NSS/MIC), 2012 IEEE*, pages 4283–4289. IEEE, 2012.

[8] Bruno Guerard, Richard Hall-Wilton, and Fabrizio Murtas. Prospects in mpgds development for neutron detection. *arXiv preprint arXiv:1410.0107*, 2014.

[9] Gabriele Croci, Fabrizio Murtas, and Filippo Resnati. Prospects in mpgds development for neutron detection. *arXiv preprint arXiv:1601.01534*, 2016.

[10] F. Sauli. GEM: A new concept for electron amplification in gas detectors. *Nuclear Instruments and Methods in Physics Research*, A(386):531–534, 1997.

[11] Fabio Sauli. The Gas Electron Multiplier (GEM): Operating principles and applications. *Nuclear Instruments and Methods in Physics Research Section A:*

Accelerators, Spectrometers, Detectors and Associated Equipment, 805:2 – 24, 2016. Special Issue in memory of Glenn F. Knoll.

[12] C Altunbas, M Capéans, K Dehmelt, J Ehlers, J Friedrich, I Konorov, A Gandi, S Kappler, B Ketzer, R De Oliveira, et al. Construction, test and commissioning of the triple-gem tracking detector for compass. *Nuclear Instruments and Methods in Physics Research Section A: Accelerators, Spectrometers, Detectors and Associated Equipment*, 490(1):177–203, 2002.

[13] M Alfonsi, G Bencivenni, W Bonivento, A Cardini, P de Simone, F Murtas, D Pinci, M Poli Lener, D Raspino, and B Saitta. The triple-GEM detector for the M1R1 muon station at LHCb. In *Nuclear Science Symposium Conference Record, 2005 IEEE*, volume 2, pages 811–815. IEEE, 2005.

[14] Marco Villa, Serge Duarte Pinto, Matteo Alfonsi, Ian Brock, Gabriele Croci, Eric David, Rui De Oliveira, Leszek Ropelewski, Hans Taureg, and Miranda van Stenis. Progress on large area GEMs. *Nuclear Instruments and Methods in Physics Research Section A: Accelerators, Spectrometers, Detectors and Associated Equipment*, 628(1):182–186, 2011.

[15] Martin Klein and Christian J Schmidt. CASCADE, neutron detectors for highest count rates in combination with ASIC/FPGA based readout electronics. *Nuclear Instruments and Methods in Physics Research Section A: Accelerators, Spectrometers, Detectors and Associated Equipment*, 628(1):9–18, 2011.

[16] G Croci, G Claps, R Caniello, C Cazzaniga, G Grosso, F Murtas, M Tardocchi, E Vassallo, G Gorini, C Horstmann, et al. GEM-based thermal neutron beam monitors for spallation sources. *Nuclear Instruments and Methods in Physics Research Section A: Accelerators, Spectrometers, Detectors and Associated Equipment*, 732:217–220, 2013.

[17] G Croci, G Claps, M Cavenago, M Dalla Palma, G Grosso, F Murtas, R Pasqualotto, E Perelli Cippo, A Pietropaolo, M Rebai, et al. nGEM fast neutron detectors for beam diagnostics. *Nuclear Instruments and Methods in Physics Research Section A: Accelerators, Spectrometers, Detectors and Associated Equipment*, 720:144–148, 2013.

[18] M Köhli, F Allmendinger, W Häußler, T Schröder, M Klein, M Meven, and U Schmidt. Efficiency and spatial resolution of the CASCADE thermal neutron detector. *Nuclear Instruments and Methods in Physics Research Section A: Accelerators, Spectrometers, Detectors and Associated Equipment*, 828:242–249, 2016.

[19] Gordon Leslie Squires. *Introduction to the theory of thermal neutron scattering*. Cambridge university press, 2012.

[20] AJ Allen, MT Hutchings, CG Windsor, and C Andreani. Neutron diffraction methods for the study of residual stress fields. *Advances in Physics*, 34(4):445–473, 1985.

[21] Stephen M. King. Small Angle Neutron Scattering. Technical report, ISIS Facility, STFC Rutherford Appleton Laboratory, 1995.

[22] Colin G. Windsor. *Pulsed neutron scattering*. Taylor & Francis, 1981.

[23] C Andreani, D Colognesi, J Mayers, GF Reiter, and R Senesi. Measurement of momentum distribution of lightatoms and molecules in condensed matter systems using inelastic neutron scattering. *Advances in Physics*, 54(5):377–469, 2005.

[24] Glenn F Knoll. *Radiation detection and measurement*. John Wiley & Sons, 2010.

[25] F Piscitelli, JC Buffet, JF Clergeau, S Cuccaro, B Guerard, Anton Khaplanov, Q La Manna, JM Rigal, and P Van Esch. Study of a high spatial resolution ^{10}B-based thermal neutron detector for application in neutron reflectometry: the Multi-Blade prototype. *Journal of Instrumentation*, 9(03):P03007, 2014.

[26] Francesco Piscitelli. Boron-10 layers, neutron reflectometry and thermal neutron gaseous detectors. *arXiv preprint arXiv:1406.3133*, 2014.

[27] Paul Reuss. *Neutron physics*. EDP sciences, 2012.

[28] TW Crane and MP Baker. Neutron detectors. *Passive Nondestructive Assay of Nuclear Materials*, pages 379–406, 1991.

[29] M Alfonsi, G Bencivenni, I Brock, S Cerioni, G Croci, E David, E De Lucia, R De Oliveira, G De Robertis, D Domenici, et al. Activity of CERN and LNF groups on large area GEM detectors. *Nuclear Instruments and Methods in Physics Research Section A: Accelerators, Spectrometers, Detectors and Associated Equipment*, 617(1):151–154, 2010.

[30] Nist, Composition of KAPTON POLYIMIDE FILM.

[31] Fabio Sauli. *Gaseous radiation detectors: fundamentals and applications*. Number 36. Cambridge University Press, 2014.

[32] M Alfonsi, G Bencivenni, P De Simone, F Murtas, M Poli Lener, W Bonivento, A Cardini, D Pinci, D Raspino, and B Saitta. The LHCb triple-GEM detector for the inner region of the first station of the muon system: construction and module-0 performance. In *Nuclear Science Symposium Conference Record, 2004 IEEE*, volume 1, pages 5–9. IEEE, 2004.

[33] F Murtas, G Croci, A Pietropaolo, G Claps, CD Frost, E Perelli Cippo, D Raspino, M Rebai, NJ Rhodes, EM Schooneveld, et al. Triple GEM gas detectors as real time fast neutron beam monitors for spallation neutron sources. *Journal of Instrumentation*, 7(07):P07021, 2012.

[34] J Benlloch, A Bressan, M Capeáns, M Gruwé, M Hoch, JC Labbé, A Placci, L Ropelewski, and F Sauli. Further developments and beam tests of the Gas Electron Multiplier (GEM). *Nuclear Instruments and Methods in Physics Research Section A: Accelerators, Spectrometers, Detectors and Associated Equipment*, 419(2):410–417, 1998.

[35] Yu Ivaniouchenkov, P Fonte, Vladimir Peskov, and BD Ramsey. Breakdown limit studies in high-rate gaseous detectors. *Nuclear Instruments and Methods in Physics Research Section A: Accelerators, Spectrometers, Detectors and Associated Equipment*, 422(1):300–304, 1999.

[36] P Fonte, V Peskov, and BD Ramsey. Which gaseous detector is the best at high rates. *ICFA Instrum. Bull*, 16, 1998.

[37] J Mayers, J Tomkinson, T Abdul-Redah, WG Stirling, C Andreani, R Senesi, M Nardone, D Colognesi, and E Degiorgi. VESUVIO: the double difference inverse geometry spectrometer at ISIS. *Physica B: Condensed Matter*, 350(1):E659–E662, 2004.

[38] ISIS Home Page: http://www.isis.stfc.ac.uk.

[39] G Croci, C Cazzaniga, M Tardocchi, R Borghi, G Claps, G Grosso, F Murtas, and G Gorini. Measurements of γ-ray sensitivity of a GEM-based detector using a coincidence technique. *Journal of Instrumentation*, 8(04):P04006, 2013.

[40] G Nowak, M Störmer, H-W Becker, C Horstmann, R Kampmann, D Höche, M Haese-Seiller, J-F Moulin, M Pomm, C Randau, et al. Boron carbide coatings for neutron detection probed by x-rays, ions, and neutrons to determine thin film quality. *Journal of Applied Physics*, 117(3):034901, 2015.

[41] Jonathan Correa Magdalena. $^{10}B_4C$ Multi-Grid as an alternative to ^{3}He for Large Area Neutron Detectors. 2012.

[42] http://www.srim.org.

[43] Francesco Piscitelli and Patrick Van Esch. Analytical modeling of thin film neutron converters and its application to thermal neutron gas detectors. *Journal of Instrumentation*, 8(04):P04020, 2013.

[44] Walter Bonivento, P Jarron, D Moraes, W Riegler, and F Dos Santos. Development of the CARIOCA front-end chip for the LHCb muon detector. *Nuclear*

Instruments and Methods in Physics Research Section A: Accelerators, Spectrometers, Detectors and Associated Equipment, 491(1):233–243, 2002.

[45] M Zoppi F Grazzi, M Celli. INES: Italian Neutron Experimental Station @ ISIS (UK), INES report N.1. Technical report, ISIS, 2004.

[46] WCA Pulford, SPH Quinton, MW Johnson, and J Norris. Future data acquisition at isis. In *Institute of physics conference series*, number 97, pages 537–547. IOP PUBLISHING LTD DIRAC HOUSE, TEMPLE BACK, BRISTOL BS1 6BE, ENGLAND, 1989.

[47] A Miceli, G Festa, R Senesi, E Perelli Cippo, L Giacomelli, M Tardocchi, A Scherillo, E Schooneveld, C Frost, G Gorini, et al. Measurements of gamma-ray background spectra at spallation neutron source beamlines. *Journal of Analytical Atomic Spectrometry*, 29(10):1897–1903, 2014.

[48] Mantid Project Home Page: http://www.mantidproject.org/main_page.

[49] Owen Arnold, Jean-Christophe Bilheux, JM Borreguero, Alex Buts, Stuart I Campbell, L Chapon, M Doucet, N Draper, R Ferraz Leal, MA Gigg, et al. Mantid—data analysis and visualization package for neutron scattering and μ sr experiments. *Nuclear Instruments and Methods in Physics Research Section A: Accelerators, Spectrometers, Detectors and Associated Equipment*, 764:156–166, 2014.

[50] http://www-llb.cea.fr/en/web/hpr_web/hprweb1.php.

[51] http://www.isis.stfc.ac.uk/instruments/rotax/rotax-6463.html.

[52] H Tietze-Jaensch, W Kockelmann, W Schmidt, and G Will. The ROTAX/DIFF time-of-flight diffractometer at ISIS. *Physica B: Condensed Matter*, 234:1149–1151, 1997.

[53] Michael D Abràmoff, Paulo J Magalhães, and Sunanda J Ram. Image processing with ImageJ. *Biophotonics international*, 11(7):36–42, 2004.

[54] HET Home Page: http://www.isis.stfc.ac.uk/instruments/het/het6915.html.

[55] Ansys home page: http://www.ansys.com.

[56] Tadeusz Stolarski, Y Nakasone, and Shigeka Yoshimoto. *Engineering analysis with ANSYS software*. Butterworth-Heinemann, 2011.

[57] Höglund C et al. B_4C thin films for neutron detection. *J. Appl. Phys.*, 111 104908, 2012.

[58] Höglund C et al. Stability of $^{10}B_4C$ thin films under neutron radiation. *Radiat. Phys. Chem.*, 113:14–9, 2015.

[59] https://web.infn.it/gemini/index.php/hvgem.

[60] http://www.crystals.saint-gobain.com/sites/imdf.crystals.com/files/documents/glass-scintillator-material-data-sheet_69772.pdf.

[61] K. Kanaki A. J. Jackson. ESS construction proposal. LoKI a broadband SANS instrument. Technical report, European Spallation Source.

[62] A. J. Jackson et al. LoKI - a broad band high flux SANS instrument for the ESS. *Proceedings ICANS XXI*, 2015.

[63] https://ess-ics.atlassian.net/wiki/display/dg/geant4simulationframework.

[64] Thomas Kittelmann, Irina Stefanescu, Kalliopi Kanaki, Mirko Boin, Richard Hall-Wilton, and Karl Zeitelhack. Geant4 based simulations for novel neutron detector development. In *Journal of Physics: Conference Series*, volume 513, page 022017. IOP Publishing, 2014.

[65] https://geant4.web.cern.ch/geant4/.

Synopsis of attached papers

This thesis is based on the following papers, which are referred to in the text:

I **Neutron beam imaging with GEM detectors.**

Neutron GEM-based detectors represent a new frontier of devices in neutron physics applications where a very high neutron flux must be measured such as future fusion experiments (e.g. ITER Neutral beam Injector) and spallation sources (e.g. the European Spallation source). This kind of detectors can be properly adapted to be used both as beam monitors but also as neutron diffraction detectors that could represent a valid alternative for the ^{3}He detectors replacement. Fast neutron GEM detectors (nGEM) feature a cathode composed by one layer of polyethylene and one of aluminium (neutron scattering on hydrogen generates protons that are detected in the gas) while thermal neutron GEM detectors (bGEM) are equipped with a borated aluminium cathode (charged particles are generated through the $^{10}\mathrm{B}(n,\alpha)^7\mathrm{Li}$ reaction). GEM detectors can be realised in large area ($\approx 1\,\mathrm{m}^2$) and their readout can be pixelated. Three different prototypes of nGEM and one prototype of bGEM detectors of different areas and equipped with different types of readout have been built and tested. All the detectors have been used to measure the fast and thermal neutron 2D beam image at the ISIS-VESUVIO beam line. The different kinds of readout patterns (different areas of the pixels) have been compared in similar conditions. All the detectors measured a width of the beam profile

consistent with the expected one. The imaging property of each detector was then tested by inserting samples of different material and shape in the beam. All the samples were correctly reconstructed and the definition of the reconstruction depends on the type of readout anode. The fast neutron beam profile reconstruction was then compared to the one obtained by diamond detectors positioned on the same beam line while the thermal neutron one was compared to the imaged obtained by cadmium-coupled x-rays films. Also efficiency and γ-ray background rejection have been determined. These prototypes represent the first step towards the realisation of new neutron beam monitors for fusion experiments and spallation sources.

II **Diffraction measurements with a boron-based GEM neutron detector.**

The research of reliable substitutes of ^{3}He detectors is an important task for the affordability of new neutron scattering instrumentation for future spallation sources like the European Spallation Source. GEM (Gas Electron Multiplier)-based detectors represent a valid alternative since they can combine high-rate capability, coverage of up to 1 m^2 area and good intrinsic spatial resolution (for this detector class it can be better than 0.5 mm). The first neutron diffraction measurements performed using a borated GEM detector are reported in this paper. The detector has an active area of $10 \times 5\,\mathrm{cm}^2$ and is equipped with a borated cathode. The GEM detector was read out using the standard ISIS Data Acquisition System. The comparison with measurements performed with standard ^{3}He detectors shows that the broadening of the peaks measured on the diffractogram obtained with the GEM is $20 - 30\%$ wider than the one obtained by ^{3}He tubes but the active area of the GEM is twice that of ^{3}He tubes. The GEM resolution is improved if half of its active area is considered. The

signal-to-background ratio of the GEM is about 1.5 to 2 times lower than that of ^{3}He. This measurement proves that GEM detectors can be used for neutron diffraction measurements and paves the way for their use at future neutron spallation sources.

III **A GEM-based thermal neutron detector for high counting rate applications.**

In this paper, we present the results of a GEM-based neutron detector in a high-flux environment (the ORPHE reactor in Saclay), especially in terms of maximum rate capability and linearity. Recorded data show that the detector can manage neutron counting rates in the order of 50×10^6 counts/scm^2 while maintaining a reasonable linearity and with no sign of instability.

IV **Neutron radiography as a non-destructive method for diagnosing neutron converters for advanced thermal neutron detectors.**

The efficiency of GEM-based neutron detectors can be increased by using a three dimensional neutron converter cathode (3D-C). The 3D-C is composed by a series of alumina (Al_2O_3) lamellas coated by 1 μm of ^{10}B enriched boron carbide (B_4C). In order to obtain a good characterisation in terms of detector efficiency and uniformity it is crucial to know the thickness, the uniformity and the atomic composition of the B_4C neutron converter coating. In this work a non-destructive technique for the characterisation of the lamellas composing the 3D-C was performed using neutron radiography. The results of these measurements show have coating uniformity suitable for detector applications. This technique (compared with SEM, EDX, ERDA, XPS) has the advantage of being global (*i.e.* non point-like) and non-destructive, thus it is suitable as a check method for mass production of the 3D-C elements.

V **Evolution in boron-based GEM detectors for diffraction measurements: from planar to 3D converters.**

In this paper the evolution of boron- based GEM detectors from planar to 3D converters (3D-C) with an application in diffraction measurements is presented. The use of 3D-C coupled with GEMs allows for an optimisation of the detector performance. Three different detectors were used for diffraction measurements on the INES instrument at the ISIS spallation source. The performances of the GEM-detectors are compared with those of conventional ^{3}He tubes installed on the INES instrument. The detector equipped with the 3D-C reached a count rate per unit area of about 25% relative to the currently installed ^{3}He tube. Its timing resolution is similar and the signal-to-background ratio (S/B) is 2 times lower.

Paper I

PUBLISHED BY IOP PUBLISHING FOR SISSA MEDIALAB

RECEIVED: *September 29, 2014*
REVISED: *January 23, 2015*
ACCEPTED: *February 20, 2015*
PUBLISHED: *April 30, 2015*

16th INTERNATIONAL WORKSHOP ON RADIATION IMAGING DETECTORS
22–26 JUNE 2014,
TRIESTE, ITALY

Neutron beam imaging with GEM detectors

G. Albani,[a,1] **G. Croci,**[b] **C. Cazzaniga,**[a] **M. Cavenago,**[c] **G. Claps,**[d] **A. Muraro,**[b] **F. Murtas,**[c] **R. Pasqualotto,**[d] **E. Perelli Cippo,**[b] **M .Rebai,**[a] **M. Tardocchi**[b] **and G. Gorini**[a]

[a] *INFN e Universitá degli Studi di Milano-Bicocca, Piazza della Scienza 3, 20126 Milano, Italy*
[b] *Istituto di Fisica del Plasma "P. Caldirola", CNR, Via Roberto Cozzi 53, 20126 Milano, Italy*
[c] *INFN — LNF, Via E. Fermi 40, 00044 Frascati, Italy*
[d] *Consorzio RFX, Corso Stati Uniti 4, 35127 Padova, Italy*

E-mail: giorgia.albani@mib.infn.it

[1] Corresponding author.

doi:10.1088/1748-0221/10/04/C04040

ABSTRACT: Neutron GEM-based detectors represent a new frontier of devices in neutron physics applications where a very high neutron flux must be measured such as future fusion experiments (e.g. ITER Neutral beam Injector) and spallation sources (e.g. the European Spallation source). This kind of detectors can be properly adapted to be used both as beam monitors but also as neutron diffraction detectors that could represent a valid alternative for the ^{3}He detectors replacement. Fast neutron GEM detectors (nGEM) feature a cathode composed by one layer of polyethylene and one of aluminium (neutron scattering on hydrogen generates protons that are detected in the gas) while thermal neutron GEM detectors (bGEM) are equipped with a borated aluminium cathode (charged particles are generated through the ^{10}B(n,α)^{7}Li reaction). GEM detectors can be realized in large area (1 m^2) and their readout can be pixelated. Three different prototypes of nGEM and one prototype of bGEM detectors of different areas and equipped with different types of readout have been built and tested. All the detectors have been used to measure the fast and thermal neutron 2D beam image at the ISIS-VESUVIO beamline. The different kinds of readout patterns (different areas of the pixels) have been compared in similar conditions. All the detectors measured a width of the beam profile consitent with the expected one. The imaging property of each detector was then tested by inserting samples of different material and shape in the beam. All the samples were correctly reconstructed and the definition of the reconstruction depends on the type of readout anode. The fast neutron beam profile reconstruction was then compared to the one obtained by diamond detectors positioned on the same beamline while the thermal neutron one was compared to the imaged obtained by cadmium-coupled x-rays films. Also efficiency and the gamma background rejection have been determined. These prototypes represent the first step towards the realization of new neutron beam monitors for fusion experiments and spallation sources.

KEYWORDS: Gaseous detectors; Micropattern gaseous detectors (MSGC, GEM, THGEM, RETHGEM, MHSP, MICROPIC, MICROMEGAS, InGrid, etc); Gaseous imaging and tracking detectors; Electron multipliers (gas)

2015 JINST 10 C04040

Contents

1 Introduction **1**

2 Detectors **2**
- 2.1 Performance 2
  - 2.1.1 nGEM perfomance 3
  - 2.1.2 bGEM performance 3
  - 2.1.3 γ-ray rejection 3

3 ISIS VESUVIO facility **4**

4 Neutron imaging **5**
- 4.1 Imaging of samples inserted in the neutron beam 6
- 4.2 Comparison between nGEM and diamond detector 6
- 4.3 Comparison between the bGEM and the cadmium-coupled X-ray technique 7

5 Conclusions **9**

2015 JINST 10 C04040

1 Introduction

New high flux and large area neutron detectors are needed for future fusion experiments and spallation sources. The construction of the CNESM diagnostic system of the SPIDER NBI prototype for ITER [1] requires a fast neutron detector with a millimetric space resolution in order to qualify neutron beams in applications related to nuclear fusion. Furthermore the ^{3}He shortage limits its use in applications including future neutron sources like ESS [2] where large areas (several m^2) and high efficiency ($> 50\%$) detectors are needed for both fast and thermal neutrons. In this framework, GEM (Gas Electron Multiplier) is one of the explored detector technologies [3]. GEMs [4–6] were invented at CERN as charged particle detectors but, if a proper cathode is chosen, they can be used also as neutral particles detectors [7–11]. GEMs can be used as beam monitors because they can provide directionality, γ-ray rejection, linearity, adequate spatial and time resolution and real time operation. This paper explores the characteristics of GEMs in terms of imaging performances either for fast and thermal neutrons. All the measurements were performed at the ISIS-RAL (UK) VESUVIO neutron beamline [12] which features a mixed neutron spectrum consisting of a thermal/epithermal component and a fast neutron component falling of as $1/E_n$ where E_n is the neutron energy.

2 Detectors

Four GEMs were built and tested as prototypes of new, high-rate detectors for fusion experiments and spallation sources. One of the main features of this technology is the fact that the conversion and the multiplication regions are decoupled. This modularity allows the GEM to be adaptable to detect different particles choosing a suitable converter cathode. Three fast neutron GEMs (nGEM) [1, 13, 14] were built and tested for the CNESM neutron diagnostic and one thermal neutron GEM (bGEM) [15, 16] was built as a thermal neutron beam monitor for future thermal neutron beamlines at ESS. A GEM for neutrons is equipped with a cathode that "converts" neutrons into charged particles through a nuclear reaction. The energetic products can cross the cathode and ionize the gas producing electrons that are multiplied in the GEM foils. The signal is induced on a padded anode connected to the front end electronics composed by CARIOCA-GEM digital chips [17] connected to a custom made FPGA mother board [18] that analyzes the signal coming from the chips. The gas mixture employed is Ar/CO2 70/30 for all detectors. To detect fast neutrons ($\sim$ MeV) an Al/CH_2 cathode is used. The elastic scattering of a neutron on a H atom in CH_2 gives origin to a recoil proton that can be detected and carries information about the interacting neutron. On the other hand thermal neutrons are converted into charged particles through the nuclear reaction ^{10}B(n,α)^{7}Li if a cathode composed by an aluminum plate coated by a uniform thick boron carbide (B_4C) film is used. The main features of the four GEM detectors are summarized in table 1. The cathode of the bGEM detector is composed of an Al layer (400 μm thick) covered by a natural (not enriched) B_4C coating 1 μm thick. The B_4C layer was obtained by courtesy of the Institute of Materials Research, HELMHOLTZ-ZENTRUM GEESTHACHT (Germany) using a PVD DC Magnetron Sputtering Technique [19]. The gap geometry is the relative distance between the five parts of the detector (Cathode,GEM-1, GEM-2, GEM-3 and anode). Figure 1 shows the padded anodes used in the construction.

Table 1. Relevant parameters of the four GEM detectors.

Detector	Cathode	Gap geometry	Total number of pads	Pad dimensions	Active area
nGEM-1	60 μm CH_2+ 40 μm Al	3/1/2/1 mm	128	$12 \times 6\,mm^2$	$10 \times 10\,cm^2$
nGEM-2	50 μm CH_2+ 50 μm Al	3/1/2/1 mm	136	$8 \times 8\,mm^2$	$10 \times 10\,cm^2$
nGEM-3	150 μm CH_2+ 50 μm Al	4/2/2/2 mm	256	$22 \times 13\,mm^2$	$20 \times 35\,cm^2$
bGEM	1 μm B_4C + 400 μm Al	13/2/3/1 mm	136	$8 \times 8\,mm^2$	$10 \times 10\,cm^2$

2.1 Performance

The counting rate of bGEM and nGEM-1 detectors exposed to different particles was measured as a function of the effective gain. If the gas mixture and the electronic thresholds are set, the effective gain changes by varying the sum of potential difference over the three GEM foils ($\Sigma\Delta V_{GEM} = V_{GEM}$) and the results are shown in figure 2.

2015 JINST 10 C04040

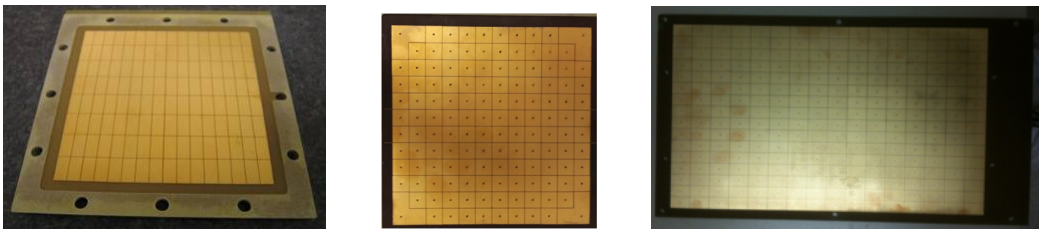

(a) (b) (c)

Figure 1. Photographs of the padded readout anodes of the nGEM and bGEM prototypes. (a) 128 pads with dimensions $12 \times 6\,\mathrm{mm}^2$ and active area $10 \times 10\,\mathrm{cm}^2$. (b) 132 pads with dimensions $8 \times 8\,\mathrm{mm}^2$ plus 4 L-shaped pads with an area of $192\,\mathrm{mm}^2$ and a total active area $10 \times 10\,\mathrm{cm}^2$. (c) 256 pads with dimensions $22 \times 13\,\mathrm{mm}^2$ and active area $20 \times 35\,\mathrm{cm}^2$.

2.1.1 nGEM perfomance

The nGEM-1 and the bGEM neutron counting rates in figure 2 have a different trend. As shown in figure 2(a) the nGEM-1 starts to detect fast neutrons at $V_{GEM} = 750\,V$ and the counting rate is an increasing function of V_{GEM}. The nGEM-1 detects recoil protons from the CH_2 layer. The range of the recoil protons in Ar/CO_2 70/30 (tens of cm) is larger than the detector thickness, so only a fraction of their energy is deposited in the gas. Moreover the stopping power is inversely proportional to v^2, so protons of higher energy deposit a lower fraction in the gas. The lack of a shoulder is due to both the incomplete proton energy deposition and the continuous neutron spectrum of VESUVIO (see section 3). The working point is set equally at $V_{GEM} = 870\,V$, in order to guarantee good γ-ray rejection (see section 2.1.3). For what is concerning the rate stability in absence of an efficiency plateau, previous measurements [14] have shown a good intrinsic stability of the detector; however for the sake of applications of GEMs as a beam monitor, the environmental parameters that may affect the gain (gas temperature and pressure) and the electronic threshold should be carefully monitored during operations.

2.1.2 bGEM performance

The bGEM starts to detect thermal neutrons at $V_{GEM} = 710\,V$ as shown in figure 2(b). The counting rate is an increasing function of V_{GEM} but a wide counting rate plateau is present between 825 V and 925 V ($60 < \text{gain} < 400$) where the maximum detection efficiency is reached [1, 13, 20]. Indeed the alphas and the ions produced in the conversion process are completely stopped in the gas because the maximum range is 7 mm. This range refers to alphas and ions emitted at the boundary between the B_4C layer and the gas: if an alpha particle is emitted deep in the layer it may not reach the gas or reach it with a reduced energy and corresponding shorter range in the gas mixture [21]. The presence of such plateau leads to a natural choice of $V_{GEM} = 870\,V$ as the working point, representing the optimal compromise between gain stability and γ-ray rejection.

2.1.3 γ-ray rejection

When the beam is off the GEMs detect particles not correlated in time with the pulsed neutron beam (see section 3), that are mainly photons coming from surrounding materials activation. These

2015 JINST 10 C04040

γ-rays represent one of the possible sources of background during neutron measurements. In addition also neutrons of "wrong" energy (thermal neutrons when you are detecting fast neutrons and viceversa) and γ-rays generated by the spallation process represent other background sources. This problem was already accessed by the present authors in previous works. Reference [20] describes a detailed study in order to understand the γ-ray sensitivity of these kind of detectors scanning the LLD threshold and the V_{GEM}. In addition reference [14] shows the results obtained by specific measurement performed by inserting filters of different materials in the beam. These works indicate that for $V_{GEM} < 900$ V (gain < 100) both detectors are insensitive to γ-rays. This is due to the fact that the byproducts of the neutron conversion reactions deposit a much higher energy in the gas with respect to electrons mostly generated by Compton scattering of γ-rays on the solid material of the detector. Since the deposited energy is directly connected to the primary charge liberated in the detector, keeping the GEM gain less than about 100 guarantees that γ-rays-induced signals fall below the thresholds set for electronic noise rejection (in the order of 1400 mV for CARIOCA chips). The working point for both detectors is thus set up at $V_{GEM} = 870$ V where the detectors are insensitive to γ-rays and where the detectors efficiencies are about 10^{-4} [13] for nGEM and 10^{-2} [15] for bGEM.

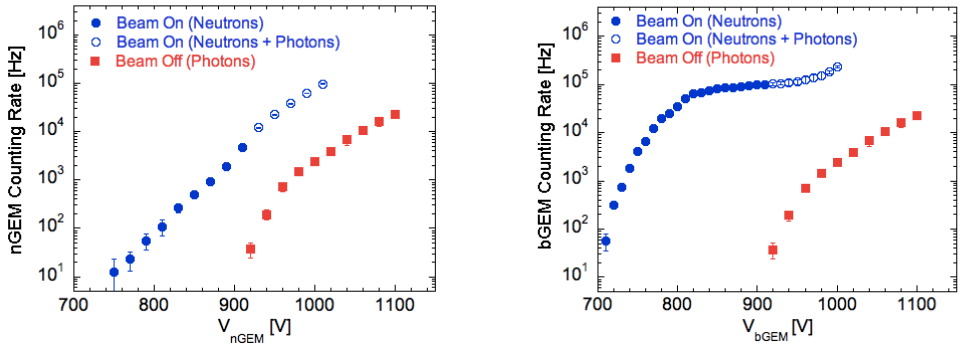

(a) (b)

Figure 2. nGEM-1 (a) and bGEM (b) counting rate as a function of V_{GEM} when the neutron beam is on and off.

3 ISIS VESUVIO facility

All the measurements were performed at the VESUVIO [12] beamline at a flight distance of about $L = 12.5$ m from the neutron source. At ISIS, neutrons are produced by a 800 MeV proton beam with a double bunch fine structure and a repetition frequency of 50 Hz. The two proton bunches are about 70 ns wide (FWHM) and 322 ns apart. The proton beam delivers an average current of 180 μAh on a Ta-W target yielding about 30 neutrons per incident proton. The VESUVIO beam profile widths FWHMx and FWHMy are in a range between approximately 30 mm and 40 mm (as obtained with the Cadmium-film method described in section 4.3). Being VESUVIO an undermoderated neutron beamline, the energy range of neutrons spans from thermal energies up to, in principle, 800 MeV, with an excess of high energy neutrons with respect to a (moderated)

2015 JINST 10 C04040

Maxwell-Boltzmann distribution [12]. A detailed shape of the VESUVIO spectrum is reported in reference [22]. Here we just mention that Bedogni et al. measured a fluence fraction of about 46.9% for $E_n < 0.4\,eV$, 40.9% for $0.4\,eV < E_n < 100\,keV$, 11.5% for $100\,keV < E_n < 10\,MeV$ and 0.7% for $E_n > 100\,MeV$.

4 Neutron imaging

The imaging properties of the nGEM and bGEM detectors could be tested by reconstructing the bi-dimensional VESUVIO beam profile. All four detectors were exposed to the neutron beam for a few minutes. Figure 3 shows the bi-dimensional VESUVIO beam profile reconstructed with the detectors.

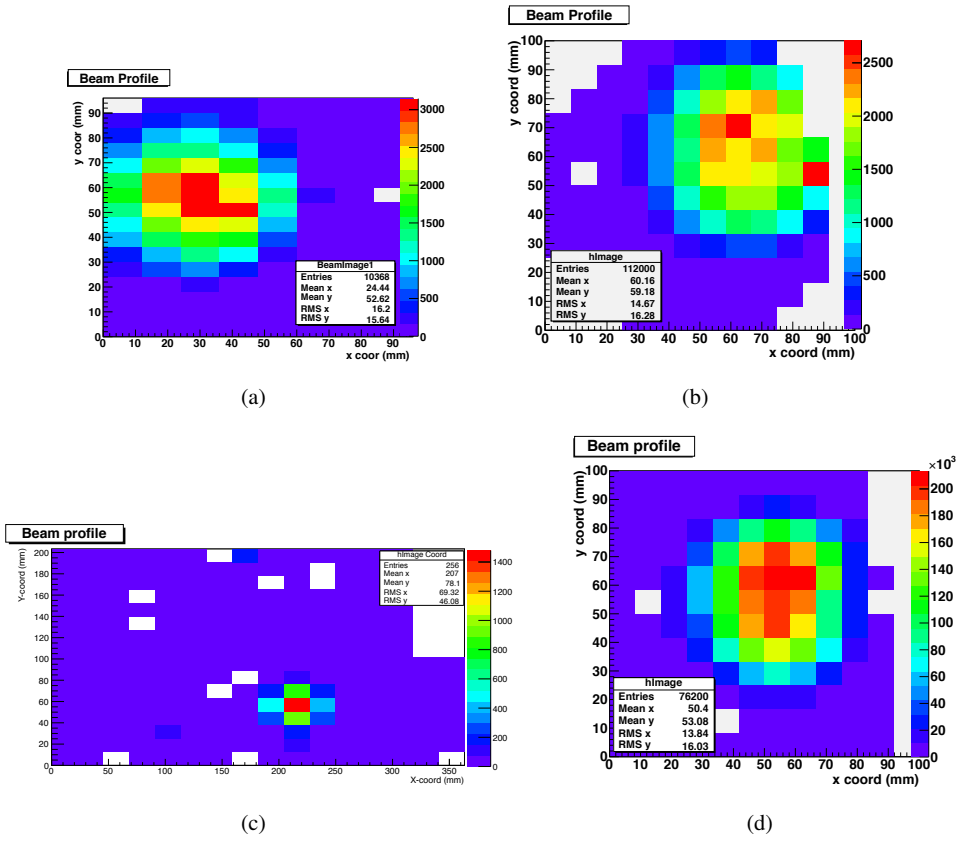

Figure 3. 2D map of the beam intensity distribution as number of events over threshold recorded at each readout pad of the detectors nGEM-1 (a), nGEM-2 (b), nGEM-3 (c) and bGEM (d).

A bell-shaped profile is visible if the counting rate is projected on the x and y axes for each detector. Such curves were fitted with simple Gaussian functional forms and the FWHMs of such fits taken as indication of the beam size (see table 2). It is expected the measurements for the different nGEM detectors are compatible within the errors on the FWHMs. The precision on the FWHM depends on the pad dimensions. The errors on the FWHMs are presented in table 2 both as

2015 JINST 10 C04040

estimated by the fitting procedure (least-square method) and as derived by the constant probability distribution method on the pads, i.e. $z/\sqrt{(12)}$, being z the pad dimension. The latter value sets indeed an intrinsic limit for the precision on the determination of FWHMs, and thus it is a more realistic estimated error. Within such error level, the values obtained from the three nGEMs are compatible. In general neutrons of different energies are not be transported in the same way along the beam. In particular, it is expected that the thermal beam profile is narrower than the fast one, because neutron absorption of the collimators along the beamline is more effective for lower energy neutrons. However this effect is not apparent in the data obtained by the bGEM: if present, it may be smaller than the available resolution of the instrument, the FWHM obtained with the latter being also compatible with the nGEM results. The FWHMs of the beam imaged by these detectors are compared with the beam imaged by other detectors sensible to the same neutron energy range (see sections 4.2 and 4.3). We performed a scan of each detector moving the center of the beam along all pads taking several measurements of the beam profile and all the reconstructed FWHM (both X and Y) were reproducible within 5%.

Table 2. Results of a bi-dimensional fit of the reconstructed beam are shown.

Detectors	FWHM x	σ_{FWHMx} fit	σ_{FWHMx}	FWHM y	σ_{FWHMy} fit	σ_{FWHMy}	pads FWHM x	pads FWHM y
nGEM-1	37.94	0.13	4.89	35.37	0.10	2.44	3	6
nGEM-2	39.96	0.19	3.25	41.17	0.13	3.25	5	5
nGEM-3	34.37	0.37	8.96	27.05	0.28	5.29	2	2
bGEM	31.64	0.01	3.25	37.20	0.01	3.25	4	5

4.1 Imaging of samples inserted in the neutron beam

In order to test the capability of image reconstruction of these detectors, samples of different material and shape were inserted in the beam. Figure 4(a) shows the reconstructed beam profile with the nGEM-1 when a 25 cm thick block of CH_2 is inserted in the beam. The thickness of the CH_2 prevents fast neutrons to reach the nGEM detector and only half of the beam could be imaged. Figure 4(b) shows the reconstructed beam profile with the bGEM when a 1 mm thick L-shape Cadmium sheet is inserted in the beam. The ^{113}Cd isotope absorbs with very high probability neutrons with energy lower than the cadmium cut-off at 0.5 eV and transmits the faster ones. As a consequence the negative image of the cadmium foil is expected on the bGEM detector. The shape of the block is highlighted in the 2D histogram, even if the negative image is not as "black" as the off-beam regions. This is due to neutrons scattered (by the Cadmium itself or other surrounding materials), neutrons with energies over the Cd cut-off transmitted through the foil and the divergence of the beam (estimated about 0.01 deg).

4.2 Comparison between nGEM and diamond detector

The fast neutron beam profile reconstruction was compared to the one obtained by a diamond detector positioned on the same beamline. This detector is constituted by a commercial single crystal

2015 JINST 10 C04040

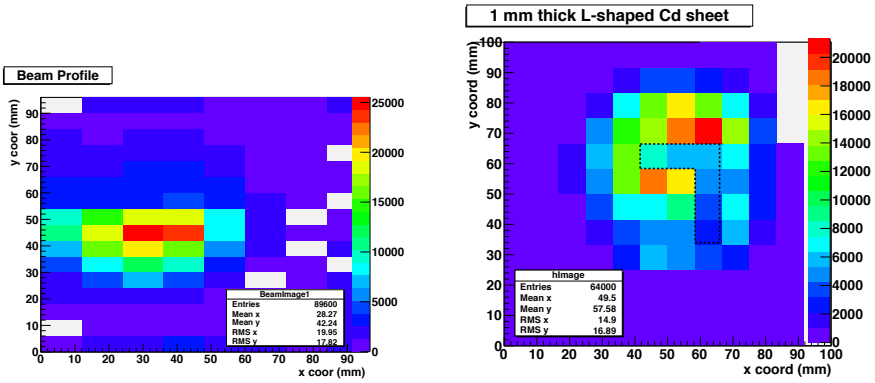

(a) (b)

Figure 4. (a) The reconstructed beam profile with the nGEM-1 when a 25 cm thick block of CH_2 is inserted in the beam. (b) The reconstructed beam profile with the bGEM when a sheet of Cadmium with L-shape is inserted in the beam.

diamond detector with dimensions $4.5 \times 4.5 \times 0.5\,\mathrm{mm}^3$ [23]). In order to measure the full beam profile it was installed in front of the nGEM-1 detector and was moved in steps of 5 mm recording the counting rate at each position. A LLD threshold of 10 MeV was applied to the neutron energy deposition inside the crystal. The results of the measurements are shown in figure 5 where the counting rates of the diamond and of the nGEM-1 are plotted along the x axis superimposing the maxima. The beam profile obtained with the diamond is somehow wider than the nGEM one ($\mathrm{FWHM_{nGEM}} = 33.72\,\mathrm{mm}$; $\mathrm{FWHM_{diam}} = 37,01\,\mathrm{mm}$). This is due to the higher sensitivity of diamond to higher energy neutrons that are therefore less efficiently collimated (details of the energy dependence of counting efficiencies for diamond and GEM are given in [14, 23]. In fact, while the diamond is sensitive to neutron with energies $\mathrm{E_n} > 10\,\mathrm{MeV}$, the nGEM maximum sensitivity for neutron energies is about 6 MeV.

4.3 Comparison between the bGEM and the cadmium-coupled X-ray technique

The thermal neutron beam profile imaged with the bGEM was also compared to the one obtained by the cadmium-coupled X-ray sensitive films used at VESUVIO for sample alignment. In this case the beam profile is imaged by an X-ray sensitive film (typically Kodak DEF) in a light-tight holder, coupled with a 0.5 mm thick Cd foil. Following thermal neutron capture, the cadmium foil gets excited and emits X-rays that expose the film. Due to the very high absorption cross section of cadmium, the mean free path of neutrons into the foil is negligible, thus the X-ray induced blackening of the film is representative of the striking positions of neutrons on the foil surface. The sensitivity of the film itself to neutrons is negligible, so neutrons with energy higher than 0.5 eV are transmitted by the Cadmium foil and the film. Figure 6(a) shows the beam image obtained with this technique and figure 6(b) shows its plot profile. The die-off on the edge of the film image is due to multiple effects. Firstly, the beam itself being not uniform but bell-shaped, then the non-linearity of the film blackening with photon exposure, and finally the blurring effect due to the 4π emission of photons. Separating such effects is not straightforward, and so is the estimate of the width of the

2015 JINST 10 C04040

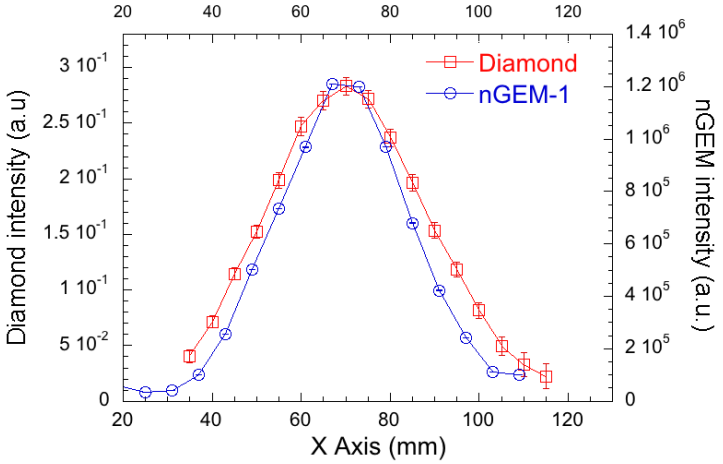

Figure 5. Comparison of the counting rates of the nGEM-1 and the diamond detector in the horizontal direction.

beam. Moreover, the non-linearity of the film blackening causes a strong saturation effect visible in the figure 6(b), so that the resulting shape of the beam profile is by no means approximated by a Gaussian. It is still possible to approximately indicate the FWHM, but hardly to make a correct esteem of associated error based on a statistical procedure. The FWHMs of the blackening intensity are superimposed to the picture in figure 6(a) for x and y directions. They are about 34 mm and 32 mm respectively, that is consistent with the results of the FWHM of the bGEM profile in the horizontal dimension that is 32 mm.

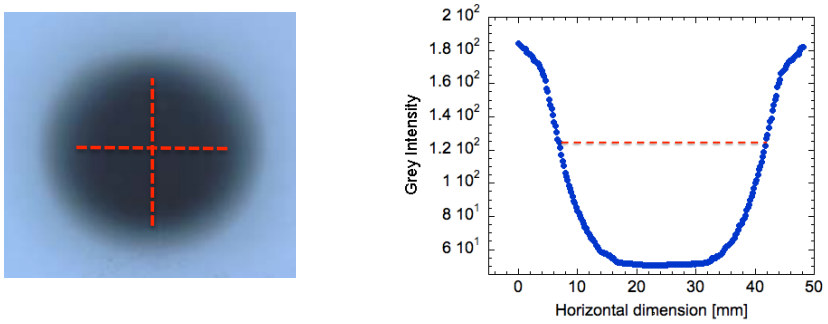

(a) (b)

Figure 6. (a) Image of the VESUVIO beam with the Cadmium-coupled X-rays technique. The dashed lines mark the FWHM of the blackening intensity in x and y axes. (b) Plot profile on the x axis. The grey intensity is in 8 bit. The dynamic range of the Kodak DEF with respect to the used scanner ranges from about 50 (saturation of the film) to about 190 (unexposed film). The dashed line marks the FWHM.

2015 JINST 10 C04040

5 Conclusions

The obtained results demonstrate that all four nGEM and bGEM detectors are able to image the bi-dimensional beam profiles of VESUVIO and the measured widths are consistent with the other available measurements. In the case of the nGEMs the imaged beam profile was compared with one obtained by a single crystal diamond detector. A comparison is made also between the bGEM and the cadmium-coupled x-rays technique and the results are compatible within the estimated errors. Efficiency in detecting fast (thermal) neutrons and insensitivity to other neutral particles as thermal (fast) neutrons and gamma rays demonstrate that nGEM (bGEM) detectors can be used as fast (thermal) neutron beam monitor. The detector spatial resolution can be modified simply changing the type of the readout anode: indeed the pad dimensions set the physical limit to the resolution. This is the first step towards the realization of new neutron beam monitors for fusion experiments and spallation sources. The future perspective is to perform a more detailed study of the resolution, the energy sensitivity range and the background characterization.

Acknowledgments

This work was set up in collaboration and financial support of Fusion for Energy and of INFN Group 5 (Technology Research). This publication reflects the view only of the authors and Fusion for Energy cannot be held responsible for any use which may be made of the information contained here. The views and opinion expressed herein do not necessarily reflect those of ITER organization.

References

[1] G. Croci et al., *nGEM neutron diagnostic concept for high power deuterium beams*, 2012 *JINST* **7** C03010.

[2] https://europeanspallationsource.se.

[3] B. Guerard, R. Hall-Wilton and F. Murtas, *Prospects in MPGDs development for neutron detection*, RD51-NOTE-2014-003 (2014).

[4] F. Sauli, *GEM: A new concept for electron amplification in gas detectors*, *Nucl. Instrum. Meth.* **A 386** (1997) 531.

[5] S. Duarte Pinto et al., *Progress on large area GEMs*, 2009 *JINST* **4** P12009.

[6] M. Villa et al., *Progress on large area GEMs*, *Nucl. Instrum. Meth.* **A 628** (2011) 182 [arXiv:1007.1131].

[7] M. Alexeev et al., *Micropattern gaseous photon detectors for Cherenkov imaging counters*, *Nucl. Instrum. Meth.* **A 623** (2010) 129.

[8] M. Alexeev et al., *THGEM based photon detector for Cherenkov imaging applications*, *Nucl. Instrum. Meth.* **A 617** (2010) 396.

[9] M. Alexeev et al., *Development of THGEM-based photon detectors for Cherenkov Imaging Counters*, 2010 *JINST* **5** P03009.

[10] M. Klein and C.J. Schmidt, *CASCADE, neutron detectors for highest count rates in combination with ASIC/FPGA based readout electronics*, *Nucl. Instrum. Meth.* A 628 (2011) 9.

2015 JINST 10 C04040

Paper II

A Letters Journal Exploring the Frontiers of Physics

July 2014

EPL, **107** (2014) 12001
doi: 10.1209/0295-5075/107/12001

www.epljournal.org

Diffraction measurements with a boron-based GEM neutron detector

Gabriele Croci[1,5(a)], Giorgia albani[2], Carlo Cazzaniga[2], Enrico Perelli Cippo[1], Erik Schooneveld[3], Gerardo Claps[4], Anna Cremona[1], Giovanni Grosso[1], Andrea Muraro[1], Fabrizio Murtas[4], Marica Rebai[2], Antonella Scherillo[3], Marco Tardocchi[1] and Giuseppe Gorini[2,5]

[1] *Istituto di Fisica del Plasma (IFP-CNR) - Via Cozzi 53, 20125 Milano, Italy*
[2] *Dipartimento di Fisica, Università degli studi di Milano Bicocca - Piazza della Scienza 3, 20126 Milano, Itlay*
[3] *STFC-ISIS Facility, RAL - OX11 0Q, Didcot, UK*
[4] *INFN - Laboratori Nazionali di Frascati - Via Fermi 40, 0044 Frascati, Italy*
[5] *INFN - Sezione di Milano-Bicocca - Piazza della Scienza 3, 20126 Milano, Italy*

received 24 April 2014; accepted in final form 13 June 2014
published online 7 July 2014

PACS 28.20.Cz – Neutron scattering
PACS 29.40.-n – Radiation detectors
PACS 29.40.Cs – Gas-filled counters: ionization chambers, proportional, and avalanche counters

Abstract – The research of reliable substitutes of ^{3}He detectors is an important task for the affordability of new neutron scattering instrumentation for future spallation sources like the European Spallation Source. GEM (Gas Electron Multiplier)-based detectors represent a valid alternative since they can combine high-rate capability, coverage of up to 1 m^2 area and good intrinsic spatial resolution (for this detector class it can be better than 0.5 mm). The first neutron diffraction measurements performed using a borated GEM detector are reported. The detector has an active area of 10×5 cm^2 and is equipped with a borated cathode. The GEM detector was read out using the standard ISIS Data Acquisition System. The comparison with measurements performed with standard ^{3}He detectors shows that the broadening of the peaks measured on the diffractogram obtained with the GEM is 20–30% wider than the one obtained by ^{3}He tubes but the active area of the GEM is twice that of ^{3}He tubes. The GEM resolution is improved if half of its active area is considered. The signal-to-background ratio of the GEM is about 1.5 to 2 times lower than that of ^{3}He. This measurement proves that GEM detectors can be used for neutron diffraction measurements and paves the way for their use at future neutron spallation sources.

Introduction. – Due to the present ^{3}He worldwide shortage [1], an intense R&D phase [2] has been started in order to realize ^{3}He-free detectors that can represent valid candidates for detection systems for future spallation neutron sources such as the *European Spallation Source* (ESS [3]). In the case of ESS, besides the need for replacing ^{3}He, it is essential to develop high-rate neutron detectors that can fully exploit the increase of neutron flux of ESS relative to present neutron sources. Among the possible candidates, *Gas Electron Multiplier* (GEM [4]) based detectors offer good spatial resolution (from 80 μm up to few mm) and timing properties (few ns), excellent rate capability (MHz/mm^2), radiation hardness and the possibility to cover large areas [5,6]. GEM detectors properly modified to detect neutral particles [7–13] have been already used for neutron beam measurements. This paper describes the first neutron diffraction measurement recorded by the GEM-based detector described in ref. [12] and compares its performances with the standard ^{3}He-based detection system. This measurement took place on the INES instrument at the ISIS neutron spallation source.

Experimental set-up. –

The GEM detector. Figure 1(a) shows the detector installed inside the INES blockhouse.

The detector used in this measurement is a triple GEM equipped with an aluminium cathode coated by 1 μm of natural boron carbide (B_4C). The detector gaps (Drift, Transfer 1, Transfer 2 and Induction) —*i.e.* the spaces between the three GEM foils, the cathode and the

(a) E-mail: croci@ifp.cnr.it

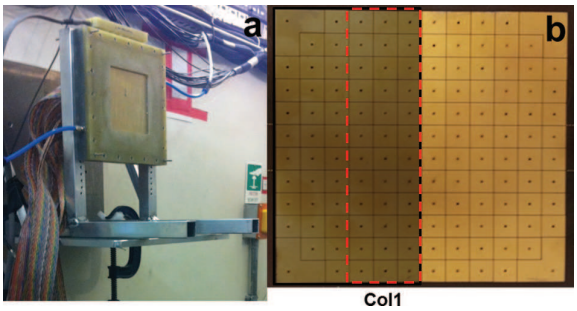

Fig. 1: (Colour on-line) (a) The GEM detector installed in the INES blockhouse; (b) picture of the padded read-out anode; the active area used in the measurement (shaded) as well as only three columns of pads (Col1 —dashed rectangle) are shown (see text for details).

anode— were, respectively, 13 mm, 2 mm, 3 mm and 1 mm wide. The following electrical configuration was applied to the GEM: $E_{\rm d}$ (drift field) = 0.69 kV/cm, ET_1 (Transfer 1 field) = 1.5 kV/cm, ET_2 (Transfer 2 field) = 2 kV/cm, $E_{\rm Ind}$ (induction field) = 5 kV/cm and $V_{\rm GEM}$ (sum of the voltages on the three GEMs) = 870 V. This configuration corresponds to an effective gas gain of 100. This device is equipped with a padded anode (whose substrate is made of fiberglass which is few mm thick) composed by 132 $8 \times 8\,{\rm mm}^2$ pads (made of gold-plated few microns thick copper) plus 4 L-shaped angular pads with an area of 192 $\rm mm^2$. The signal of each L-shaped pad is shortened with the signal coming from 2 adjacent pads in such a way that the resulting total number of channels is 128. Only half of the anode (64 channels corresponding to 68 pads —shaded area in fig. 1(b)) was read out and measurements were performed either considering the 64 channels all together or only 36 pads (dashed rectangle in fig. 1(b) - Col1). The GEM was positioned at 90° with respect to the beam and it was flushed with an Ar/CO_2 70%/30% gas mixture.

The electronic set-up. The front-end chips used to read out the pads are of the CARIOCA [14] type. The CARIOCAs were positioned on the back of the anode and are digital, self-triggered chips. The LVDS signals generated by four CARIOCAs were routed to a user-designed FPGA board that formed the interface between the front-end electronics and the standard ISIS Data Acquisition Electronics (DAE), known as DAE2. Data from the CARIOCAs were first buffered inside the FPGA, using an individual buffer per GEM pad, so that the interface electronics did not introduce any additional dead time. When the FPGA found data in one of the buffers, the position of the corresponding GEM pad that generated the signal was sent to the DAE for histogramming. The DAE performed the time stamping of these events and incremented the corresponding bin in the ToF histogram associated with this GEM pad, thereby creating the diffractograms that were recorded.

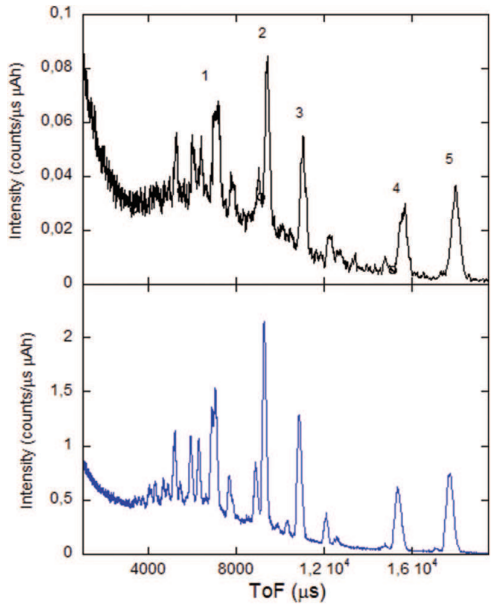

Fig. 2: (Colour on-line) Top: ToF diffractogram recorded by the GEM from a bronze sample; the total measurement time is 18 h; representative peaks are labelled for reference to table 1. Bottom: the same measurement but taken by two ^{3}He detectors from the INES beamline. Broadening of peak 1 is not due to detectors feature but it is intrinsic to the sample.

The INES beamline. INES [15] is a neutron *Time-of-Flight* (ToF) diffractometer at the ISIS neutron source. The pulsed nature of the ISIS source makes it ideal to exploit the possibility offered by the ToF technique. INES exploits thermal neutrons with wavelength between 0.17 Å and 3.24 Å with a $\Delta d/d$ up to 0.002. INES is equipped with 144 high-pressure (20 bar), squashed ^{3}He tubes (frontal width of 12.5 mm) as neutron detectors, each spanning an angle of about 1° in the horizontal plane. Such detectors are credited with an efficiency of about 60% to 70% for neutrons in the thermal energy range. Two of such ^{3}He detectors (positioned at 90° with respect to the neutron beam, symmetrically to the GEM) were taken as a reference for the present tests. As a scattering sample we used a 5 mm deep, 20 mm × 50 mm surface bronze slab.

Results and discussion. – In fig. 2, top panel, a diffractogram obtained by the GEM detector is shown. The lower panel shows the result of the same measurement recorded with two standard INES ^{3}He detectors (the signals coming from the two detectors are summed). A number of Bragg peaks from the bronze (copper) phase are visible. In table 1 a comparison of the performances of the two detector systems relatively to the current measurement is presented. All features of the data are correctly reproduced by the GEM detector.

For sake of simplicity, we summarize the following three facts:

a) The total count rate of the 68 GEM pads used in the measurement is about 7% the count rate of the two ^{3}He

Table 1: Comparison between GEM and ^{3}He tubes in terms of FWHM and S/B for the peaks labelled in fig. 2 (top panel). The errors associated to the fitting procedure are reported.

Peak number	1	2	3
ToF - GEM (μs)	7076 ± 6	9404 ± 3	11039 ± 4
FWHM - GEM (μs)	459 ± 114	240 ± 12	322 ± 18
S/B - GEM	1.1 ± 0.1	1.6 ± 0.2	2.3 ± 0.4
ToF - ^{3}He (μs)	6690 ± 20	9277 ± 1	10877 ± 1
FWHM - ^{3}He (μs)	325 ± 20	195 ± 4	231 ± 5
S/B - ^{3}He	1.2 ± 0.1	2.3 ± 0.1	2.8 ± 0.1
Peak number	4	5	
ToF - GEM (μs)	15603 ± 7	17994 ± 5	
FWHM - GEM (μs)	446 ± 48	435 ± 16	
S/B - GEM	4.9 ± 1.5	9 ± 3	
ToF - ^{3}He (μs)	15381 ± 2	17746 ± 3	
FWHM - ^{3}He (μs)	336 ± 6	378 ± 8	
S/B - ^{3}He	5.3 ± 0.4	12 ± 1	

detectors (9% in the case of the vanadium run), but with a different Signal-to-Background (S/B) ratio. These values are compatible with what was estimated from a simple calculation.

b) The FWHM of the diffraction peaks recorded with GEM is larger than that of the two ^{3}He detectors. Here we neglect the intrinsic broadening of the peaks since we are only interested in the effect of the detectors: in the present set-up, in order to optimise the count rate, all the 68 pads connected to the ISIS DAE were summed. This means that the full sensible area used in the measurement shown in fig. 2 spanned about 2.6° (compared to about 1° for the two adjacent ^{3}He tubes), thus causing a loss of angular resolution compared to the two INES detectors.

Conclusions and hints for future developments. – The results obtained in this paper show the possibility for GEM detectors equipped with borated cathodes to obtain good neutron diffraction data with the ToF technique. The detector proved to be fully compatible with the standard ToF DAE in use at ISIS. These results have a comparable quality with standard ^{3}He detectors, but GEMs need further optimisation to be really competitive with other detection systmes in such an application. The present authors envisage three areas of optimisation:

a) *Efficiency*. The overall efficiency to thermal neutrons of the present GEM is of the order of 1% for thermal neutrons, *i.e.* 60 to 70 times lower than common high-pressure ^{3}He tubes in the same energy range. The proposed way to improve the efficiency are the *3-D cathodes*, *i.e.* borated cathodes characterised by a three-dimensional configuration made to optimise the mean free path of both neutrons and reaction products into the converter material. Examples of 3-D cathodes are, for instance, presented in refs. [16,17]. Integration of 3-D cathodes with the present GEM set-up will be the subject of a future publication.

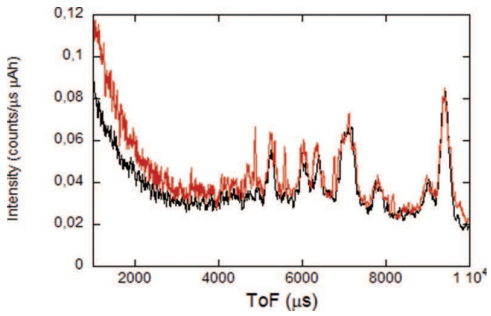

Fig. 3: (Colour on-line) zoom (in the region up to 10000 μs) of ToF diffractograms taken by the GEM detector from the mentioned sample with (black line) and without (red line) a boron-enriched plastic mask positioned on the detector structure. A sensible reduction of the background is especially visible in the shorter-times region.

b) *S/B ratio*. In the present experiment, the S/B ratio for the GEM was lower than for the ^{3}He tubes by approximately a factor 2. A likely source of background is the (H-atoms–rich) plastic structure of the GEM itself. A quick measurement performed with the same detector covered with a rough mask cut in boron-enriched plastic showed a sensible reduction of the background, especially at lower ToF, following a typical trend of neutron-induced background (fig. 3). We expect that proper design of boron carbide or cadmium masks will greatly improve the S/B ratio.

c) *Resolution*. As mentioned in the previous section, in order to optimise the count rate in fig. 2 all the 68 pads connected to the ISIS DAE were summed together, with consequent loss of angular resolution compared to the INES detectors. This effect can be reduced envisaging the possibility of summing single columns of pads, thus lowering the angular extension of the sensible area associated to a ToF channel. Padding makes the GEMs to be intrinsically position-sensitive detectors: this allows a better *focusing* of ToF data for larger-area detectors. As an example, when summing the signals from 36 pads only, arranged in three columns (thus reducing the angular span of the sensitive area —see fig. 1 - Col1), the FWHM of peak No. 4 and 5 is reduced by about 10%. For other, less intense peaks, due to the relatively low count rate, the resolution of single peaks is limited by the effect of counting statistics, as it occurs while summing a single column of pads with the present setup. A study in depth of the dependence of resolution on the shape and span of the detector requires further tests with a suitable collimation (for instance obtained with gadolinium-coated slits), and will be the subject of future work. An increased detector efficiency will also give the possibility of summing single-pad columns, thus improving the spatial resolution.

This test proves that GEM detectors can be used for neutron diffraction measurement and paves the way for their use at future neutron spallation sources.

Paper III

PUBLISHED BY IOP PUBLISHING FOR SISSA MEDIALAB

RECEIVED: *May 18, 2015*
REVISED: *August 25, 2015*
ACCEPTED: *September 7, 2015*
PUBLISHED: *October 5, 2015*

A GEM-based thermal neutron detector for high counting rate applications

E. Perelli Cippo,[a,1] **G. Croci,**[b,a,c] **A. Muraro,**[a] **A. Menelle,**[d] **G. Albani,**[b] **M. Cavenago,**[e] **C. Cazzaniga,**[b] **G. Claps,**[f] **G. Grosso,**[a] **F. Murtas,**[f] **M. Rebai,**[b] **M. Tardocchi**[a] **and G. Gorini**[c]

[a] *Istituto di Fisica del Plasma "P. Caldirola", Associazione EURATOM-ENEA/CNR, Milano, Italy*
[b] *Dipartimento di Fisica "G. Occhialini", Università degli Studi di Milano-Bicocca, Milano, Italy*
[c] *INFN – Sezione di Milano-Bicocca, Piazza della Scienza 3, 20125 Milano, Italy*
[d] *Laboratoire Léon Brillouin, CEA-Saclay, 91191 Gif sur Yvette Cedex France*
[e] *INFN Laboratori Nazionali di Legnaro, Viale dell'Università 2, 35020 Legnaro, Italy*
[f] *INFN – Laboratori Nazionali di Frascati, Via Fermi 40, 00044 Frascati, Italy*

E-mail: perelli@ifp.cnr.it

ABSTRACT: Among other neutron detector systems proposed as a possible substitute for ^{3}He tubes, GEM-based ones have shown appealing characteristics, when coupled with suitable neutron-converter cathodes. In this paper, we present the results of a GEM-based neutron detector in a high-flux environment (the ORPHÉE reactor in Saclay), especially in terms of maximum rate capability and linearity. Recorded data show that the detector can manage neutron counting rates in the order of 50×10^6 counts/sec cm^2 while maintaining a reasonable linearity and with no sign of instability.

KEYWORDS: Micropattern gaseous detectors (MSGC, GEM, THGEM, RETHGEM, MHSP, MICROPIC, MICROMEGAS, InGrid, etc); Neutron detectors (cold, thermal, fast neutrons)

[1] Corresponding author.

doi:10.1088/1748-0221/10/10/P10003

2015 JINST 10 P10003

Contents

1 Introduction **1**

2 Experimental setup **2**
2.1 The G3-2 station 2
2.2 The GEM-based detector 2

3 Results and discussion **3**
3.1 Measurement of the thermal neutron 2D map 3
3.2 Maximum rate capability and linearity test 3
3.3 HV-scan and threshold-scan 4
3.4 Counting stability 5

4 Conclusions **7**

2015 JINST 10 P10003

1 Introduction

The R&D activity about neutron detectors has had a sensible rise in recent times due to the somehow sudden shortage of ^{3}He. The search for substitutes of ^{3}He tubes as thermal neutron detectors is paramount for the implementation of present and especially next generation neutron sources such as the European Spallation Source (ESS [1]). In order to make a full use of the intense ESS neutron beam, an optimised detector should have high-rate capability and (especially for SANS and NR instruments) cover a large area. GEM (Gas Electron Multiplier) -based detectors fulfil such requirements: in particular, they have proven very high-rate capabilities for X-rays (up to 1 MHz/mm^2 [2], coverage of up to 1 m^2 area and spatial resolution better than 0.5 mm [3–5]. GEMs are intrinsically charged-particles detectors for tracking and triggering but if coupled to a proper converter can be used to detect neutral particles such as photons [6–9] and neutrons [10–14].

GEMs can be made sensitive to thermal neutrons by coupling with a neutron converter cathode (for instance enriched in ^{10}B) able to let the neutrons generate electrically charged particles (for instance Alpha particles or Lithium ions) to be revealed by the GEM [15]. Present R&D activity is concentrated on the optimisation of such cathodes (the present authors group them under the common name of 3-D cathodes), of which many examples exist [20, 21]. Other approaches followed for the development of gas counters as neutron detectors are, for instance, optimisation for fast neutrons [23], or the CASCADE detectors [24]. All of these detectors present some advantages and disadvantages, depending on the expected applications and, consequently, the different characteristics that are either improved (for instance efficiency, resolution etc.) or, on the opposite, neglected. Thus, not a single kind of detector can be considered as the "perfect" substitute for ^{3}He tubes.

The present authors are involved in the development of a series of detectors, the envisaged application of which is low-angle scattering and diffraction in the future spallation source ESS, with

typical neutron wavelength range 1 to 12 Å (thus extending from "thermal" to "cold" neutrons) and high neutron flux. In this paper, we present the results obtained with a triple-GEM detector with a natural B_4C neutron converter cathode tested at the G3-2 irradiation station of the 14 MW ORPHÉE reactor in Saclay [16]. The G3-2 beamline provides a flux of 7.88×10^8 n/s cm^2, and it thus constitutes a very valuable test bed for counting rate capability, radiation hardness and other detector properties requiring a high neutron flux. Moreover, the G3-2 flux distribution, peaked at about 3.5 meV energy, is reasonably representative of the thermal/cold neutron field expected at ESS. The presented results show that the GEM-based detector can achieve counting rates in the order of 50 MHz/cm^2 with a reasonable loss of linearity. Moreover, the used GEM electronics has worked continuously in the neutron beam for about 9 hours without appreciable loss of performances.

2 Experimental setup

2.1 The G3-2 station

The G3-2 irradiation station is located at about 20 m from the ORPHÉE reactor core; it provides a white neutron beam of peak energy of about 3.5 meV with a 25×50 mm^2 spot and 0.4° divergence. The expected thermal neutron flux at the measurement position is $\Phi = 7.88 \times 10^8$ n/cm^{2}s [22].

2.2 The GEM-based detector

The detector used in the present experiment was a triple-GEM based one, equipped with a 400 μm Al cathode covered with a 1 μm thick boron carbide layer. Such a cathode/converter exploits the ^{10}B(n, α)^{7}Li reaction in order to convert thermal neutrons into charged particle to be detected through the GEM multiplication stages. The choice of the converter layer thickness is determined by two competing effects, and namely the probability of neutron capture from ^{10}B nuclei (higher for higher thicknesses) and probability of escape of reaction products from the layer (lower for higher thickness). In fact, only reaction products emerging from the layer into the gas may be detected. Both previous tests and analytical calculations have shown that 1 μm is very close to the optimum thickness [25]. The relevant parameters of such a detector [17] were:

a) GEM gaps (*Drift, Transfer* 1, *Transfer* 2 and *Induction*): 13 mm, 2 mm, 3 mm and 1 mm, respectively. The choice of a triple-GEM configuration is linked to discharge probability: a triple-GEM has a discharge probability that is many order of magnitude lower than a single one with the same total gain. Thus the triple-GEM represents a safer and more robust option for a detector that has to work at high rates for long measurement times [26].;

b) padded anode composed by 124 8×8 mm^2 pads plus 4 L-shaped angular pads for a total area of 192 mm^2 on 128 independent channels (see figure 1, left panel).

c) read-out performed through CARIOCA chips [18] and a FPGA motherboard with real-time recording capability [17]. The "working point", i.e. total applied voltage (shared by the three GEM foils) is nominally 870 V (see further for details). Previous measurements had shown, for such an applied voltage and the Ar 70%/CO_2 30% gas mixture used in this setup, a gain G = 100 [13].

2015 JINST 10 P10003

The conversion efficiency of the borated cathode may be written as:

$$1 - e^{-\Sigma z_{\text{eff}}} \tag{2.1}$$

where Σ is the macroscopic cross-section for neutron capture in ^{10}B nuclei and z_{eff} is the effective thickness of such nuclei into the converter material. Considering the cross-section of the neutron capture reaction in boron and the mentioned parameters, a 5% conversion efficiency estimated for a cold/thermal beam as the one of G3-2. The number of detected counts in the detector depends of course on other parameters, such as for instance the settings of the electronic read-out; however, taking the previous figure as a rough indication of the overall efficiency of the detector, thus the expected count rate with the G3-2 station flux was estimated to be of 39.4 MHz/cm^2.

3 Results and discussion

3.1 Measurement of the thermal neutron 2D map

The detector operated with the electrical parameters described in the previous paragraph was exposed to the neutron beam and figure 1 shows the reconstruction of the 2D beam image using 128 pads with 8×8 mm^2 area. The shape of the beam is rectangular as expected from the shape of the G3-2 beam-line collimator [22].

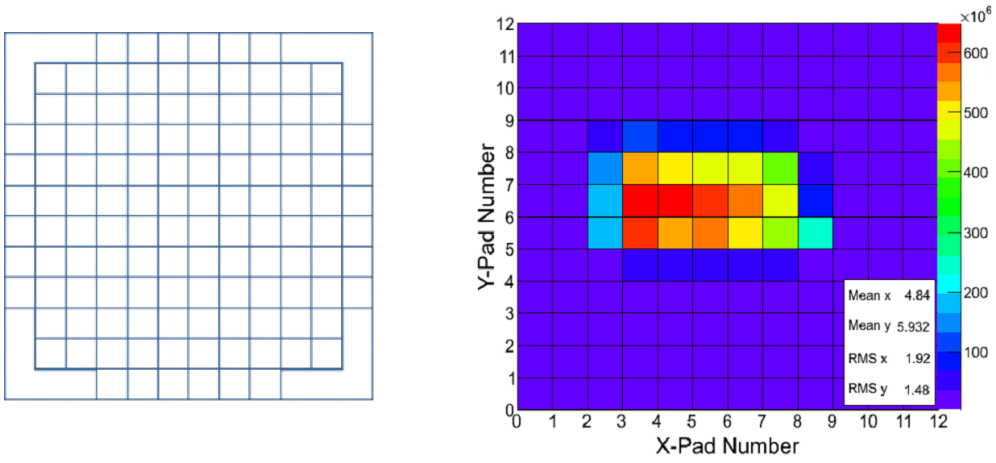

Figure 1. Left panel: a scheme of the padded anode of the GEM used in these measurements. The square pads dimensions are 8×8 mm^2. Right panel: 2D Neutron Map reconstructed with the GEM.

3.2 Maximum rate capability and linearity test

The GEM counting rate capability as well as its linearity were compared with a fission chamber (FC) detector (a well-proven neutron flux monitor) constituted of a 4 mm diameter gas proportional counter with a 2 cm section internally coated with a ^{235}U deposit. The FC was positioned in front of the GEM detector and simultaneous measurements were taken. A series of 1.8 mm thick polyethylene slabs were placed in the neutron beam in order to attenuate, via multiple scattering,

2015 JINST 10 P10003

the flux impinging on both detectors. As a rule of thumb, such polyethylene slabs are credited to reduce the G3-2 neutron flux of about a factor 2 for every mm of thickness. For sake of clarity, we have to underline that a precise estimation of the flux reduction through moderation typically would require long and complex simulations; however, for the present purposes, it is not necessary to exactly quantify the flux on the detectors, provided that the flux investing the two systems is the same. For that reason, the data presented in figure 2 are just labelled with the total thickness of plastic interposed.

Due to the behaviour of the electronic system, our detector setup can be modelled using a *non-paralizable* model. We consider the FC as the reference detector so that its measured interaction rate is strictly linked to the real interaction rate. The non-paralizable model leads to the following relation between GEM and the real counting rates:

$$N_{\mathrm{Real}} - N_{\mathrm{GEM}} = \tau N_{\mathrm{GEM}} N_{\mathrm{Real}} \tag{3.1}$$

where N_{Real} and N_{GEM} are the true and GEM detector count rates and τ is the saturation time.

Since the FC is taken as reference detector we can say that $N_{\mathrm{Real}} = aN_{\mathrm{FC}}$ and we rewrite the saturation time τ as b/a, where b and a are parameters that can be determined through a fitting procedure.

By applying the described changes to formula (2.1) we can obtain the saturation formula that links the GEM counting rate to the FC counting rate:

$$N_{\mathrm{GEM}} = a \quad N_{\mathrm{FC}}/(1 + bN_{\mathrm{FC}}) \tag{3.2}$$

where N_{FC} and N_{GEM} are the reference detector and GEM detector count rates. Assuming the reference detector is perfectly linear in its whole dynamic range, the b/a ratio assumes as expected the physical meaning of the saturation time of the (non-paralizable) system constituted by the GEM detector and its front-end electronics.

Fitting of the data in figure 2 with formula (3.1) gives the values $a = 3.519$ MHz/pad and $b = 0.028$, thus resulting in an estimated saturation time τ of about 8 ns/pad. The GEM system non-linearity measured in correspondence of the dashed-line in figure 2 (that is when the beam is attenuated by one polyethylene slab) is about 9% while this values increases up to 20% if the full beam (no absorber) is considered.

The value of the GEM counting rate per pad where the non-linearity starts to appear is around 10MHz/pad which represents the limit value for the CARIOCA linearity [17].

3.3 HV-scan and threshold-scan

The rate achieved in full beam conditions with the GEM detector with the present settings, and in particular with the present applied voltage, was of about 40 MHz/cm^2. However, the overall count rate depends upon a) the gas gain of the detector, and thus the applied voltage, and b) the *low level discrimination* (LLD) threshold applied. A suitable LLD is in fact necessary to cut thermal electronic noise. Previous measurements [15] had shown an ideal applied HV ("working point") of 870 V divided on the three GEM foils: tests showed that at such working point the sensitivity of the detector to the (ever present) gamma-ray background is negligible [13].

2015 JINST 10 P10003

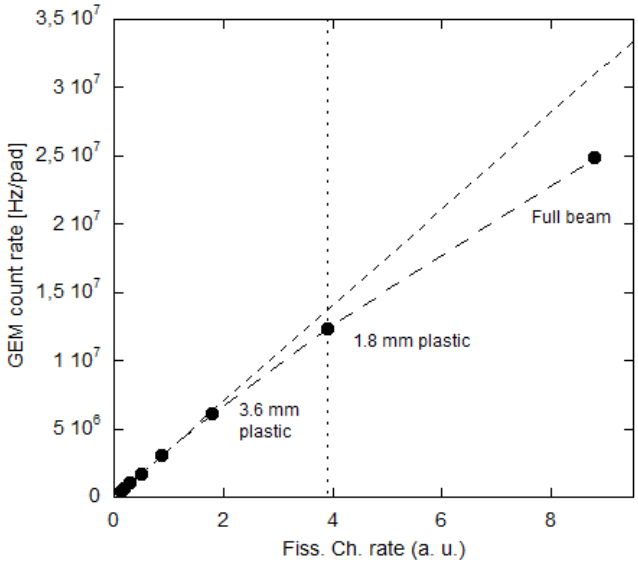

Figure 2. GEM counting rate per pad vs Fission chamber counting rate for different thickness of plastic absorbers interposed in the beam before both detectors.

The present digital electronics does not allow to obtain a pulse eight spectrum (in order to precisely determine the exact relationship between LLD threshold and energy deposit in the gas); however, it had been observed [15] that a 900 mV LLD threshold is high enough to reject most of the noise, even if it is usually set higher to be on the safe side. So called "HV-scan" and "threshold-scan" were performed in order to study the dependence of count rate upon the previous parameters and to check the maximum realistic count rates achievable with the present detector setup. Figure 3 shows such measurements in the left and right panel, respectively. In this case the counting rate was normalized to the pad dimensions that are $8 \times 8\,\mathrm{mm}^2$. As already seen from previous measurements, it may be noted that the counting rate dependence *vs* applied HV shows a sort of plateau for $V > 850\,\mathrm{V}$, corresponding to a rate of about $40\,\mathrm{MHz/cm}^2$, in good agreement with the estimated value. The rate may be even raised while lowering the LLD threshold down to 900 mV. The HV-scan and threshold-scan suggest that, in appropriate conditions, the thermal neutron count rate may be as high as about $50\,\mathrm{MHz/cm}^2$, thus overtaking the theoretical upper limit of linearity of the CARIOCA chips.

3.4 Counting stability

Among other aspects, counting rate stability is a major requirement for high-rate neutron detectors, expected to work properly for the sake of many-hours long experimental runs. Most concerns about detector stability involve the detector itself (possibility of discharges between GEM foils) and especially the CARIOCA chips board. We have to note that, due to the configuration of the detector, with the chips right behind the padded anode, the chips themselves were irradiated by the neutron beam, thus enhancing the possibility of the rise of so-called "soft-errors" [19]. To check the detector stability, the integrated number of events detected in 0.4 seconds intervals was recorded

2015 JINST 10 P10003

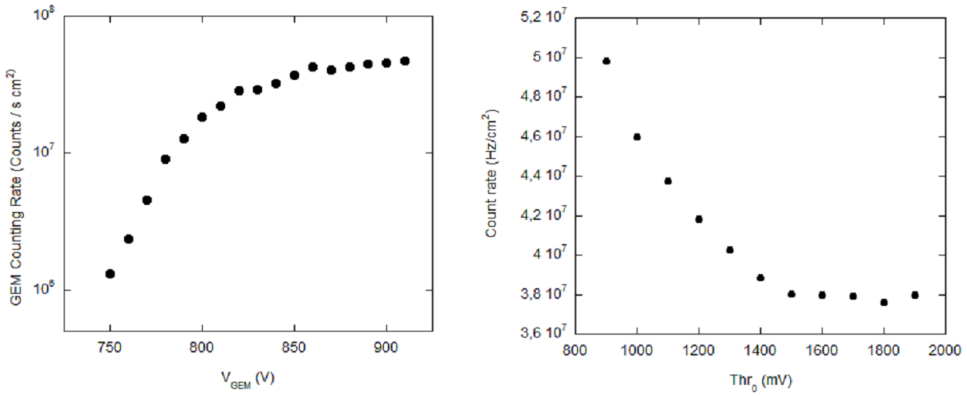

Figure 3. Left: HV-scan measurement. The scan was performed with a LLD threshold of 1300 mV, in order to avoid any possible signal from unwanted gamma-rays. Right: threshold-scan measurement. The quantity on the X axis is the common threshold applied to the CARIOCA chips. In both panels, the count rate is normalized to a conventional $8 \times 8\,\mathrm{mm}^2$ detector surface.

for a 9-hours long run (see figure 4), and the distribution of the recorded values analysed. A mean and median value of 3.6604×10^7 counts/s and 3.6603×10^7 counts/s, respectively as well as a standard deviation of 1.4×10^5 counts/s were measured. Assuming the latter value as an indication of the detector count rate stability, we can conclude that, in the present, very high-flux conditions, the detector was stable within a 0.5% level.

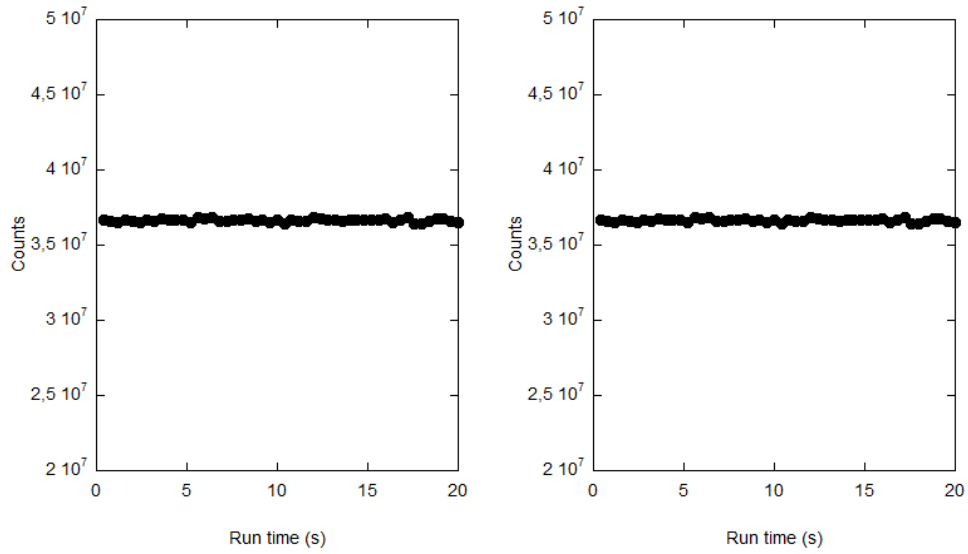

Figure 4. Integrated counts in a series of 0.4 s time intervals for a 9-hours long run. Left panel: the first 20 seconds of the measurement. Right panel: the last 20 seconds.

2015 JINST 10 P10003

4 Conclusions

In this paper, results from tests on a GEM-based thermal neutron detector have been presented. The tests were especially devoted to the investigation of the possibilities offered by GEMs in terms of count rate. High count rate, in fact, is a paramount for the detectors envisaged in next-generation neutron sources like ESS. The application of the GEM detector to the realistic conditions (very high neutron flux) available at ORPHÉE has shown that the GEM-based detector coupled with a boron cathode/converter may easily reach count rates of the order of 50 MHz/cm^2, with good linearity. The count rate appears to be limited by the associated read-out electronics only. The CARIOCA chips used in the present setup are in fact characterised by a range of linearity up to about 10 MHz per channel. New chips based on 180 nm CMOS technology are being developed in order to overcome this problem. Moreover, the detector offers the additional advantage of a good long-term (several hours) stability in a harsh environment.

The present results add up to the good characteristics already shown by the detector in terms of spatial and Q resolution when applied as a neutron diffraction detector [14], resolution that may also be further improved by mean of a proper focussing procedure.

Acknowledgments

The authors warmly acknowledge Dr. C. Alba-Simionesco of Laboratoire Léon Brillouin in providing the neutron research facilities used in this work. This work was set up in collaboration and financial support of INFN Group 5 (Technology Research).

References

[1] European Spallation Source, http://europeanspallationsource.se/.

[2] M. Alfonsi et al., *Activity of CERN and LNF groups on large area GEM detectors*, *Nucl. Instrum. Meth.* **A 617** (2010) 151.

[3] S. Duarte Pinto et al., *Progress on large area GEMs*, 2009 *JINST* **4** P12009.

[4] F. Sauli, *GEM: A new concept for electron amplification in gas detectors*, *Nucl. Instrum. Meth.* **A 386** (1997) 531.

[5] M. Villa et al., *Progress on large area GEMs*, *Nucl. Instrum. Meth.* **A 628** (2011) 182 [arXiv:1007.1131].

[6] M. Alexeev et al., *The quest for a third generation of gaseous photon detectors for Cherenkov imaging counters*, *Nucl. Instrum. Meth.* **A 610** (2009) 174.

[7] M. Alexeev et al., *THGEM based photon detector for Cherenkov imaging applications*, *Nucl. Instrum. Meth.* **A 617** (2010) 396.

[8] M. Alexeev et al., *Development of THGEM-based photon detectors for Cherenkov Imaging Counters*, 2010 *JINST* **5** P03009.

[9] M. Alexeev et al., *Micropattern gaseous photon detectors for Cherenkov imaging counters*, *Nucl. Instrum. Meth.* **A 623** (2010) 129.

[10] G. Croci et al., *nGEM neutron diagnostic concept for high power deuterium beams*, 2012 *JINST* **7** C03010.

2015 JINST 10 P10003

Paper IV

Jinst

Published by IOP Publishing for Sissa Medialab

Received: *January 12, 2016*
Accepted: *February 14, 2016*
Published: *March 16, 2016*

International workshop on Imaging
7–10 September 2015
Varenna, Italy

Neutron radiography as a non-destructive method for diagnosing neutron converters for advanced thermal neutron detectors

A. Muraro,[a,1] **G. Albani,**[b] **E. Perelli Cippo,**[a] **G.Croci,**[b] **G. Angella,**[c] **J. Birch,**[d] **C. Cazzaniga,**[e] **R. Caniello,**[a] **F. Dell'Era,**[a] **F. Ghezzi,**[a] **G. Grosso,**[a] **R. Hall-Wilton,**[f] **C. Höglund,**[d] **L. Hultman,**[d] **S. Schimdt,**[d] **L. Robinson,**[d] **M. Rebai,**[b] **G. Salvato,**[g] **D. Tresoldi,**[g] **C. Vasi**[g] **and M. Tardocchi**[a]

[a] *Istituto di Fisica del Plasma "P. Caldirola", IFP-CNR, Via Cozzi 53, Milan, Italy*
[b] *Dipartimento di Fisica, Università di Milano Bicocca, Piazza della Scienza 3, Milan, Italy*
[c] *IENI-CNR, Via Cozzi 53, Milan, Italy*
[d] *Dept. of Physics, Chemistry and Biology (IFM), Thin Film Physics Division, Linköping University, SE-581 83 Linköping, Sweden*
[e] *ISIS — Rutherford Appleton Laboratory — STFC, Didcot, United Kingdom*
[f] *European Spallation Source ESS-ERIC, Tunavägen 24, 223 63 Lund, Sweden*
[g] *Istituto Processi Chimico-Fisici, IPCF-CNR, Viale Ferdinando Stagno d'Alcontres 37, Messina, Italy*

E-mail: muraro@ifp.cnr.it

Abstract: Due to the well-known problem of ^{3}He shortage, a series of different thermal neutron detectors alternative to helium tubes are being developed, with the goal to find valid candidates for detection systems for the future spallation neutron sources such as the *European Spallation Source* (ESS). A possible ^{3}He-free detector candidate is a charged particle detector equipped with a three dimensional neutron converter cathode (3D-C). The 3D-C currently under development is composed by a series of alumina (Al_2O_3) lamellas coated by 1 μm of ^{10}B enriched boron carbide (B_4C). In order to obtain a good characterization in terms of detector efficiency and uniformity it is crucial to know the thickness, the uniformity and the atomic composition of the B_4C neutron converter coating. In this work a non-destructive technique for the characterization of the lamellas that will compose the 3D-C was performed using neutron radiography. The results of these measurements show that the lamellas that will be used have coating uniformity suitable for detector applications. This technique (compared with SEM, EDX, ERDA, XPS) has the advantage of being global (i.e. non point-like) and non-destructive, thus it is suitable as a check method for mass production of the 3D-C elements.

Keywords: Inspection with neutrons; Neutron radiography; Image filtering; Data processing methods

[1] Corresponding author.

doi:10.1088/1748-0221/11/03/C03033

2016 JINST 11 C03033

Contents

1 Introduction **1**

2 Sample description **2**

3 Preliminary characterization techniques **2**
- 3.1 SEM 3
- 3.2 EDX, ERDA and XPS analysis 3
- 3.3 Neutron radiography 4
- 3.4 Experimental setup 5
- 3.5 Data analysis 7
- 3.6 Results of the measurements with the lamellas perpendicular to the neutron beam 9
- 3.7 Results of the measurements with the lamella inclined by different angles 11
- 3.8 Measurement of lamellas with different boron thickness 11
- 3.9 Results validation 11

4 Conclusions and future work **12**

2016 JINST 11 C03033

1 Introduction

Due to the well-known problem of ^{3}He shortage, a series of different thermal neutron detectors alternative to helium tubes are being developed, with the goal to find valid candidates for detection systems for the future spallation neutron sources such as the *European Spallation Source* (ESS [1]). Given the expected high neutron flux at the ESS, compared with present spallation sources, there is not only a need for replacing ^{3}He, but also to develop high-rate neutron detectors. An intense R&D phase is ongoing in order to find high performing ^{3}He-free detectors which can meet the requirements imposed by ESS. One possibility is to equip charged particle detectors (such as GEM [2, 3] detectors) with three-dimensional neutron converter cathodes (3D-C). The 3D-C currently under development is composed by a series of alumina (Al_2O_3) lamellas coated by 1 μm of boron-10 enriched boron carbide ($^{10}B_4C$). A thermal neutron reaction in ^{10}B produces the detectable charged particles ^{7}Li and ^{4}He. In order to obtain a well-known characterization in terms of detector efficiency and uniformity is crucial to know the thickness, the uniformity and the atomic composition of the $^{10}B_4C$ neutron converter coatings.

While the determination of such parameters is relatively straightforward for standard two-dimensional neutron converters, this may not be the case for the complex 3D-C. In fact, given the huge number of lamellas required for the composition of the 3D-C and the relatively high cost for each lamella, it is essential to find a non-destructive method for the characterization of the $^{10}B_4C$ coatings.

In this work a series of methods for the characterization of the lamellas are presented: first of all a series of destructive tests were carried out on a limited number of samples. The techniques

used in these tests are the Scanning Electron Microscopy (SEM), the Energy Dispersive X-ray Spectroscopy (EDX), the Elastic Recoil Detection Analysis (ERDA) and the X-ray photoelectron spectroscopy (XPS). Finally a non-destructive technique for the characterization of all the lamellas that will composed the 3D-C was performed using neutron radiography.

The SEM and EDX measurements were made in the electron microscopy laboratory of the research Institute IENI-CNR [3], the ERDA analysis was performed in the Linköping University [4] and, the XPS analysis was performed in the Institute IFP-CNR [5] while the neutron radiography measurements have been performed at the *ROTAX* beamline at ISIS [6], making use of the new radiography-tomography system being developed for the next *IMAT* beamline [7]. Data treatment considering the white-spectrum measurements is described and validated through the use of a standard reference sample.

2 Sample description

Figure 1 shows an Al_2O_3 lamella coated with 1 um of $^{10}B_4C$.

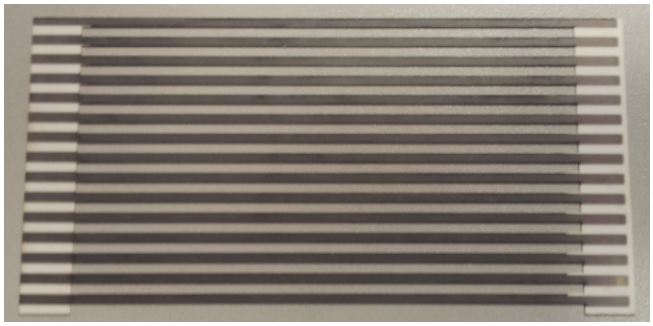

Figure 1. Coated Al_2O_3 lamella.

Each lamella has external dimensions of $120 \times 60 \times 0.25\,mm^3$ and is composed by 15 strips, each one with dimensions $100 \times 2 \times 0.25\,mm^3$. Each strip is coated on both sides with 1 μm of $^{10}B_4C$ that serves as neutron converter. $^{10}B_4C$ shows superior chemical, mechanical and electrical properties compared to pure ^{10}B. Excellent stability against neutron radiation has also been shown in [8]. The main disadvantage is the 20% lower ^{10}B concentration compared to pure ^{10}B. The coatings have been deposited using DC magnetron sputtering, as further described in [9]

The depositions were done in an industrial CC800/9 deposition system manufactured by CemeCon AG at the Linköping University in Sweden. After being cleaned in acetone followed by isopropanol in an ultrasonic bath, the alumina substrates were mounted onto a sample carousel which allows 2-axis planetary rotation and 2-sided deposition. In order to decrease the impurity level and to improve the adhesion of the coating, the lamellas where heated up to 400°C before and during the deposition process [9, 10]

3 Preliminary characterization techniques

The characterization of the lamellas proposed in this paper may give best results if some information on the deposited film are known with high precision; for the sake of this paper devoted to the

2016 JINST 11 C03033

technique development, important parameters like isotopic composition, thickness, mass density and presence of impurities have been measured and cross-checked with the techniques described in the following paragraphs.

3.1 SEM

The SEM analysis was performed with a high resolution SU70 microscope by Hitachi with Schottky electron source. This analysis gives a measurement of the coating thickness and, by repeating the measurement all along the strips length, one can obtain an estimation of the thickness uniformity. Figure 2 shows a 0.9 μm B_4C thick coating on the alumina substrate.

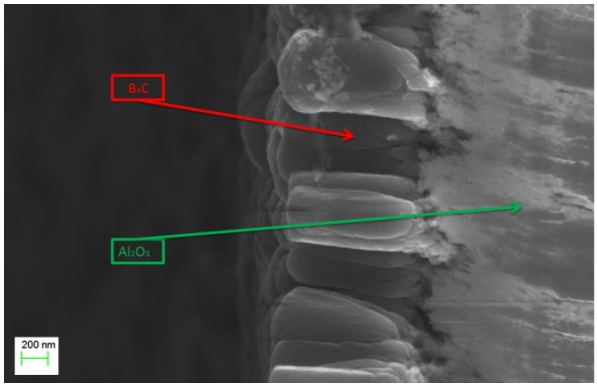

Figure 2. Result of the SEM analysis.

By repeating the measurements in different locations along the strips, it was noticed that the film thickness is not perfectly uniform. The values found lie between 0.85 μm (near the strips edges) and 0.95 μm (at the center of the lamellas): a value of 0.9 μm was taken for the successive calculations presented in this paper.

3.2 EDX, ERDA and XPS analysis

The EDS (Energy Dispersive X-Ray Spectroscopy) and the ERDA (Elastic Recoil Detection Analysis) analyses were performed in order to obtain an estimation of the impurities contained in the coating, while the XPS (X-Ray Photoelectron Spectroscopy) analysis has the scope to measure the variation of the atomic composition of the coating all along its thickness. These are standard material analysis techniques, and the detailed description of the instrumentation used to perform these analyses is beyond the scope of this paper and it will be presented in a future paper. Here we just mention that the results obtained with the different analyses are compatible (see table 1). The used techniques are intrinsically point-like, and this can easily explain small discrepancies between local values. However, the XPS analysis has shown that the atomic composition of the coating is constant all along its thickness. The averages of the found values are reported in table 1.

As one can see, not only B and C are found in the coating, but also O, Mg, Al and some heavier elements (Fe, Cr, Ni and Cu). The elemental composition found in these analyses is taken into account in the calculation of absorption coefficients for the successive non-destructive characterization method.

2016 JINST 11 C03033

Table 1. Average atomic composition found using the different analysis techniques mentioned in the paper. Values are in percentage. Typical errors associated with these estimations are in the order of a few percent. Small discrepancies between values are due to the point-like nature of the techniques. The presence of such impurities into the neutron-absorber coating is accounted for in the following calculations.

Isotopes	B	C	Fe	Cr	Ni	Cu	O	Mg	Al
EDS	73	20	4	1	1	1	/	/	/
TOF-ERDA	77	16	/	/	/	/	1	2	0.4
XPS	68	28	2	/	/	/	7	/	/

The combination of these techniques gives a complete characterization of the samples, but at the price of sectioning and sampling the lamella elements, thus making them unsuitable for further application. As a consequence, another approach must be followed in order to characterize all the samples that will compose the detector.

3.3 Neutron radiography

In order to characterize the boron carbide film deposited on all the lamellas, the neutron radiography technique was used. This is a non-invasive, non-destructive technique to obtain images of the inner parts of an object using a neutron beam to illuminate it. Neutrons transmitted through the sample are described by the following exponential law:

$$I(E) = I_0(E)e^{-\Sigma(\mathrm{E})z}$$

where $I_0(E)$ is the incoming neutron flux onto the sample, $I(E)$ is the attenuated flux after crossing the sample, z is the thickness and Σ is the total macroscopic cross section that is defined as a function of the atomic density ρ and the total neutron cross section σ of the elements which compose the sample of molecular weight PM:

$$\Sigma = \sigma\,(\mathrm{E})\,\frac{n}{V} = \sigma\,(\mathrm{E})\,\frac{\rho N_A}{PM}$$

where N_A is the Avogadro constant. For the characterization of the lamellas we were interested in the total amount of neutrons absorbed from the boron contained into the $^{10}\mathrm{B}_4\mathrm{C}$ coating. In fact, apart from the small fraction of neutrons absorbed or scattered from the nuclei of the impurities or of the alumina substrate, all the absorbed neutrons lead to the production of charged particles that can give a detectable signal in the charged particle detector equipped with the 3D-C.

In the analysis all the materials that compose the sample are taken into account, but the main contribution to the neutron absorption comes from the presence of the $^{10}\mathrm{B}$, which presents the greater cross section compared with all the other materials in the region of interest, as shown in figure 3.

The analysis for the characterization of the film uniformity is done by comparing the the expected transmitted radiation $\left(\frac{\tilde{I}}{\tilde{I}_0}\right)^{\text{expected}}$ with the measured one $\left(\frac{\tilde{I}}{\tilde{I}_0}\right)^{\text{measured}}$.

The value of the transmitted radiation is calculated by introducing the equivalent thickness t of the $\mathrm{B}_4\mathrm{C}$ film:

$$t = \frac{\rho_{B_4C} z_{B_4C}}{PM_{B_4C}}$$

2016 JINST 11 C03033

so that the expected transmitted radiation can be written as:

$$\left(\frac{\tilde{I}}{\tilde{I}_0}\right)^{\text{expected}} = \frac{\int_{E_{\min}}^{E_{\max}} I_0(E) e^{-\sigma(E) N_{\text{Av}} t^{\text{expected}}} dE}{\int_{E_{\min}}^{E_{\max}} I_0(E) dE}$$

with the expected equivalent thickness (t^{expected}) calculated using $\rho_{\text{B4C}} = 2.242\,\text{g/cm}^3$ $\rho_{\text{B4C}} = 2,242\,\text{g/cm}^3$ [2] and the value of $z_{\text{B4C}} = 0.9\,\mu\text{m}$ obtained from the SEM analysis. The measured transmitted radiation can be written as:

$$\left(\frac{\tilde{I}}{\tilde{I}_0}\right)^{\text{measured}} = \frac{\int_{E_{\min}}^{E_{\max}} I_0(E) e^{-\sigma(E) N_{\text{Av}} t^{\text{measured}}} dE}{\int_{E_{\min}}^{E_{\max}} I_0(E) dE}$$

Where t^{measured} is calculated by using the value of mass density obtained from the residuals evaluation after estimating the average of the neutrons absorbed by the lamella's strips ($\text{neutron}_{\text{abs}}$) (see par 3.3.2 for details) and the values of z and of the impurities concentration obtained in the SEM and in the EDX, ERDA and XPS analysis.

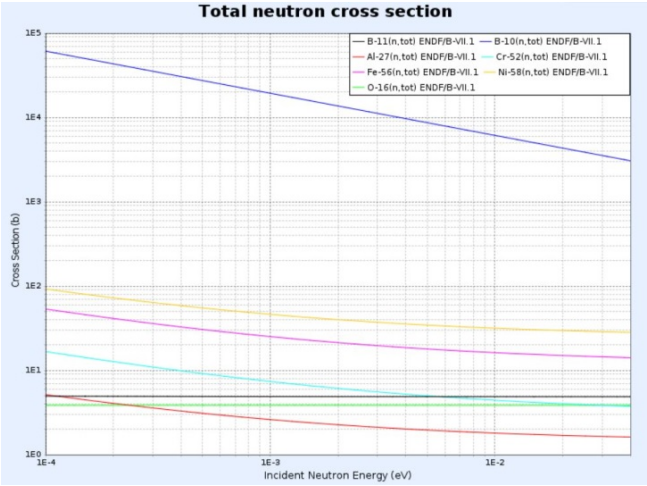

Figure 3. Total neutron cross section of the elements in the coating.

3.4 Experimental setup

The neutron radiography measurements have been performed at the *ROTAX* beamline [1] at ISIS, using the radiography-tomography system for the next *IMAT* [7] beamline at ISIS. Figure 4 shows a schematic of the experimental setup used for the characterization of the lamellas in the ROTAX beamline.

Neutrons transmitted through the sample strike a scintillator screen which converts the incoming neutrons into photons, the latter being detected, through a mirror, by a digital camera (CCD). The lamellas were positioned on a rotating sample holder, which permits to select the angle between the incoming neutron beam and the lamellas. Moreover, the neutron beam in the ROTAX beamline has

2016 JINST 11 C03033

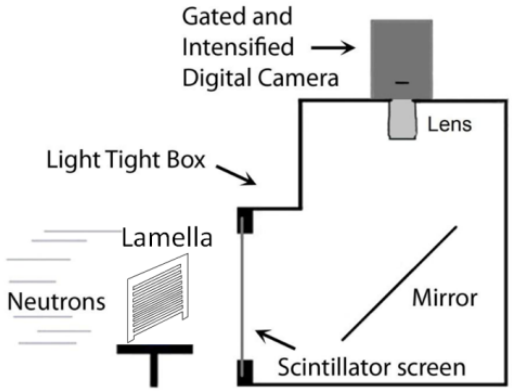

Figure 4. Schematic of the experimental setup.

dimensions of about $40 \times 35\,\mathrm{mm}^2$ therefore the rotating sample holder has been mounted on a x-y positioner, which allows to move and to enlighten all the lamella.

The neutron flux used for the irradiation had an energy spectrum cleaned of fast neutrons and gamma components thanks to an upstream t-zero chopper. This is a rotating structure that operates at the ISIS source frequency and is phased in such a way that the line of sight from the target to the sample is blocked when the proton beam hits the target. The details of operation of the chopper on the ROTAX beamline can be found in [14]. The resulting spectrum is shown in figure 5. The use of a gamma suppressing chopper is a common procedure at ISIS when transmission (i.e. *in the beam*) diagnostics are used, as in this case. In the present case, the scintillator coupled to the radiography system has a residual sensitivity to gamma rays: while this sensitivity is low (in the order of 10^{-6}) enough to make negligible the background due to activation inside the block-house and from the sample itself (see par. 3.5 for details), it may not be the case when a large flux of gammas is expected, as the one coming from the spallation target.

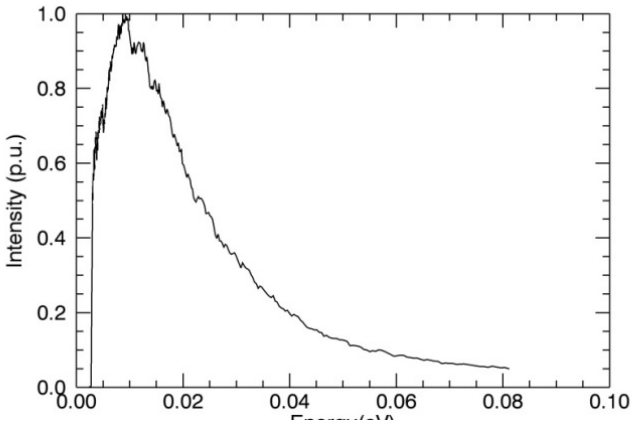

Figure 5. Neutron spectrum in the ROTAX beam line.

2016 JINST 11 C03033

The types of performed measurements are:

- measurements with the lamellas perpendicular to the neutron beam direction.
- measurements with the lamellas inclined by different angles with respect to the neutron beam.

Each measurement is composed by the following steps:

- Acquisition of the CCD "dark signal" with the neutron shutter closed.
- Acquisition of the neutron "open beam" $\tilde{I}_0$ (i.e. without sample).
- Acquisition of the lamella radiography at different positions ($\tilde{I}$). See figure 9 for details.
- Rotation of the lamella and acquisition of the neutron radiography for different angles of irradiation.

For each step, the acquisition system produces a file that contains a matrix of 512x512 16-bit pixels, subsequently analysed by an appropriate code.

3.5 Data analysis

All the images recorded by the acquisition system are processed by an IDL [12] code, whose operations are summarized in the following.

After importing the data into the IDL environment, the code selects the data useful for the analysis, discarding the parts near the sample holder, as shown in figure 6.

This operation is followed by the subtraction of the dark signal (obtained with the shutter closed), from the beam signals, without ($\tilde{I}_0$) and with ($\tilde{I}$) the lamellas. In this way the gamma-ray background due to the activation of the surrounding materials in the ROTAX block-house is subtracted from the data useful for the analysis. However the gamma-sensitivity of the scintillator used in the measurements is very low (about 10^{-6}) as shown in [15]. This is a very important feature of the neutron radiography system used, given that in 93% of the ^{10}B neutron abortion reactions,

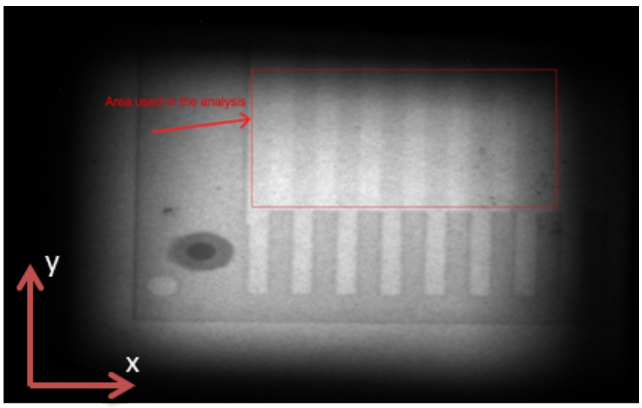

Figure 6. An example of area useful for the analysis.

2016 JINST 11 C03033

the ^{7}Li nucleus is created in an excited state which relaxes through the emission of a 0.48 MeV gamma-ray [16].

The resulting data are then filtered using a low-pass digital Butterworth filter in order to reduce the noise due to the high frequency components and the contribution of the noisy pixels. The filtered data are then normalized by making the ratio between the lamella data ($\tilde{I}$) and the open beam data ($\tilde{I_0}$). In this way is possible to eliminate the beam-shape dependence (the beam is not flat but has a Gaussian profile) from the acquired data.

In order to reduce the fluctuations presented by the normalized image, all the data are averaged along the y direction (i.e. along the strips). In figure 7 is possible to see the plot of the data along an x coordinate before and after this operation.

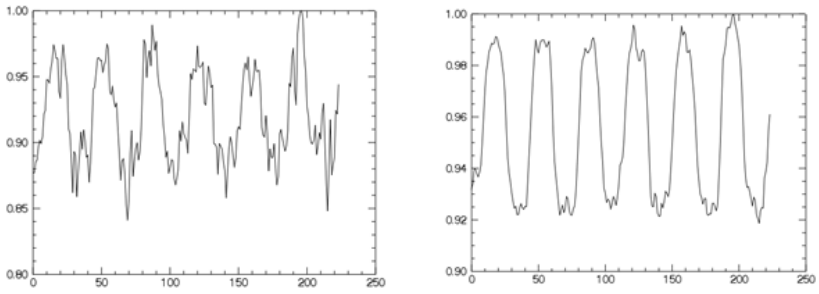

Figure 7. Plot of the data along the x coordinate before (left) and after (right) the averaging and the filtering of the normalized data. The data of the left plot are taken in the middle of the image.

Given the large number of analyzed samples and the resulting large amount of data produced by the measurements, it was necessary to implement an automatic method for the localization of the strips in the image. This method evaluates the firsts derivatives of the normalized-averaged data with respect to the x coordinate. The array of the derivatives is then filtered by a high order low-pass digital filter in order to reduce the high frequency noise, as shown in figure 8.

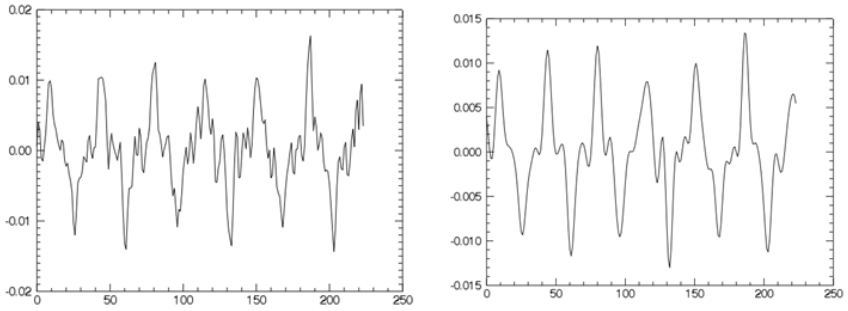

Figure 8. Plot of the first derivative first (left) and after (right) the application of the filter.

The strips of the lamella begin at the points in which the first derivative is lower than a fixed negative constant and terminate at the points in which the first derivative is greater than a fixed positive constant. The values of the constants were found after an empiric evaluation of the images. When

2016 JINST 11 C03033

the strips are localized, the data that lie on them are averaged along the y coordinate (along the strip) as well as the data that lie outside of them. The ratio between the average of the data on the strips and the average of the data outside of the strips gives an estimation of the neutron absorption ($\text{neutron}_{\text{abs}}$).

It is now possible to obtain the value of the amount of boron carbide crossed by the neutron beam in terms of equivalent mass density ρ, by implementing in the code an iterative method that minimizes the following equation:

$$\tilde{I} = (1 - \text{neutron}_{\text{abs}}) \cdot \tilde{I}_0$$

The value of ρ is found through the evaluation of the residuals:

$$\rho \rightarrow \left| \left(\left((1 - \text{neutron}_{\text{abs}}) \cdot \tilde{I}_0 \right) - \tilde{I} \right)^2 \right|_{\text{min}}$$

The value of the equivalent boron carbide mass density found is used for the calculation of the measured equivalent thickness t^{measured}:

$$t^{\text{measured}} = \frac{\rho z}{PM}$$

which is then used for the calculation of the measured transmitted radiation $\left(\frac{\tilde{I}}{\tilde{I}_0}\right)^{\text{measured}}$ that will be compared with the expected transmitted radiation $\left(\frac{\tilde{I}}{\tilde{I}_0}\right)^{\text{expected}}$

3.6 Results of the measurements with the lamellas perpendicular to the neutron beam

In order to obtain a complete characterization of the film deposit, all the lamellas (about 80 samples) was enlightened by the ROTAX neutron beam at different positions. Figure 9 shows the map of the different measurements position.

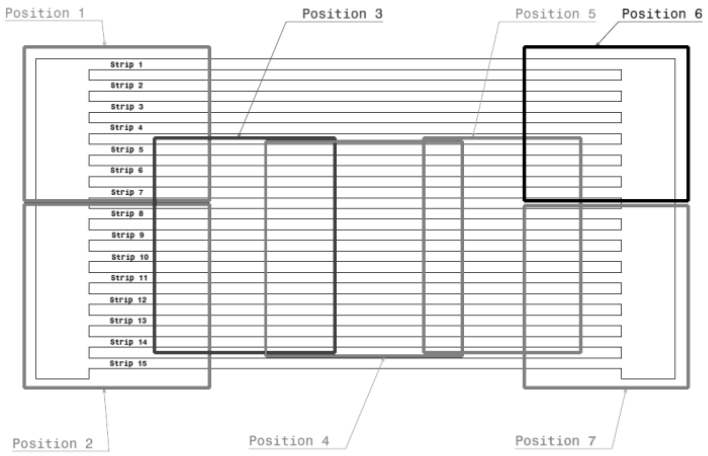

Figure 9. Schematic of the different neutron irradiation positions.

All the strips are enlightened by the beam at least twice, and the comparisons between all the different measurements give an estimate of the quality of the coating. For each measurement the code extrapolates a set of t^{measured} values (one value for each strip in the enlightened area), which

2016 JINST 11 C03033

are subsequently used for the evaluation of the $^{10}B_4C$ coating uniformity. A lamella is considered as suitable to compose the 3D-C if the coating has a value of non-uniformity less than 10% with respect to the average of all the $t^{measured}$ values found on the entire lamella surface. Figure 10 shows a sample of accepted lamellas, with the labelling of the strips as per figure 9. For the strips 1,2,3,4 and 15 two values of $t^{measured}$ are obtained, while for all the other strips five values of $t^{measured}$ are obtained.

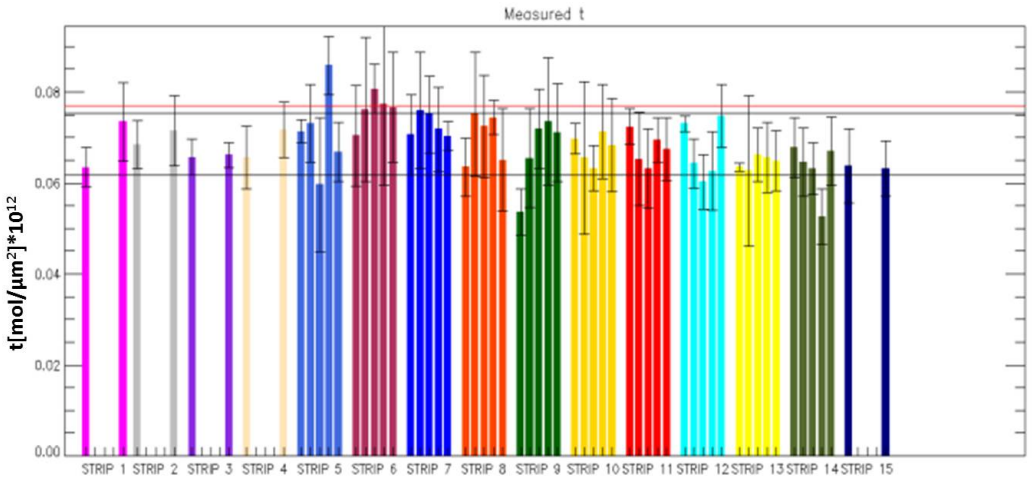

Figure 10. Example of accepted lamella. The red line indicates the $t^{expected}$ value; the black horizontal lines indicate the acceptance criteria: if the $t^{measured}$ values lie between these two lines the lamella is accepted.

More than the 90% of the enlightened samples satisfy the acceptance criterion. Moreover these measurements have shown that the deposition process is reasonably reproducible: therefore only a small number of samples will be checked in the future, in order to highlight possible major failures in a particular deposition run.

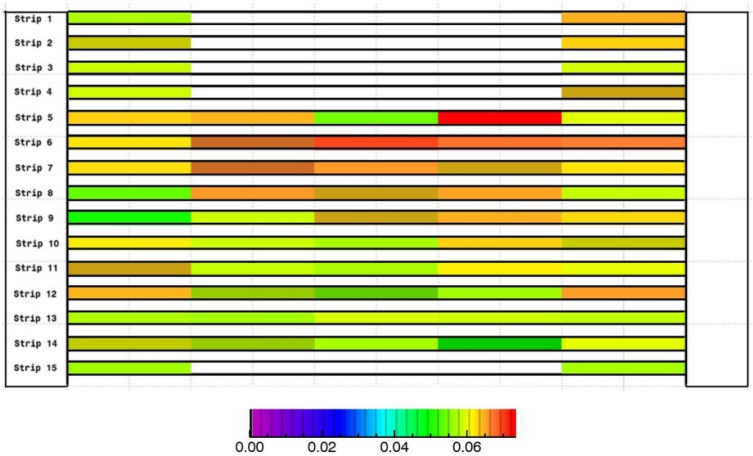

Figure 11. Bi-dimensional map of the $t^{mesaured}$ values on an accepted lamella. The values of the legend must be multiplied by 1012 in order to get the value in mol/μm^2 units.

3.7 Results of the measurements with the lamella inclined by different angles

The envisaged detector will be inclined with respect to the incoming neutron beam, in order to increase the efficiency keeping constant the escape probability of the generated charge particles inside the neutron converter coating [13]. This behavior was confirmed by a measure taken during the ROTAX campaign. In figure 12 is shown the comparison between the expected transmitted radiation $\left(\frac{\tilde{I}}{\tilde{I}_0}\right)^{\text{expected}}$ and the measured one $\left(\frac{\tilde{I}}{\tilde{I}_0}\right)^{\text{measured}}$ for the measurements taken for a single lamella rotated from 0° to 81° in steps of 0.9°.

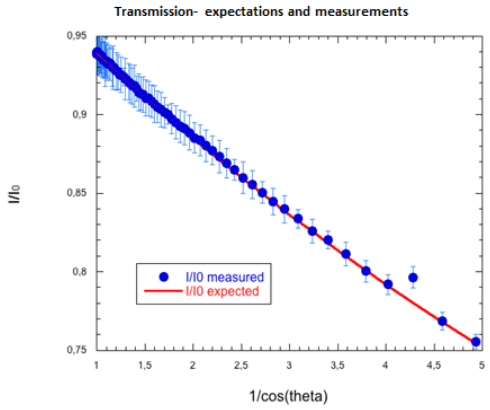

Figure 12. Comparison between the expected transmitted radiation (red line) and the measured one by varying the incidence angle of the incoming neutron beam.

By varying the angle between the coated lamella and the neutron beam, the fraction of absorbed neutron is increased, due to the longest path of the neutron inside the $^{10}B_4C$ coating. However in the $n^0+^{10}B \rightarrow ^7Li+^4He$ reaction the charged particles are emitted back-to-back, therefore the probability to escape from the coating is the same that would occur with the $^{10}B_4C$ coating placed orthogonally to the neutron beam. This means that with a good choice of the 3D-C geometry, one can obtain higher neutron absorption with respect to the standard 2D-C without paying in terms of escape probability of the generated charged particles [13].

3.8 Measurement of lamellas with different boron thickness

Ten lamellas out of 80 were by purpose coated with 1.1 μm of B_4C instead of 1 μm. The neutron radiography technique was also applied to check if it was possible to distinguish coatings that have a 10% difference in thickness. Figure 13 shows that using this technique two different values of t are obtained for the lamellas with 1.1 and 1 um of B_4C, respectively. As expected the two groups of lamellas are well separated beyond the estimated error bars. Only a small fraction of the samples is shown in figure 13.

3.9 Results validation

The analysis method was validated applying the same analysis method to a standard vanadium sample of known thickness and density.

2016 JINST 11 C03033

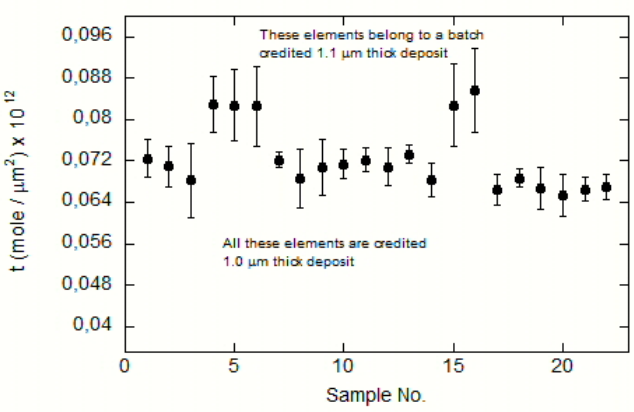

Figure 13. Comparison between the t measured for lamellas with 1 and 1.1 μm B_4C coatings. Some of the samples are shown.

The extracted and the real equivalent thickness $t$of Vanadium are:

$$t^{\text{extracted}} = 2,30 \times 10^{-4}\,\text{mol} \cdot \text{mm}^{-2}$$

$$t^{\text{expected}} = 2,35 \times 10^{-4}\,\text{mol} \cdot \text{mm}^{-2}$$

From the value of $t^{\text{extracted}}$ it is possible to extract the thickness z of the Vanadium:

$$z^{\text{extracted}} = 1,92\,\text{mm}$$

that can be compared with the real thickness of the block

$$z^{\text{real}} = 1,95\,\text{mm}.$$

4 Conclusions and future work

In this work a series of destructive and non-destructive measurements made on a series of Al_2O_3 lamellas coated with 1 μm of $^{10}B_4C$ have been presented. These tests were made in order to evaluate the suitability of the lamellas in order to realize a three dimensional cathode of a new ^{3}He-free thermal neutron detector. All the analyses have shown that the larger fraction of the measured samples (more than the 90%) are suitable to be used in the realization of the three dimensional cathode.

Acknowledgments

This work was supported within the CNR-STFC Agreement No. 01/9001 concerning collaboration in scientific research at the spallation neutron source ISIS. The financial support of the Consiglio Nazionale delle Ricerche in this research is hereby acknowledged.

2016 JINST 11 C03033

Paper V

IOP Publishing Measurement Science and Technology
Meas. Sci. Technol. **27** (2016) 115902 (9pp) doi:10.1088/0957-0233/27/11/115902

Evolution in boron-based GEM detectors for diffraction measurements: from planar to 3D converters

Giorgia Albani[1,4], Enrico Perelli Cippo[2], Gabriele Croci[1,4], Andrea Muraro[2], Erik Schooneveld[3], Antonella Scherillo[3], Richard Hall-Wilton[5,8], Kalliopi Kanaki[5], Carina Höglund[5,6], Lars Hultman[6], Jens Birch[6], Gerardo Claps[7], Fabrizio Murtas[7], Marica Rebai[1,4], Marco Tardocchi[2] and Giuseppe Gorini[1,2,4]

[1] Dipartimento di Fisica, Università degli Studi di Milano-Bicocca, Piazza della Scienza 3, 20126 Milano, Italy
[2] Istituto di Fisica del Plasma (IFP-CNR), Via Cozzi 53, 20125 Milano, Italy
[3] STFC-ISIS Facility, RAL, OX11 0Q, Didcot, UK
[4] INFN Sezione di Milano-Bicocca, Piazza della Scienza 3, 20126 Milano, Italy
[5] European Spallation Source ERIC, PO Box 176, 22 100 Lund, Sweden
[6] Department of Physics, Chemistry and Biology (IFM), Linköping University, SE-581 83 Linköping, Sweden
[7] INFN, Laboratori Nazionali di Frascati, Via Fermi 40, 0044 Frascati, Italy
[8] Mittuniversitetet, Holmgatan 10, 85170 Sundsvall, Sweden

E-mail: giorgia.albani@unimib.it

Received 9 May 2016, revised 7 September 2016
Accepted for publication 15 September 2016
Published 7 October 2016

Abstract

The so-called '^{3}He-*crisis*' has motivated the neutron detector community to undertake an intense R&D programme in order to develop technologies alternative to standard ^{3}He tubes and suitable for neutron detection systems in future spallation sources such as the European spallation source (ESS).

Boron-based GEM (gas electron multiplier) detectors are a promising '^{3}He-free' technology for thermal neutron detection in neutron scattering experiments. In this paper the evolution of boron-based GEM detectors from planar to 3D converters with an application in diffraction measurements is presented. The use of 3D converters coupled with GEMs allows for an optimization of the detector performances. Three different detectors were used for diffraction measurements on the INES instrument at the ISIS spallation source. The performances of the GEM-detectors are compared with those of conventional ^{3}He tubes installed on the INES instrument.

The conceptual detector with the 3D converter used in this paper reached a count rate per unit area of about 25% relative to the currently installed ^{3}He tube. Its timing resolution is similar and the signal-to-background ratio (S/B) is 2 times lower.

Keywords: neutron detector, GEM technology, diffraction detector, helium^3-free detector

(Some figures may appear in colour only in the online journal)

1. Introduction

The ^{3}He shortage [1, 2] is limiting its use in scientific applications including future neutron sources such as the European spallation source (ESS) [3, 4] where detectors with large areas (several m^2), high efficiency (>50%) and high rate capability (in excess of 0.1 MHz cm^{-2}) are needed.

As a result, one important task of the neutron scattering instrumentation community is to find alternative technologies in the detection of thermal neutrons [5–8]. There is a growing interest

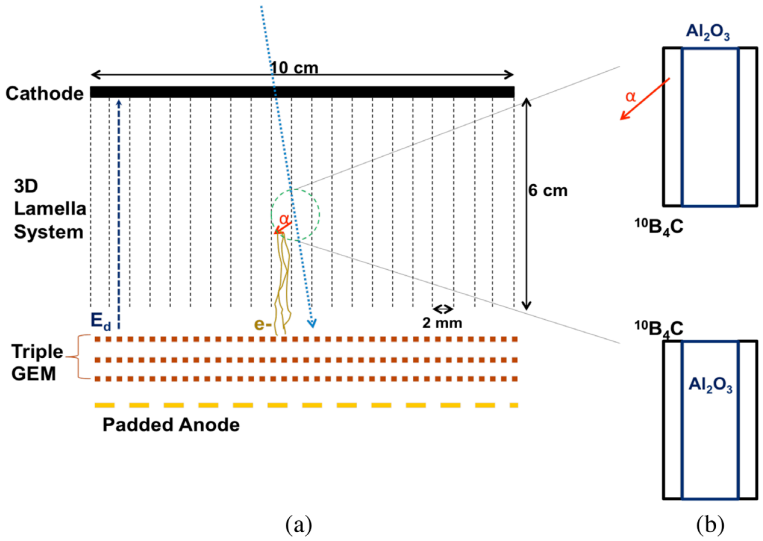

Figure 1. (a) Operation scheme of the BAND-GEM. The 3D converter is composed by Al_2O_3 lamellas (6 cm × 10 cm) borated on each side with 1 μm of $^{10}B_4C$. Lamellas are grids composed by 2 mm thick strips with a 4 mm pitch as shown with a zoom in (b). The gap between two different lamellas is 2 mm as shown in (a). When the neutron is captured in the $^{10}B_4C$ layer, α and ^{7}Li are emitted back-to-back in the converter gas. The primary ionization electrons follow the electric field towards the triple GEM where they are multiplied.

in recent years in the use of the gas electron multiplier (GEM) [9] detectors for enhancing neutron detection. GEMs are widely used in high-energy physics for tracking and triggering, thanks to their good spatial resolution (from 80 μm up to few mm) and timing properties (few ns). Moreover these detectors offer an excellent rate capability (>1 MHz mm^{-2}), radiation hardness and the possibility to cover large areas (several m^2) at reasonable cost [10, 11]. Although GEM-based detectors are generally used to detect charged particles they can be adapted to reveal neutrons by choosing a proper converter [12–19]. The rate capability of this technology under high flux neutron irradiation was also proven in the last years [20]. In this paper the improvements in the performance of a series of GEM-based detectors with a borated cathode for thermal neutrons are presented. The recent results [21] from a first diffraction experiment with a planar borated cathode GEM detector (bGEM) at the INES diffractometer [22, 23] at ISIS showed that the technology has the potential to be used in future neutron spallation sources but lacked the efficiency, the resolution and the S/B ratio to be an immediate alternative to currently installed ^{3}He tubes. Improved converters have since been coupled to a GEM: a boron-10 enriched boron carbide ($^{10}B_4C$) flat cathode and a newly developed 3D borated cathode (boron array neutron detector: BAND-GEM) [24]. In this paper the evolution from the bGEM to the BAND-GEM detector is presented. The objectives and the challenges of this new technology and finally the results of the improvements in efficiency, timing resolution and S/B ratio compared with the performances of standard ^{3}He tubes are reported.

2. Detector evolution: from bGEM to BAND-GEM

2.1. The bGEM detector

The bGEM detector is a triple GEM [14] equipped with a planar aluminum cathode coated with 1 μm of natural (i.e. 20% ^{10}B) boron carbide (B_4C). Thermal neutrons are absorbed in boron and charged particles are emitted via the nuclear reaction $^{10}B(n, \alpha)^7Li$. Both α and Li ions deposit their energy in the gas and give rise to a signal in the detector [25–27]. A detailed description of this detector and its *electrical configuration* is presented in [21].

2.2. The bGEM detector with enriched cathode

A bGEM with a cathode covered with a 1 μm B_4C coating enriched in ^{10}B (the enrichment in ^{10}B is >96%) to enhance the efficiency was realized [26, 27]. The geometry, the gas gain and the padded anode (132 8 × 8 mm^2 pads + 4 L-shaped pads) are the same as the bGEM with natural B_4C described above.

2.3. The BAND-GEM detector

The last detector developed by the authors is a boron-based GEM detector with a 3D converter (figure 1): this 'borated array neutron detector' GEM (BAND-GEM) is composed by 48 *lamellas,* each composed of 15 *strips* of 250 μm thick alumina, coated on both sides with a 1 μm thick $^{10}B_4C$ layer [26–28]. The lamellas are stacked orthogonally to the GEM foils. The converter lamellas and the GEM foils are sealed in a gas box where a constant flow of Ar/CO_2 70%/30% at room temperature and pressure is applied. The lamellas are electrically biased at different voltage so that the electric field across the whole 3D converter is tunable. With a proper regulation of the field, the charged particles produced by the $^{10}B(n, \alpha)^7Li$ nuclear reaction ionize the gas and a fraction of the ionization electrons reach the GEM foils. The padded anode coupled to the GEM is in this case composed of 128 6 × 12 mm^2 pads. A feature of the 3D cathode is that, if the whole detector is tilted by an angle ϕ (figure 2(a)) with respect to the sample-detector

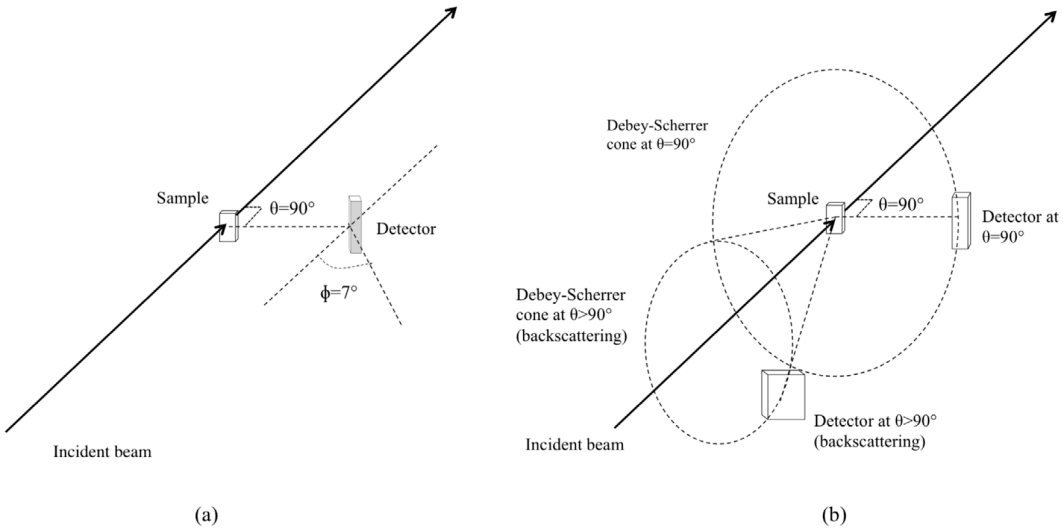

Figure 2. Definition of scattering angle θ, tilting angle ϕ (a) and Debye–Scherrer cones for scattering angle $\theta = 90°$ and scattering angle $\theta > 90°$ (backscattering) (b). When $\theta = 90°$ the Debye–Scherrer cone is parallel to a pad column, thus the focusing is simply the summing of a single column (see section 4.2 for details). When $\theta \neq 90°$, a Debye–Scherrer cone spans different columns, thus the focusing will require the sum of pads belonging to different columns.

Table 1. Summary of some relevant parameters of the experimental setup in the three cases considered in the text.

Exp. no.	GEM detector	Scattering angle (θ)	Reference ^{3}He	Active area	Tilt angle (ϕ)
1	bGEM	90°	73–74	$36 \times (8 \times 8)$ mm^2	0°
2	^{10}B-enr. bGEM	110°	53–54	$36 \times (8 \times 8)$ mm^2	0°
3	BAND-GEM	90°	74	$8 \times (6 \times 12)$ mm^2	7°

direction, the thickness of $^{10}B_4C$ crossed by the neutrons is increased by a factor $1/\sin(\phi)$ and the neutron conversion probability is enhanced accordingly.

3. Measurement setup

The detectors were tested at the neutron diffractometer INES [22, 23] at the ISIS neutron source. Diffraction is one of the most representative measurements that can be performed with thermal neutrons, and the INES instrument is particularly suitable for detector tests because of dedicated supports where detectors can be positioned and used at the same time as ^{3}He tubes.

3.1. The INES beam line at ISIS

INES is a time-of-flight (ToF) diffractometer. The useful neutron wavelengths range between 0.17 Å and 3.24 Å. The INES detector bank is composed by 144 high-pressure (20 bar) squashed ^{3}He tubes (effective sensitive area $100.0 \times 12.5\,\text{mm}^2$, 2.5 mm depth) placed along a circle of 1000 mm radius centered on the sample position. The ^{3}He tubes are numbered starting from the highest angle to the lowest one. Such detectors are estimated to have efficiency between 60% and 70% for neutrons in the thermal energy range [22]. A bank dedicated to detector tests is positioned at a *scattering angle* $\theta = 90°$ (figure 2(a)), symmetrically to the respective ^{3}He tube (No. 74).

3.2. Detector setup

The first diffraction experiment (referred to as '1' in table 1) on INES was performed with the bGEM with natural B_4C [21]. The bGEM was positioned on the dedicated bank at $\theta = 90°$. As the acquisition area considered in the test was about the double of a single ^{3}He tube, two of them were used as a comparison (No. 73 and 74). The diffraction sample was a bronze slab of dimensions 20 mm × 50 mm × 5 mm. The results showed that the bGEM detector is fully able to reproduce the expected ToF diffractogram but with a lower efficiency and signal-to-background ratio than ^{3}He tubes.

A second diffraction experiment with the bGEM cathode now enriched in ^{10}B was performed later. This time the detector was placed on a proper support in the backscattering area ($\theta > 90°$) (figure 2(b)) because the bank at $\theta = 90°$ was not available at that moment. The respective ^{3}He tubes taken as reference were in this case No. 53 and 54. The sample was a bronze parallelepiped of 10 mm × 60 mm × 60 mm.

In a third diffraction experiment the BAND-GEM was positioned on the dedicated bank at $\theta = 90°$. In this case, the efficiency was so enhanced with respect to the previous tests that a single column of pads was enough to obtain a signal with good statistics. Thus in this case a better comparison was made with a single ^{3}He tube (No. 74). The sample was the same as experiment 2. For what concerns the BAND-GEM, preliminary studies had suggested that tilting the detector by $\phi = 7°$

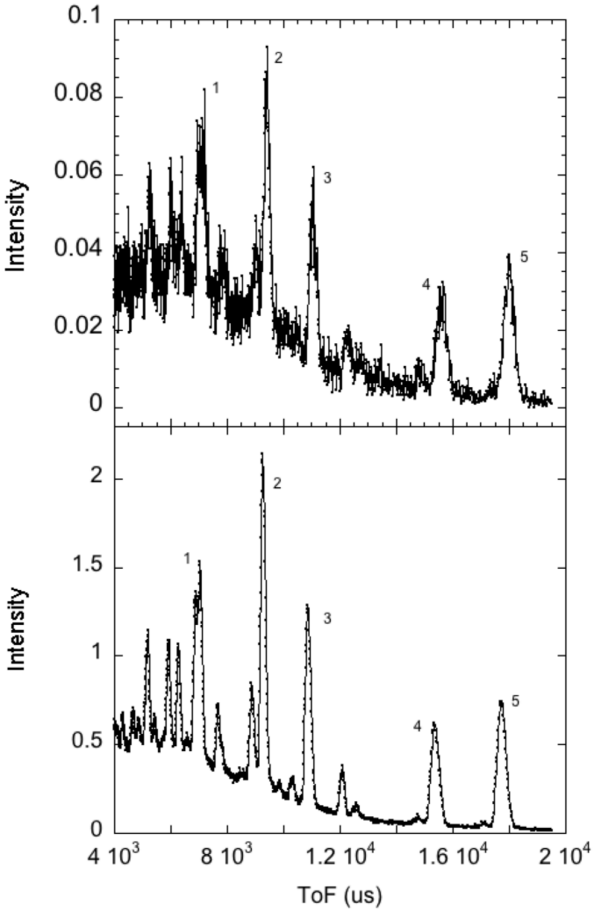

Figure 3. ToF diffractograms recorded at the INES beam line during exp. 1: 36 pads of the bGEM detectors (top) and two conventional ^{3}He tubes (bottom).

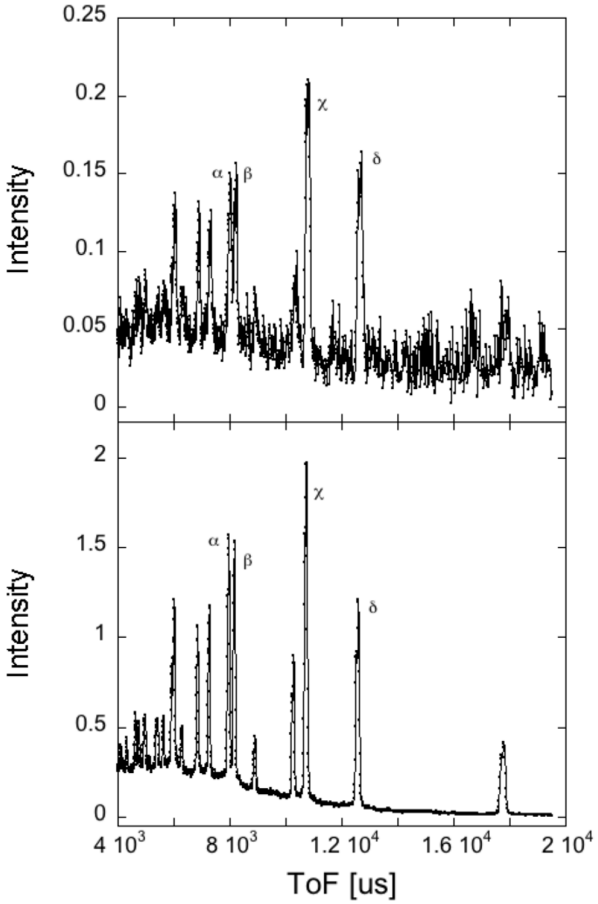

Figure 4. ToF diffractograms recorded at the INES beam line during exp. 2: 36 pads of the ^{10}B-enriched bGEM detectors (top) and two standards ^{3}He tubes (bottom).

Table 2. Results of the Gaussian fit and the analysis with the *Mantid Plot* package for 5 selected peaks recorded in exp. 1

bGEM peaks (exp. 1)	Peak	ToF (μs)	FWHM (μs)	S/B
	1	7076 ± 6	459 ± 114	1.1 ± 0.1
	2	9404 ± 3	240 ± 12	1.6 ± 0.2
	3	$11\,039 \pm 4$	322 ± 18	2.3 ± 0.4
	4	$15\,603 \pm 7$	446 ± 48	4.9 ± 1.5
	5	$17\,994 \pm 5$	435 ± 16	9 ± 3
^{3}He peaks (exp. 1)	Peak	ToF (μs)	FWHM (μs)	S/B
	1	6690 ± 20	325 ± 20	1.2 ± 0.1
	2	9277 ± 1	195 ± 4	2.3 ± 0.1
	3	$10\,877 \pm 1$	231 ± 5	2.8 ± 0.1
	4	$15\,381 \pm 2$	336 ± 6	5.3 ± 0.4
	5	$17\,746 \pm 3$	378 ± 8	12 ± 1

(figure 2(a)) with respect to the sample-detector direction the efficiency for thermal neutrons should reach its maximum [24]. For this reason, the BAND-GEM detector was positioned on INES on the dedicated bank at $\theta = 90°$ and tilted of $\phi = 7°$ (figure 2(a)). The *working point* (i.e. the applied voltage to the GEM foils) was set to $V_{GEM} = 950$ V and the electrical configuration was: drift field $E_d = 0.4$ kV cm^{-1}, transfer1 field $E_{T1} = 3$ kV cm^{-1}, transfer $E_{T2} = 3$ kV cm^{-1}, induction field $E_{ind} = 5$ kV cm^{-1}. These settings have been determined in previous tests made at the IFE JEEP II reactor in Norway [24]. Every detector has been shielded with a suitable Cadmium mask against the neutron scattering [21].

A summary of the three experiments discussed is shown in table 1.

3.3. Electronic setup

The electronic setup of the detector was unchanged with respect to what is described in [21]: a read-out of the pads based on CARIOCAs digital and self-triggered chips [29] were positioned on the back of the anode. The interface between the front-end electronics and the standard ISIS data acquisitions electronics (DAE) was formed by routing the LVDS signals generated by four CARIOCAs to a user-designed FPGA board. When the FPGA found data in one of the buffers, the position of the respective GEM pad that generated the signal was sent to the DAE. LLD thresholds in the CARIOCA chips were set at 1200 mV [24]. This value had been determined in previous tests to be adequate to

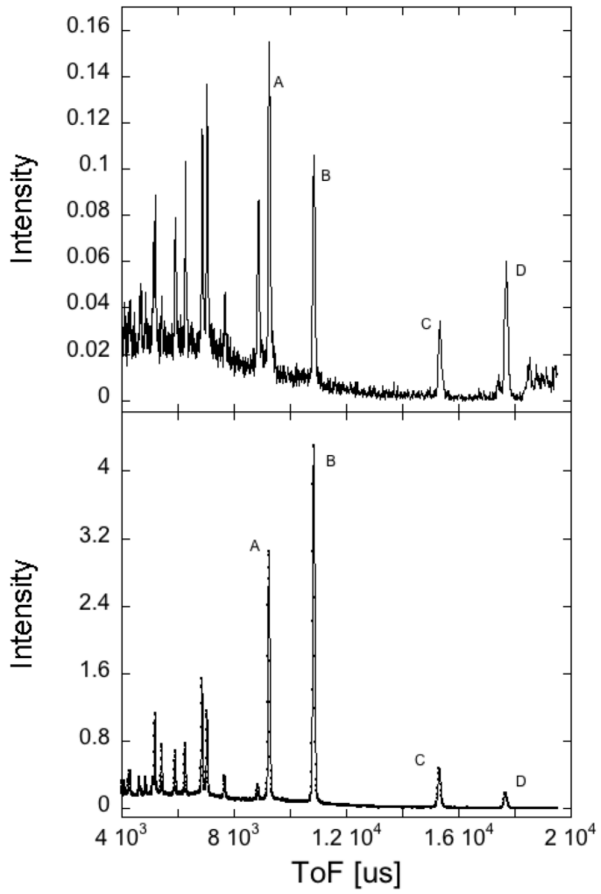

Figure 5. ToF diffractograms recorded at the INES beam line with a BAND-GEM detectors (top) and a standard ^{3}He tube (bottom) in exp. 3.

safely remove the electronic noise; such tests also showed that with the applied voltage used in the three experiments (from 870 V to 950 V) the gamma-ray background is negligible [19–21, 24, 30, 31].

4. Results and analysis of performance

Data obtained in the three experiments are discussed in this section. Figures 3–5 present the diffractograms obtained with the GEM (top panel) and the reference ^{3}He detector (bottom panel) in a selected ToF region (4–20 ms). The intensity of the peaks is measured in Counts μAh^{-1}.

The peaks visible in the diffractograms are due to Bragg scattering on the bronze sample; the most visible peaks are chosen for the detectors comparison and are labelled. Some differences in the relative intensities of the peaks were expected and they are due to the textured nature of the scattering sample. A polycrystalline sample is defined as textured if the crystallites main directions are not isotropically distributed but concentrated along selected directions. This results in the Bragg scattering to be more intense in some directions than in others. However, in the following discussions, we concentrate on parameters related to the single peaks (for instance FWHM), thus such differences are negligible for the analysis.

Table 3. Results of the Gaussian fit and the analysis with the mantid plot package for 4 selected peaks of the ToF diffractograms recorded at the INES beam line with the enriched $^{10}B_4C$ bGEM detector (top) and two standards ^{3}He tubes (bottom).

bGEM peaks (exp. 2)	Peak	ToF (μs)	FWHM (μs)	S/B
	α	8005 ± 1	186 ± 5	2.2 ± 0.8
	β	8203 ± 2	197 ± 7	2.2 ± 0.8
	χ	10786 ± 1	193 ± 2	3.4 ± 1.9
	δ	12651 ± 1	235 ± 2	2.5 ± 1.5
^{3}He peaks (exp. 2)	Peak	ToF (μs)	FWHM (μs)	S/B
	α	7953.7 ± 0.2	104.3 ± 0.7	3.6 ± 0.4
	β	8157.7 ± 0.2	103.2 ± 0.5	4.4 ± 0.6
	χ	10719.7 ± 0.2	121.3 ± 0.5	11.8 ± 2.7
	δ	$12\,563.8 \pm 0.4$	138.2 ± 0.7	10.2 ± 3.5

Table 4. Results of the Gaussian fit and the analysis with the mantid plot package for 4 selected peaks of the ToF diffractograms recorded at the INES beam line with one column of the BAND-GEM (top) and a standard ^{3}He tube (bottom).

BAND-GEM peaks (exp. 3)	Peak	ToF (μs)	FWHM (μs)	S/B
	A	9252 ± 1	92 ± 2	6.7 ± 1.7
	B	$10\,845 \pm 1$	101 ± 2	6.6 ± 2.6
	C	$15\,336 \pm 3$	153 ± 7	7.5 ± 3.9
	D	$17\,690 \pm 2$	132 ± 4	19.4 ± 6.3
^{3}He peaks (exp. 3)	Peak	ToF (μs)	FWHM (μs)	S/B
	A	9246 ± 1	80 ± 2	12 ± 1.2
	B	$10\,841 \pm 1$	87 ± 2	23 ± 2.6
	C	$15\,321 \pm 1$	134 ± 2	17 ± 4.5
	D	$17\,684 \pm 1$	141 ± 2	10 ± 2.6

The count rate, however, is integrated on the whole spectra, thus overcoming the texturing differences.

As each GEM pad is coupled to a separate data acquisition electrons (DAE) channel, the reference diffractograms shown in the following figures are obtained by summing the relevant ToF spectra (i.e. the relevant pads), rebinning them and normalizing them by the integrated current of the measurement (i.e. the total proton charge on the target).

The padded anode allows for selecting a limited number of pads to be summed, for instance belonging to the same Debye–Scherrer cone. For the sake of the comparison, the active area (i.e. the selected pads) was tailored in order to match as best as was possible the shape and dimensions of the reference detectors. The bGEM active area in both experiments 1 and 2 was $8 \times 8\,\text{mm}^2 \times 36$ pads ($2304\,\text{mm}^2$) split in three columns, in order to better match the active area of two ^{3}He, that is $2 \times 100 \times 12.5\,\text{mm}^2$ ($2500\,\text{mm}^2$). In the case of the BAND-GEM the higher count rate allowed to get satisfactory statistics with a smaller number of pads; thus, a single column of 8 pads (12 mm × 6 mm) was considered as active area, again in order to better match the area of a single ^{3}He detector.

Table 5. In column no. 2 are reported the expected ratios of GEM count rates with respect to an ideal ^{3}He tube with a 65% efficiency.

GEM cathodes	Expected GEM count rate/ ideal ($\varepsilon = 65\%$) ^{3}He count rate	Measured GEM count rate/ INES ^{3}He count rate
Planar-B_4C (exp. 1)	0.02	0.07
Planar-$^{10}B_4C$ (exp. 2)	0.08	0.19
BAND-GEM (exp. 3)	0.10	0.25

In column no. 3 are presented the ratios of count rates of the GEM detectors with respect to the respective ^{3}He tubes on INES. The count rates are normalized to the integrated beam current and to the active area of each detector.

The data analysis was performed for all cases with the *Mantid Plot* package [32, 33].

Selected peaks are fitted with Gaussian distributions. Tables 2, 3 and 4 summarize the fit results (for both the GEM detector and the reference ^{3}He) relative to the figures 3, 4, and 5 respectively.

4.1. Efficiency

One of the main reasons for the successive developments of the detectors presented in this paper is the search for a higher efficiency. Preliminary calculations suggested that the neutron efficiency to reference thermal neutrons (1.8 Å) scales roughly as 1 to 4 to 5 for the bGEM, enriched bGEM, BAND-GEM respectively [15–21, 24] as shown in the second column of table 5. The first ratio scales simply with the ^{10}B enrichment, while the second one is due to the geometry of the whole 3D converter and is subject to higher uncertainties. However, the differences in setup of the three experiment earlier mentioned may cause discrepancies to the measured efficiency (for instances, different background conditions and textured samples). It was thus a choice of the authors to refer only on the *counting rate* of the three detectors compared with the respective ^{3}He reference detectors, in order to show how the improvements of the detector have a practical effect in realistic neutron scattering conditions.

The improvement in counting rate can be inferred by table 5, where the ratios of the measured GEM/^{3}He count rates are shown. The measured count rate scales roughly as 1–4 for the bGEM, enriched bGEM, BAND-GEM respectively. The total count rate of the 36 GEM pads used in the measurements is about 7% the count rate of the reference detectors [21] in the case of exp. 1 and about 19% in the case of exp. 2. The enriched cathode is the only responsible for the enhancement of the detector efficiency; setup uncertainties may easily be responsible for the small discrepancies with respect to the expected efficiency ratio.

The ToF diffractograms recorded by a single column of the BAND-GEM (top) and the respective ^{3}He detector (bottom) are shown in figure 5 and the fit results are listed in table 4. Note that in this case the improvement in efficiency was so high that a single column (8 pads) provided data with very high statistics, so that the texture effects of the sample may be appreciated (differences in the intensity of the same ToF peaks for the BAND-GEM and the ^{3}He). These effects where hardly appreciable in the diffractograms in figures 3 and 4.

As a final remark, it was experimentally confirmed that the efficiency of the BAND-GEM has a dependence with the tilting angle [24]: in figure 6 the ToF diffractograms recorded by a single column of the BAND-GEM tilted at $\phi = 0°$ (top) and $\phi = 7°$ (bottom) are shown. This difference is only due to geometrical effects of the 3D converter.

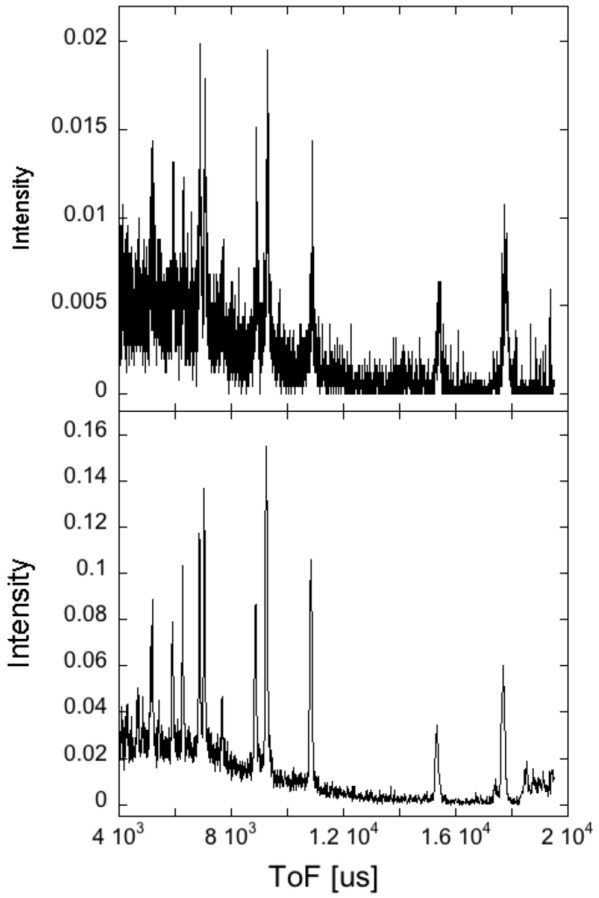

Figure 6. ToF diffractograms recorded at the INES beam line with a BAND-GEM detector tilted by $\phi = 0°$ (top) and $\phi = 7°$ (bottom). ϕ is defined in figure 2.

The most relevant limitation in the BAND-GEM efficiency is due to the electron collection in the conversion region. The electric field in this region, named drift field, allows extracting primary electronic charge from the lamellas system that will be directed towards the multiplication region of the GEM foils. The drift field depends on the potentials on the strips, aluminum cathode and the top of the first GEM foil. The electric field map could be simulated using the Ansys software [34]. The result of the simulation is shown in figure 7 where the field lines between two different lamellas are shown. For the sake of simplicity, the field lines may be visualized as the preferred electron trajectories. It can be noticed that, despite

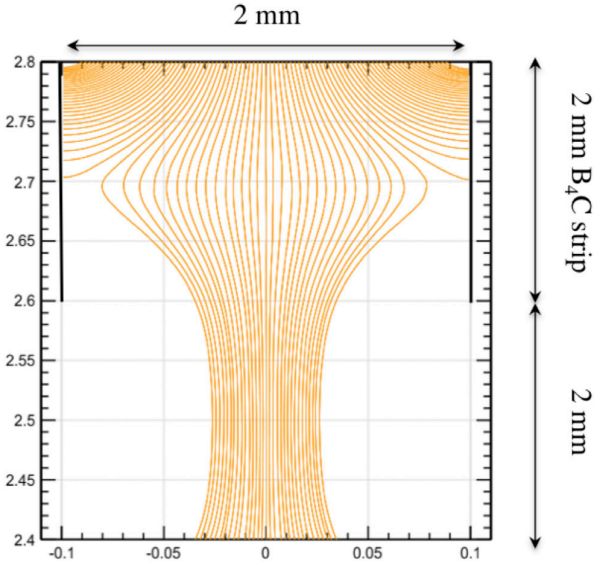

Figure 7. Map of the field lines of the electric drift field in the 3D converter. On the *y* axis is represented the sequence of a 2 mm strip and a 2 mm empty space of a single lamella. On the *x* axis the 2 mm gap between two strips of two different lamellas is indicated.

a significant fraction of the electrons are leaded trough the borated strips, at least one third of the electrons are projected through the next stage (the next couple of electrodes).

To get a better quantitative estimation, the information of the shape of the drift field obtained with Ansys can be combined with a simulation of the electrons transport inside the lamellas gap made with the Garfield software, specifically developed at CERN for simulation related to gas detectors [35].

The extraction efficiency (i.e. the percentage of events, given to gas ionization by either an alpha or a lithium ion, that, after passing through the lamella system, still own a sufficient number of primary electrons over a certain equivalent energy threshold) in the drift region is ~60% with this electrical configuration and 80 keV threshold. This result takes into account the electron drift velocity and diffusion coefficients in the Ar/CO_2 gas mixture and details of these calculations will be presented in a future paper.

The charge extraction efficiency could be significantly improved optimizing the geometry of the converter. The critical parameters to take into account in the optimization study are length, thickness and distance between lamellas. This is indeed the main advantage of the lamella-based geometry respect to the simpler, flat converter geometry. In fact, the geometrical parameters of the system may be tuned to obtain an optimized filed shape and strength. This is the subject of a future study of the present authors in designing the next prototype based on the BAND-GEM technology.

4.2. Timing resolution and S/B

Improvements in timing resolution in exp. 3 with respect to exp. 1 can only be due to better statistics as a logical consequence of the improvements of efficiency (compare for

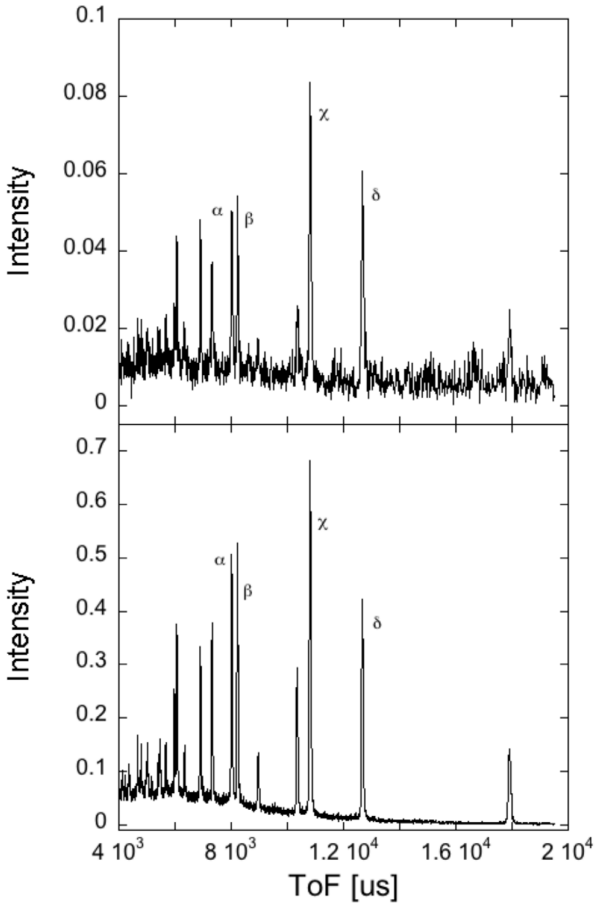

Figure 8. ToF diffractograms recorded at the INES beam line with a focused bGEM detector (top) and a standard ^{3}He detector (bottom). The sample was a bronze parallelepiped of 10 mm × 10 mm × 60 mm dimensions.

instances top panels of figures 4 and 5). The FWHM of the bGEM was 1.75 times the FWHM of the ^{3}He (table 3). The FWHM of the BAND-GEM was only 1.1 times the FWHM of the ^{3}He (table 4). The FWHM values measured in exp. 3 show that the depth of the 3D converter has a negligible effect on the timing of the BAND-GEM. In fact, calculations show that the maximum expected ΔToF associated with the 3D converter ($\Delta L_1 = 100$ mm) is less than 10 μs in the considered time window (up to 40 ms, corresponding to about 3.5 Å wavelength on INES), thus being a minor component of the measured FWHM.

On the other hand, exp. 2 results indicate that the angular component of the timing resolution, thus comprehending the pad dimensions, is not negligible. This can be better appreciated considering the effect of the *focusing* procedure in exp. 2: the FWHM of the selected peaks is reduced by roughly a factor 2. The focusing technique has the aim of summing spectra of pads that lie on the same Debye–Scherrer cone [36], i.e. summing pads that have a constant $L\sin\theta$ where L is the neutron flight path and θ is the angle of the reflected radiation from the sample. When the detector is positioned at $\theta = 90°$ pads of a single column well approximate a single Debye–Scherrer cone (figure 2(b)). The focusing technique leads to a

Table 6. Results of the Gaussian fit and the analysis with the mantid plot package for 4 selected peaks of the ToF diffractograms recorded at the INES beam line with a focused GEM detector (top) and a standard ^{3}He tube (bottom).

Focused bGEM peaks (exp. 2)	Peak	ToF (μs)	FWHM (μs)	S/B
	α	8027 ± 2 (8005 ± 1)	89 ± 5 (186 ± 5)	2.7 ± 1.1 (2.2 ± 0.8)
	β	8235 ± 1 (8203 ± 2)	68 ± 5 (197 ± 7)	3.1 ± 1.5 (2.2 ± 0.8)
	χ	$10\,823 \pm 1$ ($10\,786 \pm 1$)	92 ± 2 (193 ± 2)	4.4 ± 1.3 (3.4 ± 1.9)
	δ	$12\,676 \pm 1$ ($12\,651 \pm 1$)	94 ± 5 (235 ± 2)	4.3 ± 2.6 (2.5 ± 1.5)
^{3}He peaks (exp. 2)	Peak	ToF (μs)	FWHM (μs)	S/B
	α	8021.9 ± 0.2	60.6 ± 0.5	5.0 ± 0.9
	β	8228.4 ± 0.2	58.5 ± 0.5	5.5 ± 1.1
	χ	$10\,813.8 \pm 0.2$	76.8 ± 0.5	9.0 ± 2.4
	δ	$12\,674.3 \pm 0.3$	80.1 ± 0.5	8.5 ± 2.2

Note: The values in brackets are the fit results of the GEM detector without focusing.

significant improvement in S/B with respect to straight pads columns only when the detection position is $\theta \neq 90°$.

A direct comparison of S/B ratio (here defined as the ratio of a peak integral and the background area over it) in the detector evolution is less evident because of the texture effects presented by the sample. Nevertheless the improvement of S/B ratio is a direct consequence of the focusing technique where applied: in figure 8 the ToF diffractograms obtained by applying the focusing technique to data taken with the enriched bGEM and one currently installed ^{3}He is shown. In table 6 the ToF, FWHM and S/B for selected peaks are listed. If the focusing is not applied, S/B ratio of the bGEM is 2.8 times lower than S/B of the ^{3}He. After the focusing the S/B ratio of the bGEM becomes only 1.9 times lower than the ^{3}He.

5. Conclusions

The present research aims to develop boron-based GEM detectors as an alternative to standard ^{3}He tubes for thermal neutron detection at ESS.

Three different GEM-based detectors were produced and tested. Two have planar converters (bGEM), one has a 3D neutron converter (BAND-GEM). The detectors were tested on the INES instrument at ISIS in diffraction measurements. The first results [21] showed the bGEM detector can be used for diffraction experiments but the efficiency, timing resolution and S/B ratio must be further improved. In this paper the authors presented the improvements obtained using enriched boron and a 3D converter. The performances of the detectors are then compared with those of conventional ^{3}He tubes installed on INES. In particular the count rate per unit area significantly increased from about 7% for the bGEM, relative to the ^{3}He count rate, to 25% for the BAND-GEM. The timing resolution of the BAND-GEM is comparable with that of ^{3}He, and the S/B ratio is lower of about a factor 2 with respect to the ^{3}He.

The results show that boron-based GEM detectors can reproduce neutron diffractograms produced with ^{3}He detectors and that improvements have been made in recent years.

While the enrichment of the converter material in ^{10}B was a logical step and it resulted in an evident performance improvement, the simple thickening of the converter layer cannot be further exploited. In fact, as it is shown in [24], an increase in the layer thickness does not give any advantage, due to the higher loss of charged reaction products in the layer itself.

Since the main envisaged application of this technology is the thermal neutron detection with high-rate and high-efficiency in spallation sources, the planar geometry was abandoned to make way for a more promising 3D technology in terms of count rate and efficiency. The technology of the 3D converter, developed to optimize the *distribution* of converting material (not just its *thickness*) looks promising as a way to optimize the neutron conversion and charge deposition into the gas. A further improvement in efficiency can be envisaged by modifying the 3D converter geometry (in particular length, thickness and distance between lamellas) to optimize the charge collection, and a better S/B ratio could be reached by the use of a neutron collimator for the BAND-GEM.

The authors want to underline that the effort of manufacturing a 3D converter requires higher costs with respect to the planar converter. However the possibility of tuning both the distribution of the converting material and the charge extraction is only possibile with such a 3D approach. Moreover the authors are involved in the optimization of both the geometry and the production process; the latter will be the subject of a future paper.

Acknowledgments

The experiments were performed with support within the CNR-STFC agreement 2014–2020 concerning collaboration in scientific research at the spallation neutron source ISIS. The financial support of *Consiglio Nazionale delle Ricerche* (CNR-Italy) for pre-construction activities towards the ESS is hereby acknowledged.

R Hall-Wilton would like to acknowledge support from the *BrightnESS* project (Horizon 2020 grant agreement 676548).

References

[1] Shea D A and Morgan D 2010 *The ^{3}He Shortage: Supply, Demand, and Options for Congress* (Congressional Research Service, The Library of Congress)